



RADIOLOGY UPDATE

**JOURNAL available at
radiologyupdate.org**

Online Journal

Lithuanian Association of Radiologists

Editorial board

Editor-in-chief: Prof. Algidas Basevicius

MANAGING EDITORS:

Prof. Saulius Lukosevicius
Prof. Rymante Gleizniene
Prof. Ilona Kulakiene
Prof. Egle Monastyreckiene
Prof. Algirdas Edvardas Tamosiunas
Prof. Nomeda Valeviciene
Prof. Vincentas Veikutis
Prof. Elona Juozaityte
Prof. Arturas Inciura
Assoc. Prof. Jurate Dementaviciene
Assoc. Prof. Antanas Jankauskas
Med. Dr. Arturas Samuilis
Prof. Dr. Renaldas Raisutis
Prof. Dr. Minvydas Ragulskis
Prof. Renaldas Jurkevicius
Prof. Remigijus Zaliunas

INTERNATIONAL EDITORS

LATVIA:

Prof. Gaida Krumina
Assist. Prof. Maija Radzina
Assoc. Prof. Karlis Kupcs
Assist. Prof. Peteris Prieditis

ESTONIA:

Prof. Sergei Nazarenko
Prof. Pilvi Ilves

SWEDEN:

Assoc. Prof. Augustinas Sakinis
Assoc. Prof. Karolina Kublickiene

USA:

Prof. Jovitas Skucas
Assoc. Prof. Arunas Gasparaitis

UKRAINE:

Dr. Tetyana Yalynska
Prof. Olena Sharmazanova
Prof. Volodymyr Rogozhyn
Prof. Tetyana Kozarenko

CHINA:

Assoc. Prof. Guang-qing Lu

ADMINISTRATORS OF JOURNAL:

Julius Vidikas
Tomas Budrys

Contents

Editorial board	3
The role of radiologic imaging in the diagnosis of adrenal tumors: a literature review	6
Improving patient CT scanning protocols in the setting of polytrauma	29
Neuroimaging of headaches attributed to cranial and/or cervical vascular disorders	37
The value of magnetic resonance imaging in the assessment of chemoradiotherapy of cancer of cervix uteri	67
Pulmonary benign leiomyomas mimicking malignant pulmonary metastases: case report and literature review	77
Use of shear wave elastography in the evaluation of liver fibrosis	84
Intracranial osteochondroma: A case report with review of literature	89

The role of radiologic imaging in the diagnosis of adrenal tumors: a literature review

Ruta Pupalyte¹, Algidas Basevicius²

¹Faculty of Medicine, Lithuanian University of Health Sciences, Kaunas, Lithuania

²Department of Radiology, Lithuanian University of Health Sciences, Kaunas, Lithuania

ABSTRACT

Background and aim. The adrenal tumors are a reasonably common pathology. Radiologic imaging detects an adrenal neoplasm in approximately 4% of the patients incidentally. It is also a valuable tool that assists in determining a diagnosis. Furthermore, it may facilitate the further investigation and management of the lesion. This article aims to assess imaging features that are characteristic of the most common adrenal tumors.

Materials and methods. A selective search was carried out for relevant studies concerning radiologic imaging of adrenal adenoma, myelolipoma, pheochromocytoma, carcinoma, metastases, neural crest tumors, lymphoma, hemangioma, lymphangioma, and schwannoma. Medline (PubMed), Cochrane Library, SpringerLink and ScienceDirect databases were used.

Results. US is helpful for the screening of masses in the suprarenal region. Nevertheless, its findings have to be verified by CT or MRI. The golden standard of assessing adrenal tumors is native CT. Those lesions which present with probable malignant features should be evaluated using dynamic contrast-enhanced CT. Chemical shift MRI is a feasible alternative, especially in lipomatous masses. PET/CT is recommended for patients with large or indeterminate lesions.

Conclusion. Adrenal CT protocol is the most reliable technique in the differentiation of these diverse neoplasms. On the other hand, CS-MRI is indispensable for verifying intratumoral adipose tissue and, consequently, selecting the most appropriate approach to manage the mass. Furthermore, PET/CT permits characterizing indistinctive tumors and their potential metastatic spread.

Keywords: adrenal adenoma, pheochromocytoma, adrenocortical carcinoma, adrenal metastasis, computed tomography, magnetic resonance imaging

INTRODUCTION

The adrenal tumors are a reasonably common pathology. Clinical manifestations of these lesions are various; they cause abdominal pain, distention or fever [1]. However, the majority of the masses are asymptomatic. Although they originate from hormone-secreting cells in the adrenal cortex or medulla, the tumors are usually non-functional [2]. Hence, an adrenal mass often is a coincidental imaging finding. Adrenal tumors are found incidentally in approximately 4% of the patients during an abdominal CT scan due to unrelated symptoms [3].

Initial clinical workup, including examination of the patient and laboratory tests, is used in distinguishing the probable type of the tumor. Radiologic imaging is also a valuable tool that assists in determining an accurate diagnosis. Consequently, precise evaluation of imaging findings

allows reducing the number of adrenal biopsies, surgeries and complications [4]. Therefore, the knowledge of imaging techniques and features associated with a particular pathology is immensely beneficial.

AIM

To evaluate radiologic imaging features that are representative of the most common adrenal tumors.

MATERIALS AND METHODS

A selective search was carried out for relevant studies concerning radiologic imaging of adenoma, myelolipoma, pheochromocytoma, carcinoma, metastases, neural crest tumors, lymphoma, hemangioma, lymphangioma, and schwannoma of the adrenal gland. We chose databases from the subscription list of Lithuanian University of

Health Sciences. Medline (PubMed), Cochrane Library, SpringerLink and ScienceDirect databases were used.

RESULTS

Adrenal lesions might not accurately visualize on conventional ultrasound (US) due to small size, stomach or intestinal gas, obesity or severe liver steatosis. US is helpful for the screening of masses in the suprarenal region. Nevertheless, its findings have to be verified by computed tomography (CT) or magnetic resonance imaging (MRI). The golden standard of assessing adrenal tumors is CT [5]. Smaller, slow-growth lesions are presumably benign [6, 7]. Moreover, the attenu-

ation value of 10 Hounsfield units (HU) or less suggests a benign mass on native CT [8–10]. If unenhanced CT scan displays feature associated with malignancy, dynamic contrast-enhanced CT (DCE-CT) with 15-min delayed acquisition through the upper abdomen should be performed [11].

Neoplasms of the adrenal gland have a distinctive pattern of the contrast washout [12]. Moreover, quantitative parameters, such as total percentage washout (APW) and relative percentage washout (RPW), can be calculated [13]. This radiologic framework allows differentiating the lesions more precisely.

Adrenal tumors should also be evaluated using chemical shift MRI (CS-MRI) [14]. The sequence

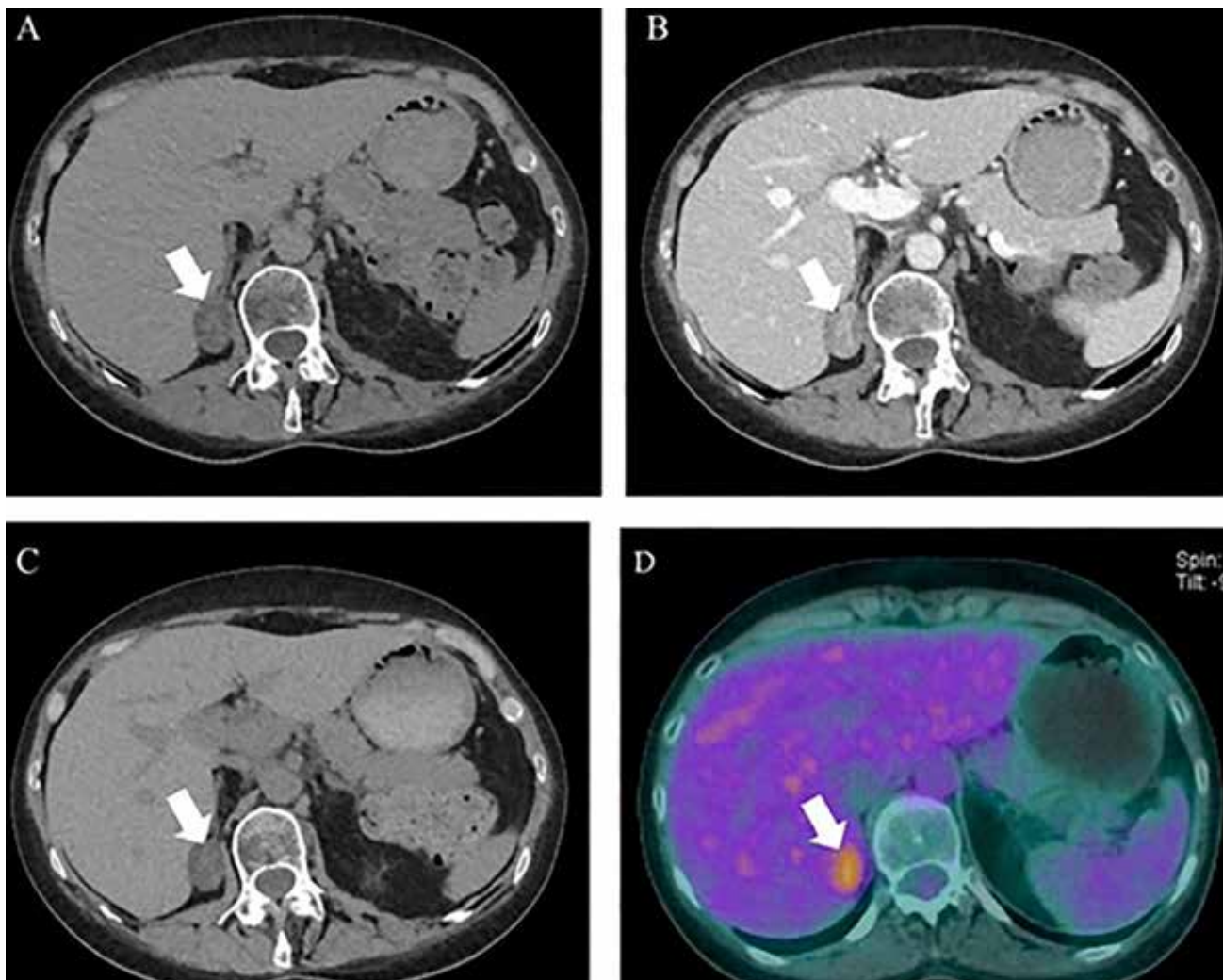


Figure 1. Axial unenhanced CT (A), DCE-CT during the portal venous phase (B) and 15-min delayed CT scans demonstrate well-defined hypoattenuated adrenal lesion (arrow) with early enhancement and rapid washout. SUVmax of the mass is 4.1 on 18F-FDG PET/CT (D). Imaging findings are suggestive of adrenal adenoma. (Humbert, AL, Lecoanet G, Moog S, Bouderraoui F, Bresler L, Vignaud JM, Chevalier E, Brunaud L, Klein M, Cuny T. The computed tomography adrenal wash-out analysis properly classifies cortisol secreting adrenocortical adenomas. *Endocrine* 2018; 59: 529-537)

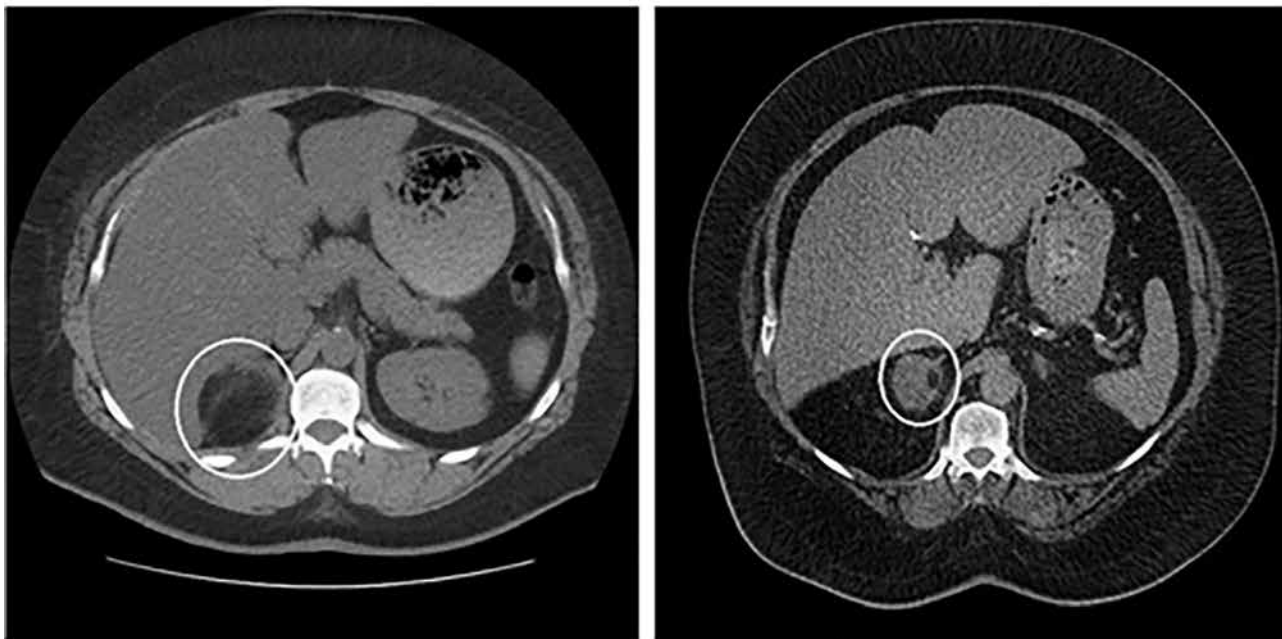


Figure 2. Myelolipoma of almost 100% macroscopic fat (circle) is observed in the right adrenal gland on axial unenhanced CT (A). Its attenuation value is lower than of myelolipoma containing approximately 10% macroscopic fat (B). (Campbell MJ, Obasi M, Wu B, Corwin MT, Fananapazir G. The radiographically diagnosed adrenal myelolipoma: what do we really know? *Endocrine* 2017; 58: 289-294)

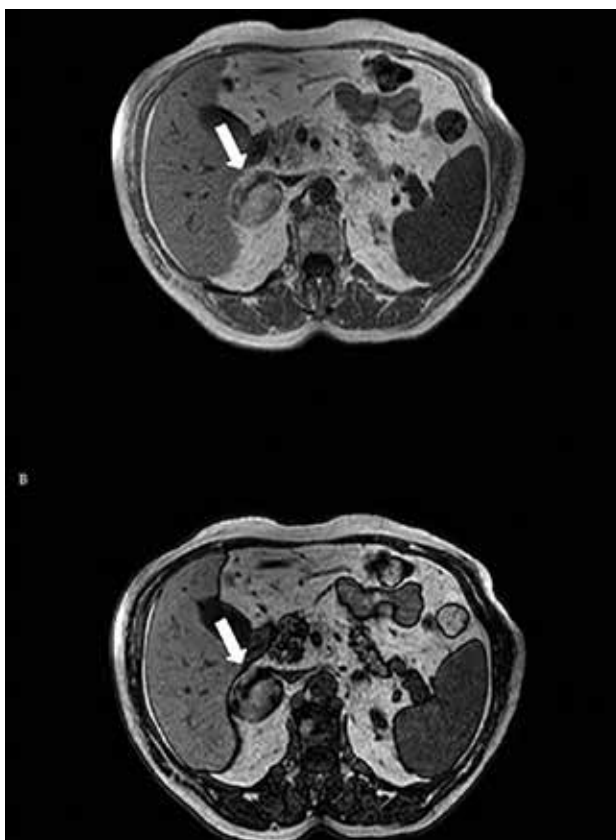


Figure 3. A loss of SI is displayed within adrenal myelolipoma (arrow) between the in-phase (A) and opposed-phase (B) axial CS-MRI. (Lesbats-Jacquot V, Cucchi JM, Amoretti N, Novellas S, Chevallier P, Bruneton JN. Lipomatous tumors of the adrenals – a report on 18 cases and review of the literature. *Clin Imag* 2007; 31: 335-339)

determines a loss of signal intensity (SI) on opposed-phase images compared to in-phase images. This signal drop correlates to intracytoplasmic fat and leads to a presumption of a benign mass [15]. CS-MRI is superior to DCE-CT only in those cases where the unenhanced attenuation value of the adrenal lesion is < 80 HU [16]. If a hyperattenuating tumor presents, DCE-CT achieves higher sensitivity than CS-MRI [17]. However, MRI is appropriate in pregnant patients or those with iodine hypersensitivity and reduced renal function.

Diffusion-weighted MRI (DW-MRI) is not routinely used for separating adrenal neoplasms [18].

Nuclear medicine, especially positron emission tomography (PET), plays a role in the differential diagnosis of adrenal tumors. Various radioisotopes are used, the most common one being fluorine-18-fludeoxyglucose (18F-FDG). A hybrid technique, PET/CT, is recommended for patients with large or indeterminate lesions. Increased metabolic activity of 18F-FDG is characteristic of malignant masses [8, 9, 19–22]. Even though PET/CT demonstrates high accuracy, it is still inferior to DCE-CT [23].

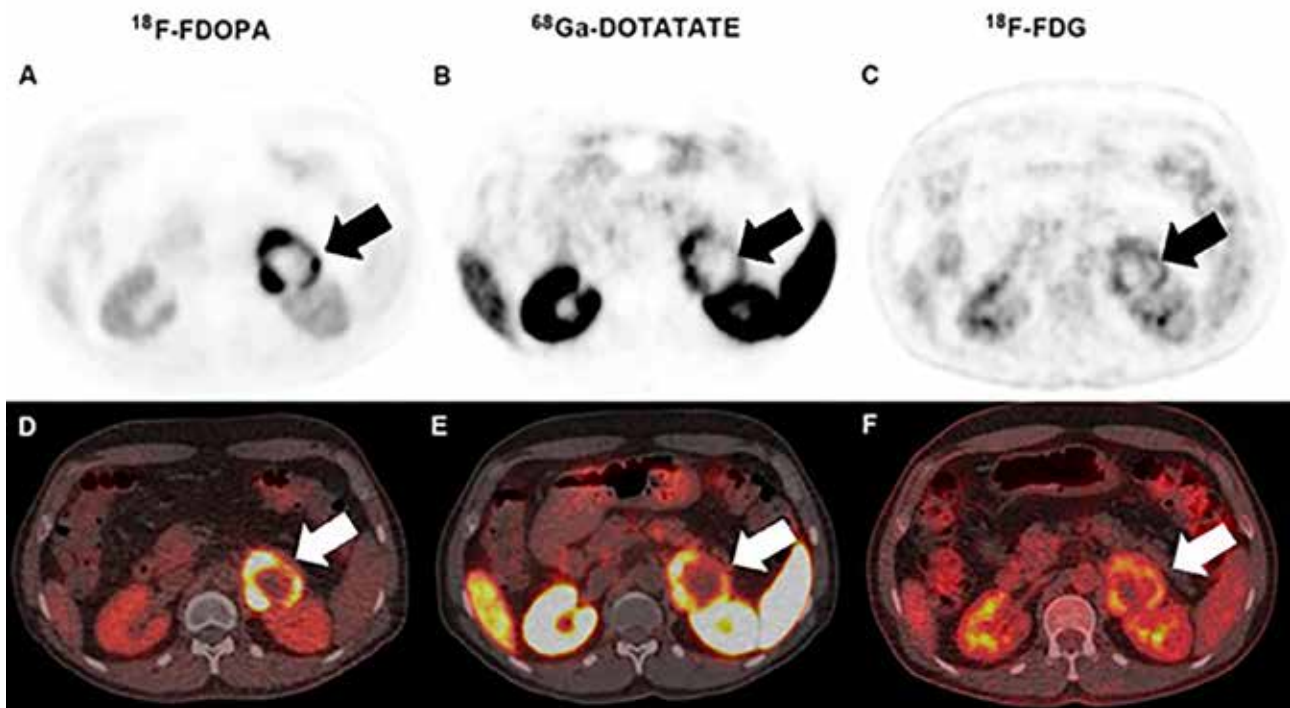
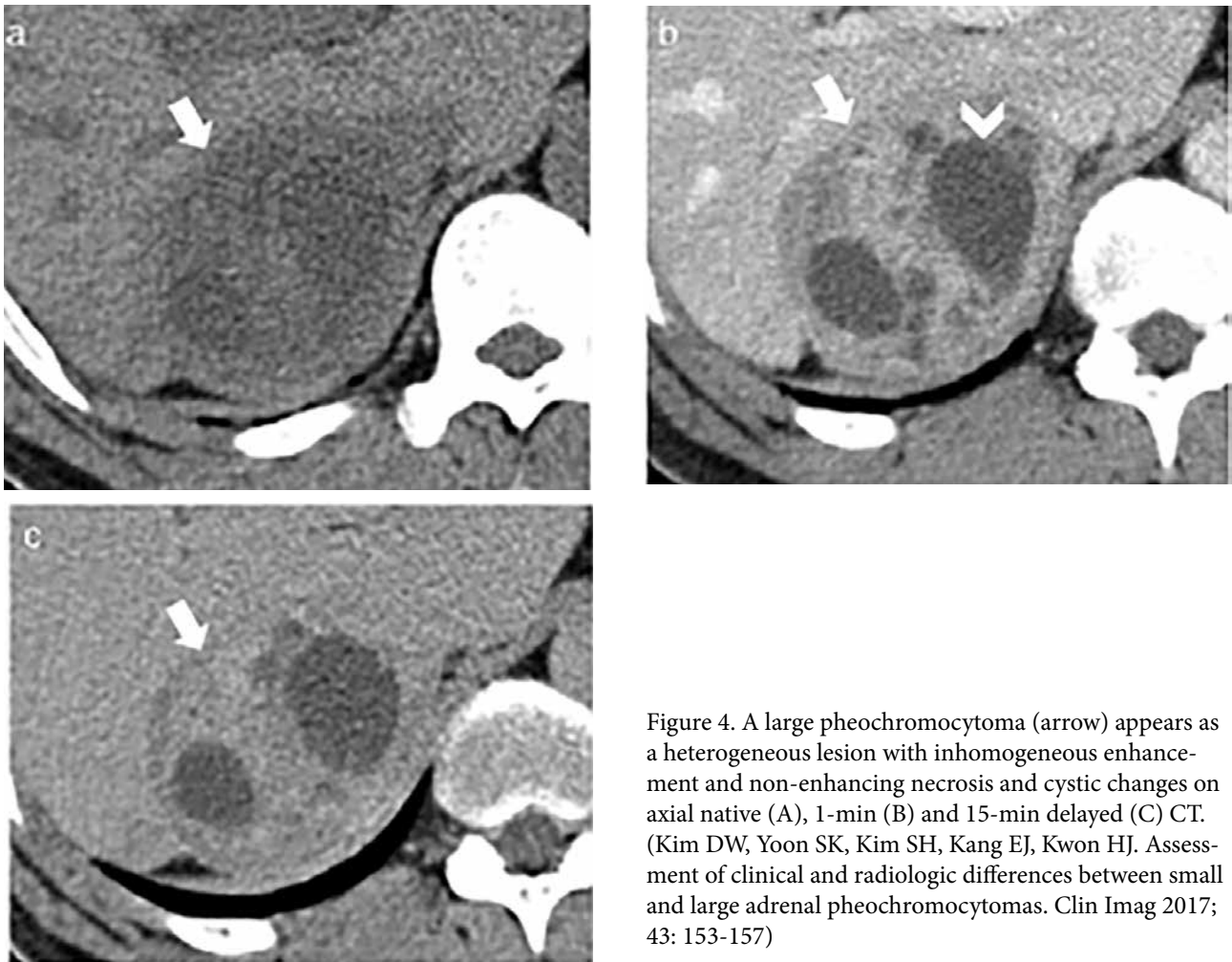




Figure 6. Adrenocortical carcinoma (arrow) presents with a large central non-enhancing hypodense region consistent with necrosis on axial native CT. (Thomas AJ, Habra MA, Bhosale PR, Qayyum AA, Ahmed K, Vicens R, Elsayes KM. Interobserver agreement in distinguishing large adrenal adenomas and adrenocortical carcinomas on computed tomography. *Abdom Radiol* 2018; 43: 3101-3108)

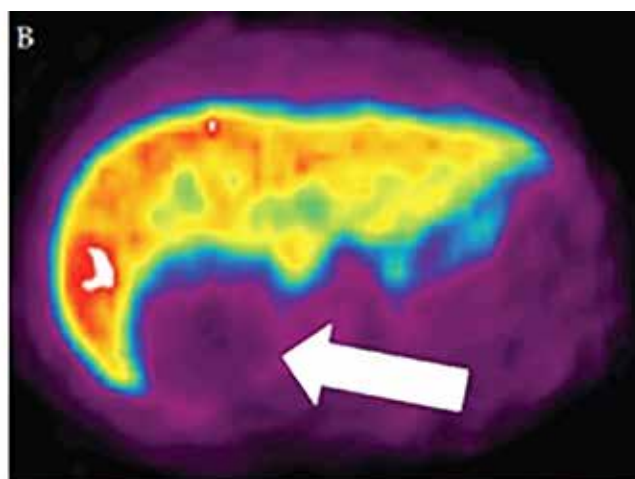
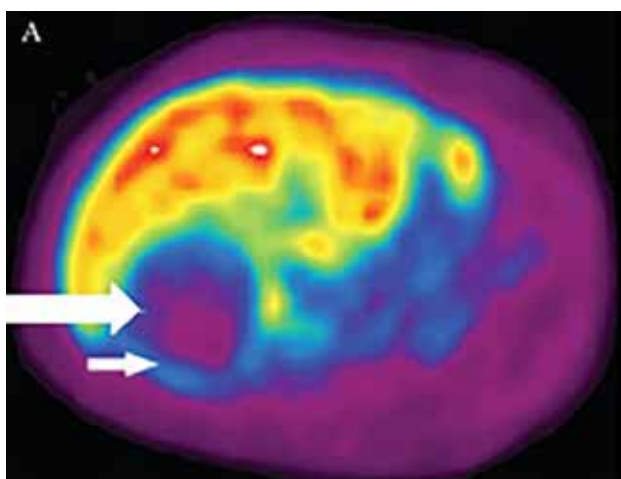


Figure 7. A lack of ¹¹C-MTO uptake within a necrotic adrenal carcinoma (long arrow) is assessed on PET (A). However, a reminiscent uptake (short arrow) can be seen. On the other hand, pheochromocytoma (arrow) does not take up ¹¹C-MTO at any rate (B). (Hennings J, Lindhe O, Bergstrom M, Langstrom B, Sundin A, Hellman P. [¹¹C] Metomidate positron emission tomography of adrenocortical tumors in correlation with histopathological findings. *J Clin Endocrinol Metab* 2006; 91(4):1410-1414)

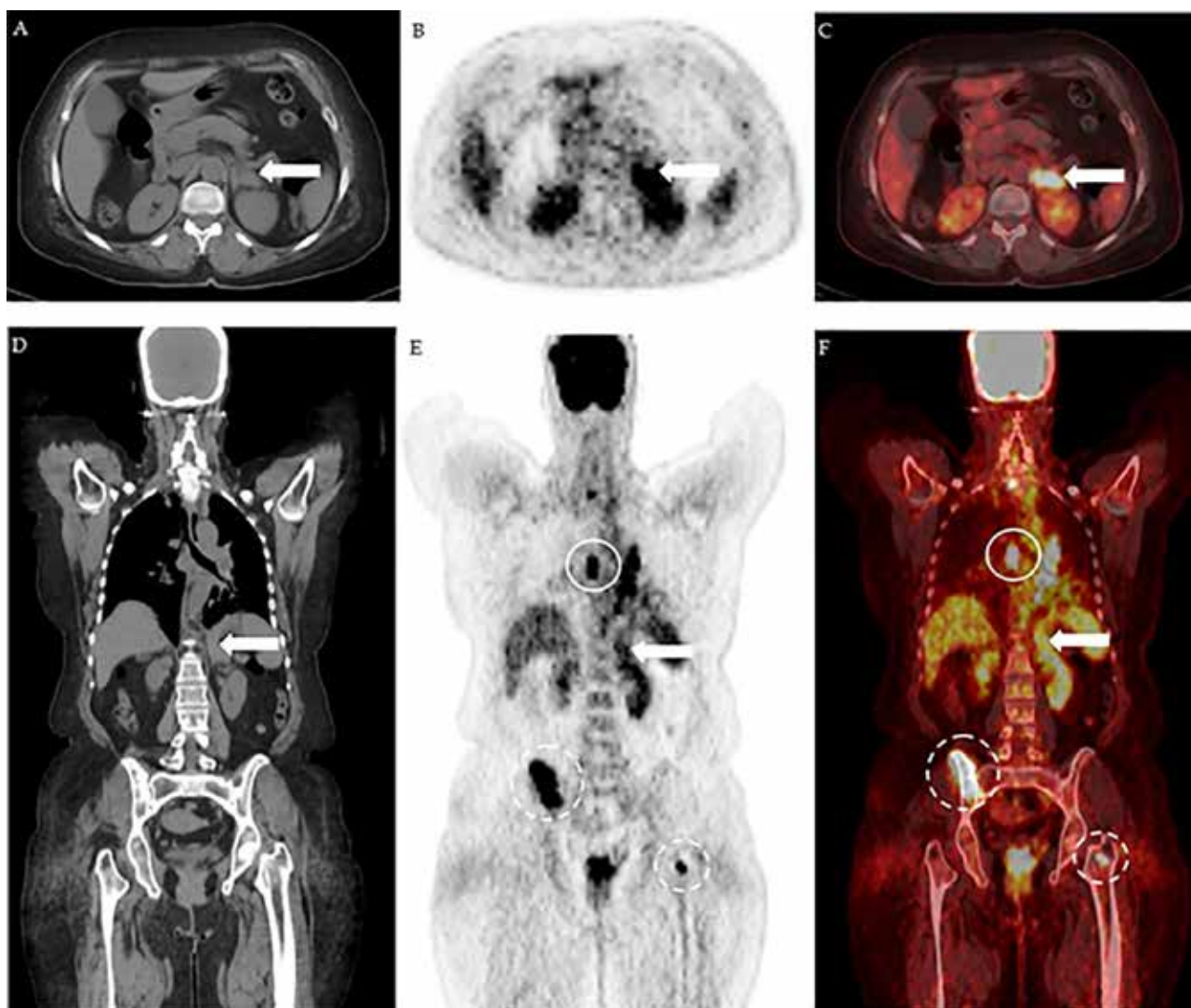


Figure 8. Adrenal metastasis is depicted on axial unenhanced CT (A), attenuation-corrected 18F-FDG PET (B) and fused PET/CT images (C). CT displays a well-circumscribed left adrenal tumor (arrow); increased 18F-FDG uptake is observed on PET and PET/CT. The primary lung cancer (continuous circle) and metastatic bone lesions (dashed circle) are seen on coronal plane of these images (D-F). (Refaat R, Elghazaly H. Employing 18F-FDG PET/CT for distinguishing benign from metastatic adrenal masses. *Egypt J Radiol Nucl Med* 2017; 48: 1065-1071)

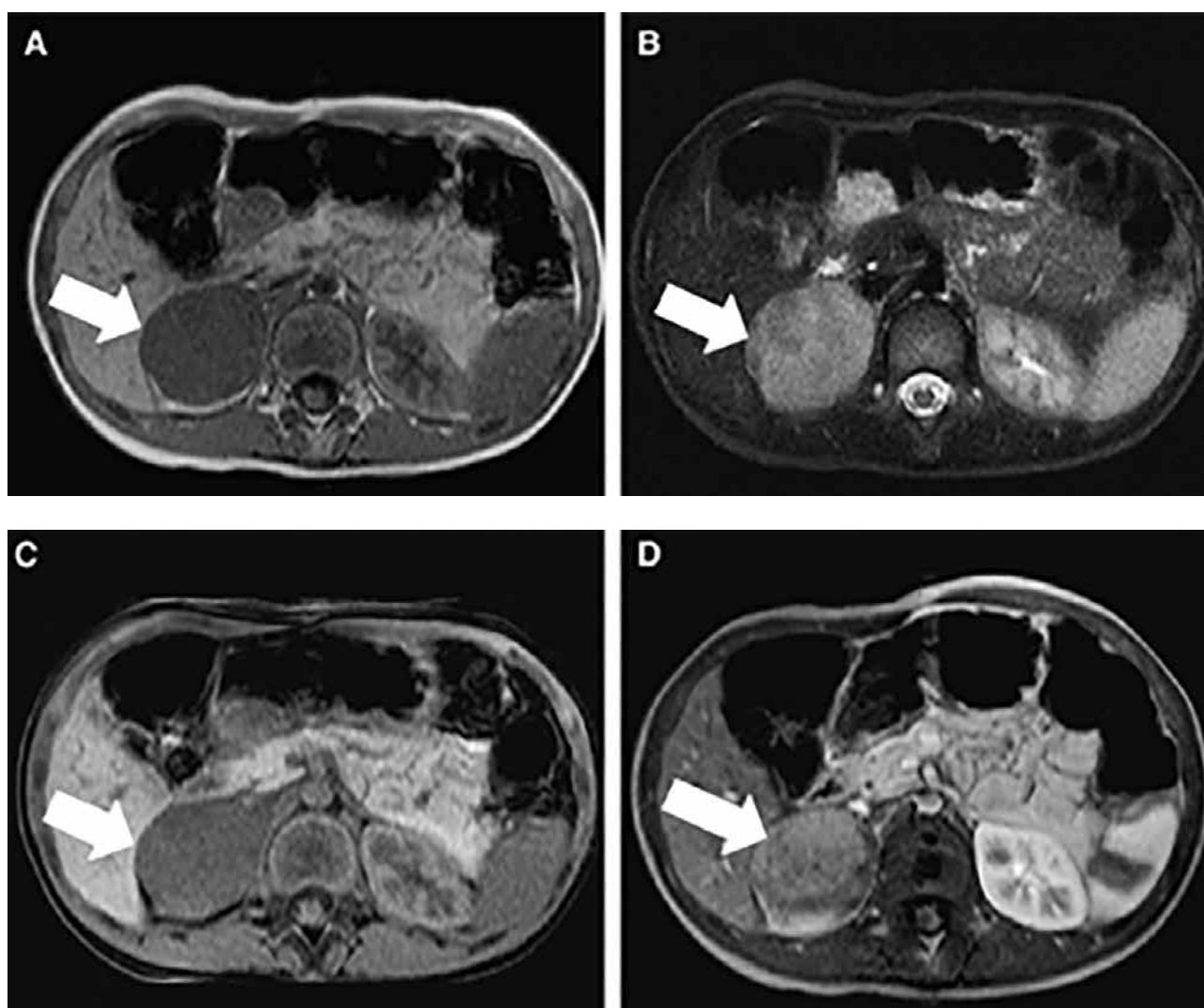


Figure 9. Ganglioneuroma (arrow) of the right adrenal gland is demonstrated as homogeneous and hypointense on MRI T1W image (A), heterogeneous and hyperintense on T2W image (B), homogeneous and isointense on fat-suppressed T1W image (C). After administration of the contrast agent, a slight and heterogeneous enhancement is observed (D). (Qing Y, Bin X, Jian W, Li G, Linhui W, Bing L, Huiqing W, Inghao S. Adrenal ganglioneuromas: a 10-year experience in a Chinese population. *Surgery* 2010; 147(6): 854-860)

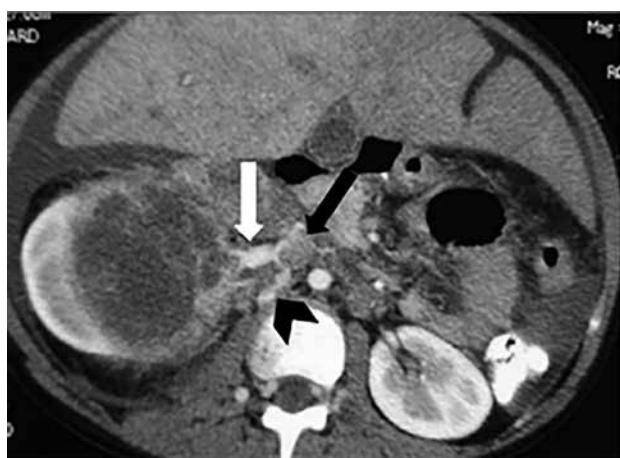


Figure 10. A heterogeneous hypoattenuated mass (white arrow), seen on axial contrast-enhanced CT, suggests a neuroblastoma. Thrombosis of the inferior vena cava (black arrow) is also displayed. It drains into a collateral vein (arrowhead). (Mehta SV, Lim-Dunham JE. Ultrasonographic appearance of pediatric abdominal neuroblastoma with inferior vena cava extension. *J Ultrasound Med* 2003; 22: 1091-1095)

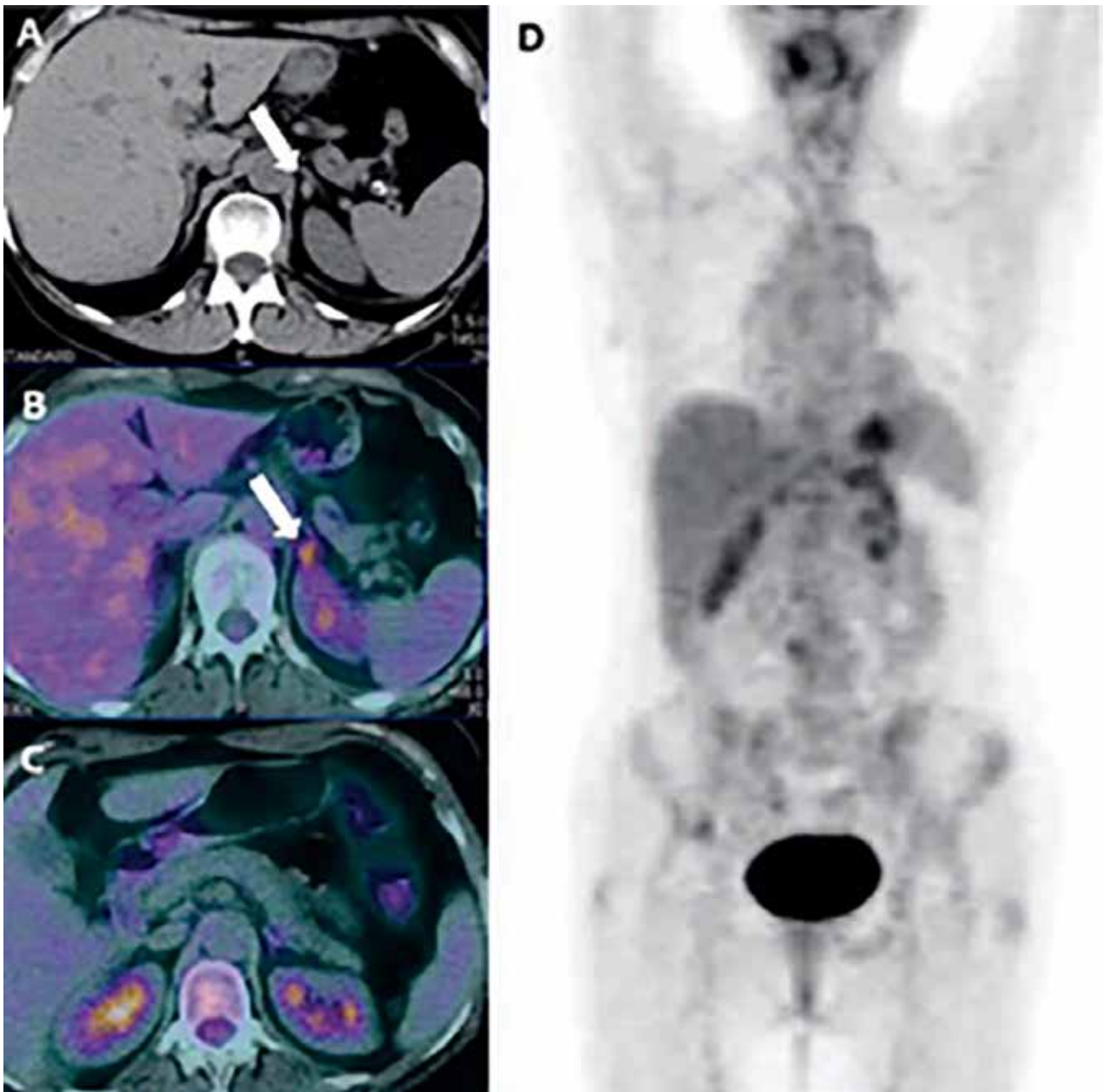


Figure 11. Increased 18F-FDG metabolic activity shows lymphoma of the left adrenal gland (arrow) on axial unenhanced CT (A) and 18F-FDG PET/CT (B). Resolution of the disease after chemotherapy is determined on axial PET/CT (C) and coronal PET (D) images. (Cistaro A, Asabella AN, Coppolino P, Quartuccio N, Altini C, Cucinotta M, Alongi P, Balma M, Sanfilippo S, Buschiazzi A et al. Diagnostic and prognostic value of 18F-FDG PET/CT in comparison with morphological imaging in primary adrenal gland malignancies – a multicenter experience. *Hell J Nucl Med* 2015; 18(2): 97-102)

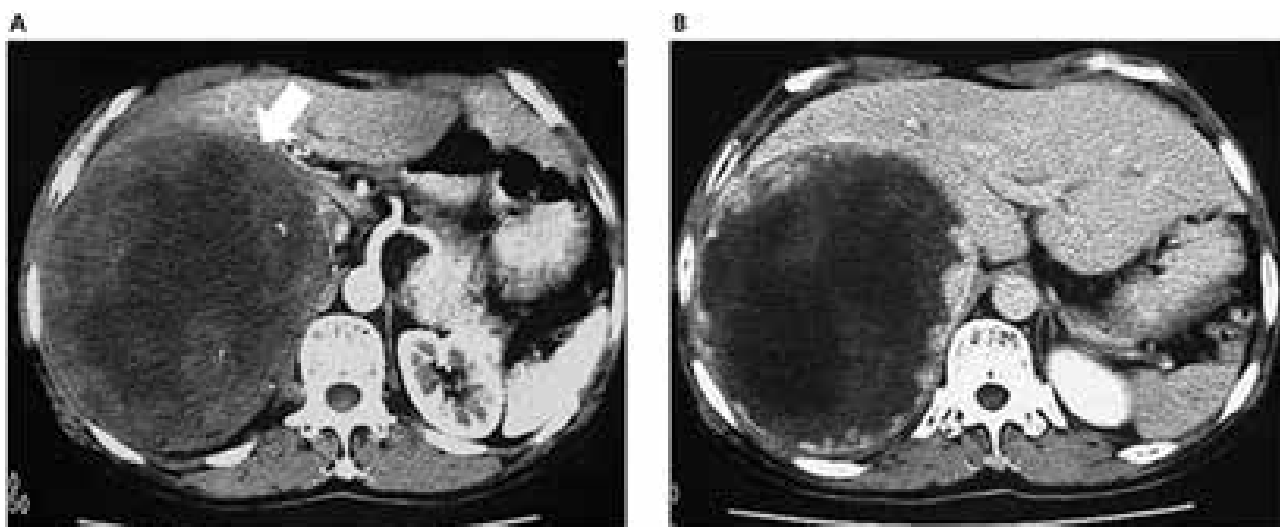


Figure 12. On axial DCE-CT, slight irregular peripheral enhancement and small calcifications during the arterial phase and more intense peripheral enhancement during the delayed phase within a mass (arrow) suggests a cavernous hemangioma of the right adrenal gland. (Xu HX, Liu GJ. Huge cavernous hemangioma of the adrenal gland. *J Ultrasound Med* 2003; 22: 523-526)



Figure 13. Coronal T2W MRI shows a multiloculated cystic mass (arrows) in the left adrenal gland (A). On contrast-enhanced fat-saturated T1W MRI, only enhancement of intratumoral septations (dashed arrows) is seen (B). Findings are characteristic of adrenal lymphangioma. (Secil M, Demir O, Yorukoglu K. MRI of adrenal lymphangioma: a case report. *Quant Imaging Med Surg* 2013; 3(6): 347-348)

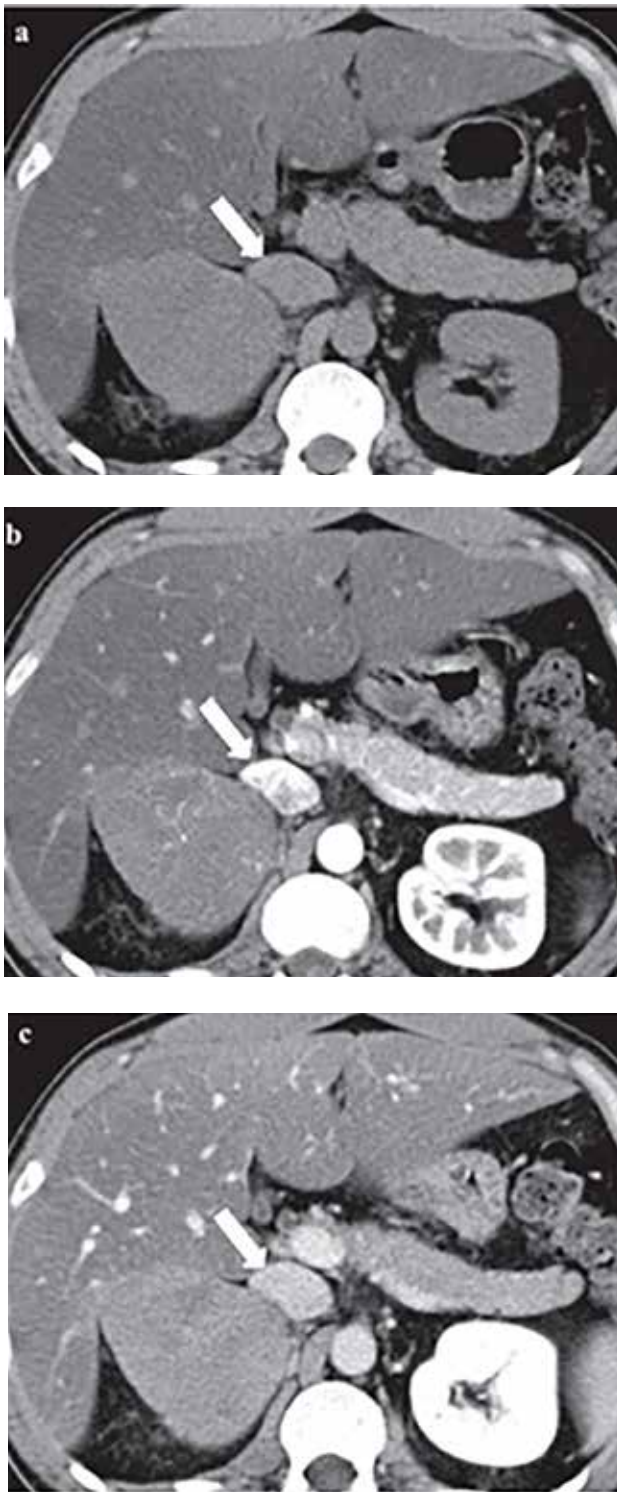


Figure 14. A well-defined homogeneous lesion (arrow) is displayed on axial native CT (A). After injection of the contrast material, slight enhancement of the tumor is observed during arterial phase (B) and delayed phase (C). These features are indicative of Schwannoma. (Suzuki K, Nakanishi A, Kurosaki Y, Nogaki J, Takaba E. Adrenal schwannoma: CT and MRI findings. *Radiat Med* 2007; 25: 299-302)

DISCUSSION

Adrenocortical adenomas are the most common adrenal neoplasms [3, 24]. These tumors are smaller than others [17, 25, 26] and they usually do not expand. In the case of adrenal adenoma, the mass is observed with cross-sectional imaging over time to detect possible changes in size. An increase of 1 cm is associated with a three times higher risk of a tumor being non-adenomatous [17].

On US, the findings are not specific. Adrenal adenoma is depicted as a small, well-defined solid lesion in the suprarenal region [27].

Histologically, adenoma contains a relatively high amount of intracytoplasmic lipid. This structural particularity is associated with lower attenuation value on native CT. A threshold of 10 HU is used to distinguish adenomas from non-adenomas. However, the quantity of intracellular fat may vary. As a result, imaging findings also differ. The majority of lipid-rich adenomas present as round hypoattenuating (< 10 HU) masses with regular margins on unenhanced CT [28, 29], contrary to lipid-poor adenomas and non-adenomatous tumors (> 10 HU) [25]. It is difficult, yet essential to separate lipid-poor adenomas from malignant lesions due to further diagnostic and treatment strategy. The presence of hyperdense foci (> 10 HU) within a mass requires more detailed assessment.

It should be noted that the 10 HU threshold has high sensitivity, although it lacks specificity. As stated by Iniguez-Ariza et al., a limit of 20 HU would decrease the number of false positive scans [7].

Moreover, the analysis of an unenhanced CT histogram is superior to the assessment of unenhanced mean attenuation. The former has higher sensitivity; a threshold of $> 10\%$ negative pixels is used for identifying adenoma [30, 31].

While hyperattenuating lipid-poor adenomas are difficult to differentiate from non-adenomatous lesions on native CT, they respond to contrast enhancement similarly to hypodense lipid-rich adenomas [25]. Higher enhancement, earlier and more rapid enhancement washout suggests adenomatous, either lipid-rich or lipid-poor, a tumor on DCE-CT (Figure 1) [12, 13, 25]. Still,

comparing lipid-rich adenomas to those containing a small amount of lipid, the former has slightly lower enhanced attenuation values, as well as delayed contrast-enhanced attenuation values [12, 25, 32].

There is minor overlap between washout patterns of adenomas and non-adenomas [12]. Hence, they are not pathognomonic.

For 10-min delayed CT, the thresholds of APW and RPW are 50% and 40%, respectively, indicating adrenocortical adenoma [33]. For 15-min delayed CT, the thresholds are 60% and 40%, accordingly [13, 25, 34, 35]. However, RPW and 15-min delayed CT is shown to be more precise [12, 17, 33]. RPW is usually lower in lipid-poor adenomas [32].

Perfusion CT is beneficial in the separation of adenomatous and non-adenomatous lesions as well; the adenomas demonstrate larger blood volume values [36, 37]. Nonetheless, perfusion CT is inferior to washout CT.

Considering that adrenal adenomas contain a relatively large amount of lipid, CS-MRI has become a valuable tool for discriminating them from the other tumors [38, 39]. Adenoma can be determined by decreased SI on T1-weighted (T1W) opposed-phase images compared to T1W in-phase images [40–44]. Indeed, this technique is less appropriate for lipid-poor adenomas.

Quantitative parameters can also be calculated using intratumoral SI on the in-phase and opposed-phase images. Adrenal-to-spleen ratio (ASR) and SI index (SII) are shown to be the most reliable parameters for the separation of adenomas and non-adenomas on CS-MRI [45]. $ASR < 0.71$ or $SII > 16.5\%$ is suggestive of lipid-rich adenoma [46, 47]. However, SII is more precise than ASR [47]. Considering the diagnostic possibilities of CS-MRI, it is far more superior to unenhanced CT [46], yet inferior to DCE-CT [48], especially for the characterization of lipid-poor adenomas. CS-MRI has a remarkable sensitivity if the attenuation value of the lesion is < 20 HU on native CT. In other cases, the sensitivity decreases [49].

A substantial overlap of apparent diffusion coefficient (ADC) values in adenomatous and non-adenomatous tumors are observed on DW-MRI [42, 50].

On dynamic contrast-enhanced MRI (DCE-MRI), the adrenocortical adenoma can be depicted by homogeneous enhancement on the arterial phase or capillary blush (increased SI higher than liver) with rapid washout on the venous phase [41, 43, 51]. In the case of lipid-poor adenoma, DCE-MRI is more valuable than CS-MRI due to inadequate SI loss on the opposed-phase. On the other hand, it should be used carefully in patients with decreased renal function owing to possible gadolinium-induced nephrogenic systemic fibrosis [52].

Lower 18F-FDG uptake of the lesion compared to uptake of the liver parenchyma indicates an adenoma on PET/CT [23, 53]. Still, there is a moderate overlap of 18F-FDG metabolic activity between adenomas and non-adenomas, e.g., hormone-secreting adenomas or those with large amounts of intracytoplasmic lipofuscin can mimic malignant adrenal neoplasms due to increased 18F-FDG uptake [54, 55].

Myelolipoma is the second most frequent adrenal incidentaloma [3]. It is always benign and mostly consists of adipocytes with some hematopoietic elements. However, fat is not an imperative element of the lesion. Although the majority of tumors are found in the adrenal gland, extra-adrenal myelolipomas are also identified [56–59].

Myelolipomas are encapsulated or have definite margins [60]. Atypical findings are hemorrhage or calcification within the mass [61–63]. They grow relatively slowly [64]. Nonetheless, the tumors tend to become larger; those who exceed 10 cm in diameter are known as giant myelolipomas. Bigger masses are likely to rupture and produce hematomas [65].

On US, myelolipoma is depicted as a heterogeneous hyperechoic or isoechogenic mass in the suprarenal region [62, 66–68]. Heterogeneity is a result of the variable architecture of the lesion. Low attenuation is characteristic of myeloid components. Therefore, hemopoietic cells determine the presence of hypoechogenic foci within the lipomatous tumor [68, 69].

Supersonic shear wave elastography may help distinguish myelolipomas from other benign adrenal masses; myelolipomas are harder than nodular hyperplasia or adenomas [70]. However, the US is insufficient in the diagnosis of myelolipoma.

A round or oval well-circumscribed heterogeneous hypodense lesion is observed in a case of myelolipoma on unenhanced CT [71, 72]. Negative attenuation values imply the presence of fat [68]. Hence, the attenuation of the tumor depends on the amount of the adipose tissue (Figure 2).

Mild enhancement is detected in the hematopoietic regions after the injection of the contrast material [72, 73].

On MRI, features typical of myelolipoma might vary. On T1W images, it can present as a homogeneous hyperintense or hypointense (if myeloid components predominate) mass with regular margins [71, 74]. On T2W images, high or intermediate SI is observed [22, 71].

Using fat-saturated T2W images, loss of SI within the fat allows identifying myelolipoma (Figure 3) [72].

A signal drop, which indicates the presence of adipose tissue, is also seen on opposed-phase CS-MRI [74].

Gadolinium-enhanced MRI displays mild enhancement of the tumor [72].

Metabolic activity of 18F-FDG is lower in fat compared to myeloid tissue [75]. Consequently, the uptake of 18F-FDG is usually not increased on PET/CT [76].

Pheochromocytoma is a rare adrenomedullary tumor derived from chromaffin cells. Extra-adrenal pheochromocytomas, termed as paragangliomas, arise from paraganglionic chromaffin cells in the sympathetic nervous system. Most patients with chromaffin-derived neoplasms have hereditary or de novo germline mutations in one of the susceptibility genes [77].

A portion of these masses secrete catecholamines. Thus, they can precipitate headache, cardiac arrhythmias or life-threatening hypertension since adrenergic crisis may occur during percutaneous biopsy [78, 79]. Laboratory tests along with radiological imaging play an essential role in the determination of pheochromocytoma and its function.

On native CT, around homogeneous or, mostly, heterogeneous lesion with possible calcification, cystic or hemorrhagic changes is observed in a case of pheochromocytoma [80–83]. Cystic degeneration and necrosis are more common in larger masses [84]. The attenuation of pheo-

chromocytoma is usually > 10 HU, and it does not significantly differ from the attenuation of lipid-poor adenoma [81, 85, 86]. However, compared to lipid-poor adenomas, pheochromocytomas are more extensive [85, 86]. If a malignant transformation has occurred, metastases in the regional lymph nodes or liver parenchyma can be detected [87].

DCE-CT is recommended as the first-line imaging tool in patients with suspected adrenomedullary neoplasm [88]. On DCE-CT, pheochromocytoma presents as a heterogeneous hyperdense lesion; its attenuation is higher than of adenoma [34, 86, 89]. Regions with no enhancement can be noticed if cystic or necrotic changes are present (Figure 4) [81]. The contrast agent washout of this tumor is variable. Lower APW and RPW are representative of pheochromocytoma rather than of adrenal adenoma [86]. Nonetheless, it can frequently imitate adenoma due to a similar washout pattern [81, 82, 84]. As stated by Woo et al., 35% of pheochromocytomas display early contrast enhancement and washout with coinciding APW and RPW [90]. Thus, the exclusion of this tumor should not be based only on the findings of the DCE-CT.

On T1W images, pheochromocytoma is hypointense. On T2W images, it is depicted as a solid, hypervascular, hyperintense mass [80]. However, it can mimic other benign or malignant tumors due to atypical features, such as fat, hemorrhage, cysts or calcification.

CS-MRI is also beneficial; SII $< 16.5\%$ and ASR SI ratio > 0.71 imply pheochromocytoma [86]. Nonetheless, if a tumor is larger, an SI drop correlating to a higher amount of intracytoplasmic lipid can be observed on opposed-phase images. DW-MRI may help differentiate pheochromocytomas from adenomas. The use of ADC in separating adrenal neoplasms has been debatable [91–93]. However, a new study shows that evaluating the heterogeneity of diffusion is more accurate. According to Umanodan et al., increased entropy of ADC values is characteristic to pheochromocytomas rather than adenomas [94]. Hemorrhage, necrosis or cystic changes are more frequent in pheochromocytomas, and these features determine the heterogeneity of the tumor. Therefore, a wider range of ADC values is seen in

the ADC histogram.

Avid heterogeneous enhancement is characteristic to pheochromocytoma on T1W gadolinium-enhanced images.

On PET/CT, pheochromocytoma is recognized by high uptake intensity compared to the liver parenchyma, regardless of the radioactive tracer (Figure 5) [95]. Still, 18F-FDG is the tracer of choice in diagnosing this adrenomedullary tumor [96]. Metabolic activity of the lesion helps to make a distinction between a benign and malignant pheochromocytoma. The latter is larger and has a higher 18F-FDG maximum standardized uptake value (SUVmax) [97].

Iodine-131-metaiodobenzylguanidine (131I-MIBG), another tracer, is taken up by catecholamine-secreting tumors. Thus, it is useful in the diagnosis of pheochromocytoma. 131I-MIBG, being a pharmacologic analog of guanethidine and norepinephrine, competes with endogenic amines in adrenergic tissues.

18F-FDG and 131I-MIBG scans complement one another in the identification of pheochromocytomas [97]. However, 18F-FDG PET/CT has higher sensitivity in detecting the dissemination of the disease [77]. Therefore, it should be used if the metastatic spread is suspected [88]. 18F-FDG PET/CT is useful in the diagnosis of pheochromocytoma, yet this imaging technique is inferior to CT or MRI [98].

Radioisotope gallium-68-DOTA-tyr3-octreotate (68Ga-DOTATATE) is presumably superior to 18F-FDG and 131I-MIBG. The use of 68Ga-DOTATATE PET/CT in conjunction with 18F-FDG PET/CT is beneficial in patients with the aggressive phenotype of the disease. In such a case, low 68Ga-DOTATATE and high 18F-FDG uptake are observed [95].

PET/CT with fluorine-18-dihydroxyphenylalanine (18F-DOPA) is valuable as well. As stated by Fiebrich et al., it is more sensitive than other imaging techniques in distinguishing catecholamine-secreting masses. Moreover, the metabolic activity of 18F-DOPA correlates with plasma and urine normetanephrine [99].

In spite of that, the uptake of radioactive tracers is predisposed not only by the location, malignancy or secretory function of pheochromocytoma but also by the underlying genetic status

[97, 100–102]. Consequently, the results of genetic testing should be taken into consideration while evaluating PET/CT images.

Primary carcinoma of the adrenal gland is a rare tumor, often found incidentally. Nevertheless, abdominal pain or a palpable mass can be present. Moreover, endocrine dysfunction, such as virilization, feminization or Cushing's syndrome, is frequently observed in patients with adrenocortical carcinoma [103, 104].

The prognosis of adrenal carcinoma is poor; the 5-year survival rate is approximately 50% [104, 105]. Older age, more significant lesion and metastatic spread is associated with malignancy and lower survival rate [7, 105].

Radiologic imaging enables to diagnose this aggressive neoplasm. On the US, a heteroechoic mass is detected in the adrenal gland [106].

On unenhanced CT, carcinoma presents as a round, oval or lobulated heterogeneous mass [107, 108]. The attenuation values of carcinoma are higher than of adenoma, although there is an overlap [28, 109]. Adrenocortical carcinoma may have a central hypodense region due to hemorrhage or necrosis (Figure 6). Additionally, hyperdense areas owing to calcification can be seen [110]. Infiltration to the adjacent tissue, including inferior vena cava liver or kidney, adenopathy, and metastasis helps to differentiate carcinoma from a benign tumor [110, 111].

After the injection of the contrast agent, inhomogeneous peripheral enhancement of the lesion is indicative of carcinoma [110]. RPW < 40% is consistent with malignancy [111, 112].

CT 3D reconstruction of the malignant lesion is valuable for evaluating its invasion and choosing the most suitable surgery plan [113, 114].

MRI is another useful imaging tool. A heterogeneous hyperintense mass is observed in a case of carcinoma on T1W and T2W images [22, 115, 116].

Intracytoplasmic lipid is not typical. Nonetheless, fatty regions within the tumor may be present in some cases. Thus, foci of decreased SI are seen on opposed-phase images.

18F-FDG PET/CT offers high diagnostic performance in separating malignant adrenal masses [26, 117]. Intense heterogeneous metabolic activity of 18F-FDG suggests carcinoma [115].

Using carbon-11-metomidate (11C-MTO) as a tracer, carcinoma can be differentiated from other adrenal lesions on PET. Extremely increased uptake of this radioactive isotope is characteristic of carcinoma, whereas pheochromocytoma and metastasis are 11C-MTO negative [118, 119]. Regions lacking the 11C-MTO uptake correlate to necrosis within the tumor (Figure 7). Nuclear medicine also contributes to the staging of the disease and follow-up after the treatment [120–122].

Primary tumors that disseminate to the adrenal glands are usually found in the lungs and esophagus [123–126]. Adrenal metastases are significantly larger than benign adrenal masses [127]. Nonetheless, other radiologic findings associated with malignancy are more valuable for diagnosis [124].

The US has low sensitivity in differentiating adrenal lesions. Still, it can be used, if other radiologic techniques are contraindicated. The metastatic tumor is recognized by its hypoechogenicity. On contrast-enhanced endoscopic US (CE-EUS), it appears as a hypervascular mass during the early vascular phase with delayed enhancement [128]. Adrenal metastasis presents as a solid hyperdense mass with smooth or irregular margins on native CT [123, 127, 129]. The majority of metastases are heterogeneous. However, this feature is not pathognomic [129, 130]. Regional lymphadenopathy, thrombosis of the renal vein or inferior vena cava and invasion of the adjacent tissues also allows differentiating malignant lesions from the benign ones. Furthermore, they show a higher and more rapid increase in size than benign lesions on follow-up images [129]. On DCE-CT, heterogeneous peripheral enhancement is observed [130].

Heterogeneous mass that is isointense on T1W images and hyperintense on T2W images implies the presence of metastasis.

CS-MRI demonstrates an insignificant signal drop on the opposed-phase images [43].

Gadolinium-enhanced MRI shows moderate and persistent peripheral enhancement without washout suggestive of metastasis [41, 43].

PET/CT is a precise, non-invasive imaging technique, although it has a lower accuracy than DCE-CT [23]. A combination of washout CT

and PET/CT is more accurate for the identification of metastasis than these imaging tools separately [123]. 18F-FDG uptake is higher or equal that of the liver in patients with metastatic foci (Figure 8) [21, 131–133]. These masses have higher 18F-FDG metabolic activity than benign lesions [21, 23]; SUVmax > 2.5 is characteristic of metastasis [125, 126, 134]. In some cases, the low metabolic activity of the radioisotope may be observed. This finding is associated with necrotic, hemorrhagic or especially small metastases [135].

A broad spectrum of masses, other than pheochromocytoma, arises from adrenomedullary ganglion cells. One of them, ganglioneuroma is a benign tumor. It originates from neural crest cells and consists of Schwann cells, ganglion cells, and nerve fibers. The majority of these masses are asymptomatic, therefore, they are found incidentally [136–138]. In other cases, patients experience abdominal discomfort or hypertension [137].

The radiologic features of ganglioneuroma are non-specific. On the US, it is depicted as a well-defined hypoechoic lesion, usually > 3 cm in size [136].

The blood flow signal is not established on Color Doppler US [136].

Unenhanced CT provides more information about the adrenal pathology. An oval or lobulated encapsulated lesion of low-attenuation, yet > 10 HU, is observed in patients with ganglioneuroma [136, 138–140]. Its homogeneity depends on the different proportions of Schwann cells and ganglions. CT may also display either central or peripheral speckled calcifications [136, 137, 140–142].

After the injection of the iodine-based contrast, low to intermediate delayed heterogeneous enhancement suggests a ganglioneuroma [136, 137, 142, 143].

Low SI on T1W images and high SI on T2W images are typical of ganglioneuroma (Figure 9) [136, 138, 139, 141, 144]. Nonetheless, it does not allow to differentiate ganglioneuroma from other neurogenic tumors.

DCE-MRI demonstrates weak delayed enhancement, as seen on DCE-CT [145, 146]. Still, MRI is inferior to CT owing to the ability of the latter

to showcase intratumoral calcifications [147].

Nuclear medicine can help identify the lesion, although the findings are not pathognomic. Metabolic activity of ^{18}F -FDG is frequently mildly increased [136, 142, 146], yet ganglioneuroma sometimes does not take up the radioisotope at all [138].

If ^{131}I -MIBG is used as a tracer, increased uptake can be observed.

Another tumor that originates from neural crest cells is neuroblastoma. It is a malignant mass common in the pediatric population [1]. Clinical symptoms characteristic of the tumor are irregular fever, abdominal pain or a palpable mass [148–150]. Neuroblastomas are extremely aggressive; the five-year overall survival rate is 50.8% [150]. However, in rare cases, neuroblastoma may undergo histological maturation into a benign ganglioneuroma [151].

A solid heterogeneously echoic lesion or an anechoic cystic mass is displayed on the US [152–156]. Bright echoes with acoustic shadowing, indicative of calcifications, may also be detected [156].

Native CT allows assessing the mass more scrupulously. Heterogeneous hypodense irregularly-shaped mass with granular calcifications is suggestive of neuroblastoma. Additionally, necrosis or cystic changes are frequent findings. Features, associated with malignancy, such as infiltration of the adjacent organs and lymphatic metastases, are also typical (Figure 10) [148].

Moderate inhomogeneous enhancement, except for the regions of necrosis and cystic changes, is seen on contrast-enhanced CT [148, 157].

On MRI, neuroblastoma presents as hypointense on T1W images and hyperintense on T2W images, identical to ganglioneuroma [149, 158, 159].

On gadolinium-enhanced MRI, heterogeneous enhancement of the mass is recognized [158].

Scintigraphy with ^{123}I MIBG or ^{131}I MIBG has become a valuable tool for the identification and staging of malignant neural crest tumors [160]. Increased MIBG uptake is determined in patients with neuroblastoma [161, 162]. Although, a false-negative scan may be occasionally observed [162]. Thus, ^{18}F -FDG PET is recommended owing to its higher sensitivity [163]. According to Kroiss et al., gallium-68-DO-

TA-tyr3-octreotide (^{68}Ga -DOTATOC) PET could also be helpful [164]. However, integrated imaging of MRI and PET further increases the accuracy in diagnosing neuroblastomas [165].

Ganglioneuroblastoma is a transitional mass which contains cells of both benign ganglioneuroma and malignant neuroblastoma. It is less differentiated than ganglioneuroma and is more related to neuroblastoma by its aggressive behavior. The main distinction between these two tumors is the regular margins of ganglioneuroblastoma and lower CT attenuation value due to its hypocellularity compared to neuroblastoma. Moreover, metastases are also more frequently observed in patients with neuroblastomas [166]. Imaging features of ganglioneuromas, ganglioneuroblastomas, and neuroblastomas do not significantly differ. Consequently, distinguishing neural crest tumors is possible only by a histological examination. However, a study shows that DW-MRI can be useful to separate these lesions. They are all hyperintense on DW-MRI. Nonetheless, ADC of malignant lesions is higher than of the benign ones [167].

Adrenal lymphoma, a rare tumor, can be primary or secondary. The most common histological type is non-Hodgkin lymphoma. Adrenal lymphoma occurs in 4% of the patients with non-Hodgkin lymphoma [168]. The mass usually presents with atypical symptoms, such as abdominal pain, fever or weight loss [169–171]. Radiologic imaging plays a notable role in the identification of the lesion. A heterogeneous hypoechoic mass with feasible hepatosplenomegaly can be determined on the US [172, 173]. However, the US lacks sensitivity in differentiating lymphoma from other adrenal malignant tumors.

On native CT, lymphoma is recognized as a round, oval or lobulated mass which is hypodense compared to the liver parenchyma, yet its attenuation value is > 10 HU [169, 174–176]. Rarely, calcifications within the mass can be seen [177]. Lymphoma is usually a well-defined lesion without invasion of the adjacent organs [178].

DCE-CT shows a slight gradual, heterogeneous enhancement [174, 175, 179].

Low to intermediate SI on MRI T1W images and high SI on T2W images is characteristic of adrenal lymphoma [178].

Using CS-MRI, a loss of SI is not visualized on opposed-phase images [174].

DW-MRI displays restricted diffusion within the lesion [179, 180].

On gadolinium-enhanced MRI, solid mass with homogeneous or heterogeneous contrast enhancement implies lymphoma [178–180]. In some cases, enlargement of the regional lymph nodes is established [181, 182].

PET/CT has higher accuracy in the differentiation of adrenal lymphoma than DCE-CT [117]. PET/CT images show avid 18F-FDG uptake in patients with lymphoma (Figure 11) [174, 183–185].

Cavernous hemangioma is an uncommon pathology of the adrenal gland; it usually affects skin and liver. Hemangioma is a benign vascular mass that consists of angioblastic cells. Due to their absent clinical manifestation, only enlarged (> 10 cm) hemangiomas are diagnosed clinically. Unfortunately, large hemangiomas may rupture and cause retroperitoneal hemorrhage, leading to hypotension [186].

Radiologic imaging determines the lesion accidentally in most cases. On the US, hemangioma appears as a well-defined hyperechoic inhomogeneous solid lesion in the suprarenal area [187, 188]. However, some patients present with a lesion that consists of diffuse anechoic regions with hyperechoic septa [189]. Intratumoral calcified foci may also be observed [188].

On unenhanced CT, a heterogeneous hypoattenuated lesion with regular margins and peripheral calcifications is characteristic of hemangioma [190–196].

The mass with the hypodense center is displayed on DCE-CT [192, 197]. Early irregular peripheral enhancement with enhancement extending to the center of the lesion during the delayed phase suggests an adrenal hemangioma (Figure 12) [189].

MRI does not show high sensitivity in the diagnosis of the tumor. The findings are non-specific, i.e., hemangioma is hypointense on T1W images and hyperintense on T2W images [187, 188, 198]. Regions of high SI within the mass are indicative of hemorrhage or calcification [190].

On opposed-phase CS-MRI, SI does not change significantly [190].

The enhancement pattern on DCE-MRI is similar to that on DCE-CT; early peripheral rim-like enhancement with slow patchy centripetal enhancement is determined [189, 190].

Lymphangioma is another benign tumor. Histologically, it is composed of multicystic owing to irregular dilated lymphatic vessels [199]. Lymphangiomas are frequently found in the neck, axilla, and mediastinum; adrenal lymphangioma is an extremely rare pathology. Adrenal masses are usually asymptomatic. However, abdominal or back pain can be present [199].

The US, as a primary imaging method, depicts the tumor as a well-defined multilocular anechoic cystic lesion [200–202].

Adrenal lymphangioma should be included in the differential diagnosis if a well-circumscribed hypodense mass with subtle septal structures is observed on native CT scans [203, 204]. Attenuation values are similar to those of lipid-rich adenomas. Nonetheless, only septal enhancement is seen after the administration of the contrast material in patients with lymphangioma [201, 204, 205]. Moreover, peripheral curvilinear or punctate calcifications may be recognized within lymphangiomas, contrary to adenomas [200, 204]. Lymphangioma appears hypointense on MRI T1W images and hyperintense on T2W images [206–208].

On gadolinium-enhanced MRI, isolated septal enhancement is typical of the tumor, correspondingly to DCE-CT images (Figure 13) [202]. Although radiologic imaging has become highly informative in distinguishing the adrenal tumors, malignant lesions remain in the differential diagnosis, if lymphangioma is present.

Adrenal schwannoma is a slowly growing benign mass. It arises from Schwann cells of myelinated sympathetic nerve fibers that innervate the adrenal medulla. Histologically, these tumors have two principal microscopic patterns of growth. The Antoni A pattern is highly cellular, the Antoni B pattern is composed of myxoid and hyaline degeneration. The tumor is usually asymptomatic [209–211]. When large, schwannomas develop degenerative (hemorrhagic or cystic) changes. These degenerative lesions are known as ancient schwannomas.

Schwannoma is frequently found incidental-

ly during the US examination. It is displayed as a hypoechoic mass with definite margins [212, 213].

On native CT, non-specific findings are observed in patients with adrenal schwannoma. The lesion is well-circumscribed heterogeneous and low-attenuated [214, 215]. Septa, cystic changes and calcification related to the tumor wall may be identified [214, 216, 217]. In such cases, schwannoma mimics a malignant tumor.

On DCE-CT, mild heterogeneous contrast enhancement during the hepatic arterial phase with progressive enhancement during the portal vein phase implies the presence of schwannoma (Figure 14) [212, 214, 215, 218].

Schwannoma is hypointense to isointense on MRI T1W images. On T2W images, it is inhomogeneous and hyperintense [211, 215, 218, 219]. T2W images are more informative; higher SI is characteristic of predominant Antoni B tissue rather than of Antoni A tissue [220].

The chemical shift sequence does not show a signal drop on opposed-phase images [215].

On DCE-MRI, schwannoma is identified by early enhancement without significant wash-out [221].

PET/CT demonstrates increased homogeneous or heterogeneous 18F-FDG uptake [222].

In conclusion, non-invasive radiologic imaging allows identifying typically asymptomatic tumors of the adrenal gland. Adrenal CT protocol is the most reliable technique in the differentiation of these diverse neoplasms. On the other hand, CS-MRI is indispensable for verifying intratumoral lipomatous components and, consequently, selecting the most appropriate approach to manage the mass. Furthermore, PET/CT permits characterizing indeterminate tumors and their potential metastatic spread. Nonetheless, some neoplasms do not display specific features and cannot be distinguished only based on radiologic imaging. Hence, clinical symptoms, laboratory test, and biopsy are essential for making a correct diagnosis.

REFERENCES

1. Lin X, Wu D, Chen C, Zheng N. Clinical characteristics of adrenal tumors in children: a retrospective review of a 15-year single-center experience. *Int Urol Nephrol* 2017; 49: 381–385.
2. Ahn SH, Kim JH, Baek SH, Kim H, Cho YY, Suh S, Kim BJ, H S, Koh JMK, Lee SH et al. Characteristics of adrenal incidentalomas in a large, prospective computed tomography-based multicenter study: the COAR study in Korea. *Yonsei Med J* 2018; 59(4): 501–510.
3. Bovio S, Cataldi A, Reimondo G, Sperone P, Novello S, Berruti A, Borasio P, Fava C, Dogliotti L, Scagliotti GV et al. Prevalence of adrenal incidentaloma in a contemporary computerized tomography series. *J Endocrinol Invest* 2006; 29: 298–302.
4. Paulsen SD, Nghiem HV, Korobkin M, Caoili EM, Higgins EJ. Changing role of imaging-guided percutaneous biopsy of adrenal masses: evaluation of 50 adrenal biopsies. *AJR* 2004; 182: 1033–1037.
5. Azoury SC, Nagarajan N, Young A, Mathur A, Prescott JD, Flshman EK, Zeiger MA. Computed tomography in the management of adrenal tumors: does size still matter? *J Comput Assist Tomogr* 2017; 41: 628–632.
6. Foo E, Turner R, Wang KC, Aniss A, Gill AJ, Sidhu S, Clifton-Bright R, Sywak M. Predicting malignancy in adrenal incidentaloma and evaluation of a novel risk stratification algorithm. *ANZ J Surg* 2018; 88: E173–177.
7. Iniguez-Ariza NM, Kohlenberg JD, Delivanis DA, Hartman RP, Dean DS, Thomas MA, Shah MZ, Herndon J, McKenzie TJ, Arlt W et al. Clinical, biochemical, and radiological characteristics of a single-center retrospective cohort of 705 large adrenal tumors. *Mayo Clin Proc Inn Qual Out* 2018; 2(1): 30–39.
8. Delivanis DA, Bancos I, Atwell TD, Schmit GD, Eiken PW, Natt N, Erickson D, Maraka S, Young Jr WF, Nathan MA. Diagnostic performance of unenhanced computed tomography and 18F-fluorodeoxyglucose positron emission tomography in indeterminate adrenal tumours. *Clin Endocrinol (Oxf)* 2018; 88: 30–36.
9. Mohamed RE, Sherif MF, Amin A. Differentiation of adrenal incidentalomas by qualitative and quantitative analytical data obtained by 18F-FDG positron emission tomography/ computed tomography in cancer patients. *Egypt J Radiol Nucl Med* 2018; 49: 764–775.
10. Dinnes J, Bancos I, Di Ruffano LE, Chortis V, Davenport C, Bayliss S, Sahdev A, Guest P, Fassnacht M, Deeks JJ et al. Imaging for the diagnosis of malignancy in incidentally discovered adrenal masses: a systematic review and meta-analysis. *Eur J Endocrinol* 2016; 175: R51–R64.
11. Mayo-Smith WW, Song JH, Boland GL, Francis IR, Israel GM, Mazzaglia PJ, Berland LL, Pandharipande PV. Management of incidental adrenal masses: a white paper of the ACR incidental findings committee. *J Am Coll Radiol* 2017; 14: 1038–1044.
12. Wang X, Li K, Sun H, Zhao J, Zheng L, Zhang Z, Bai R, Zhang G. Differentiation between adrenal adenomas and nonadenomas using dynamic contrast-enhanced computed tomography. *Oncotargets Ther* 2016; 9: 6809–6817.
13. Korobkin M, Brodeur FJ, Francis IR, Quint LE, Dunnick NR, Londy F. CT time-attenuation washout curves of adrenal adenomas and nonadenomas. *AJR* 1998; 170: 747–752.
14. Song J, Zhang C, Liu Q, Yu T, Jiang X, Xia Q, Zhang Y, Sequeiros RB. Utility of chemical shift and diffusion-weighted imaging in characterization of hyperattenuating adrenal lesions at 3.0T. *Eur J Radiol* 2012; 81: 2137–2143.
15. Leroy-Willig A, Bittoun A, Luton JP, Louvel A, Lefevre JE,

- Bonnin A, Roucayrol JC. In vivo MR spectroscopic imaging of the adrenal glands: distinction between adenomas and carcinomas larger than 15 mm based on lipid content. *AJR* 1989; 153: 771–773.
16. Wu YW, Tan CH. Determination of a cutoff attenuation value on single-phase contrast-enhanced CT for characterizing adrenal nodules via chemical shift MRI. *Abdom Radiol* 2016; 41: 1170–1177.
17. Koo HJ, Choi HJ, Kim HJ, Kim SO, Cho KS. The value of 15-minute delayed contrast-enhanced CT to differentiate hyperattenuating adrenal masses compared with chemical shift MR imaging. *Eur Radiol* 2014; 24: 1410–1420.
18. El-Kalioubie M, Emad-Eldin S, Abdelaziz O. Diffusion-weighted MRI in adrenal lesions: a warranted adjunct? *Egypt J Radiol Nucl Med* 2016; 47: 599–606.
19. Guerin C, Pattou F, Brunaud, Lifante JC, Mirallie E, Haissaguerre M, Huglo D, Olivier P, Houzard C, Ansquer C et al. Performance of 18F-FDG PET/CT in the characterization of adrenal masses in noncancer patients: a prospective study. *J Clin Endocrinol Metab* 2017; 102(7): 2465–2472.
20. Han SJ, Kim TS, Jeon SW, Jeong SJ, Yun M, Rhee Y, Kang ES, Cha BS, Lee EJ, Lee HC et al. Analysis of adrenal masses by 18F-FDG positron emission tomography scanning. *Int J Clin Pract* 2007; 61(5): 802–809.
21. Erasmus JJ, Patz Jr EF, McAdams HP, Murray JG, Herndon J, Coleman RE, Goodman PC. Evaluation of adrenal masses in patients with bronchogenic carcinoma using 18F-fluorodeoxyglucose positron emission tomography. *AJR* 1997; 168: 1357–1360.
22. Maurea S, Mainolfi C, Bazzicalupo L, Panico MR, Imparato C, Alfano B, Ziviello M, Salvatore M. Imaging of adrenal tumors using FDG PET: comparison of benign and malignant lesions. *AJR* 1999; 173: 25–29.
23. Park BK, Kim CK, Kim B, Choi JY. Comparison of delayed enhanced CT and 18F-FDG PET/CT in the evaluation of adrenal masses in oncology patients. *J Comput Assist Tomogr* 2007; 31(4): 550–556.
24. Song JH, Chaudhry FS, Mayo-Smith WW. The incidental adrenal mass on CT: prevalence of adrenal disease in 1,049 consecutive adrenal masses in patients with no known malignancy. *AJR* 2008; 190: 1163–1168.
25. Caoili EM, Korobkin M, Francis IR, Cohan RH, Dunnick NR. Delayed enhanced CT of lipid-poor adrenal adenomas. *AJR* 2000; 175: 1411–1415.
26. Humbert AL, Lecoanet G, Moog S, Bouderraoui F, Bresler L, Vignaud JM, Chevalier E, Brunaud L, Klein M, Cuny T. The computed tomography adrenal wash-out analysis properly classifies cortisol secreting adrenocortical adenomas. *Endocrine* 2018; 59: 529–537.
27. S. Goyal, Essentials of abdomino-pelvic sonography: a handbook for practitioners. 1st ed. Boca Raton, FL: CRC Press/Taylor & Francis Group, 2018.
28. Thomas AJ, Habra MA, Bhosale PR, Qayyum AA, Ahmed K, Vicens R, Elsayes KM. Interobserver agreement in distinguishing large adrenal adenomas and adrenocortical carcinomas on computed tomography. *Abdom Radiol* 2018; 43: 3101–3108.
29. Korobkin M, Brodeur FJ, Yutzy GG, Francis IR, Quint LE, Dunnick NR, Kazerooni EA. Differentiation of adrenal adenomas from nonadenomas using CT attenuation values. *AJR* 1996; 166: 531–536.
30. Ho LM, Paulson EK, Brady MJ, Wong TZ, Schindera ST. Lipid-poor adenomas on unenhanced CT: does histogram analysis increase sensitivity compared with a mean attenuation threshold? *AJR* 2008; 191: 234–238.
31. Jhaveri KS, Wong F, Ghai S, Haider MA. Comparison of CT histogram analysis and chemical shift MRI in the characterization of indeterminate adrenal nodules. *AJR* 2006; 187: 1303–1308.
32. Mosconi C, Vicennati V, Papadopoulos D, Di Dalmazi G, Morselli-Labate AM, Golfieri R, Pasquali R. Can imaging predict subclinical cortisol secretion in patients with adrenal adenomas? A CT predictive score. *AJR* 2009; 122–129.
33. Sangwaiya MJ, Boland GWL, Cronin CG, Blake MA, Halpern EF, Hahn PF. Incidental adrenal lesions: accuracy of characterization with contrast-enhanced washout multidetector CT – 10-minute delayed imaging protocol revisited in a large patient cohort. *Radiology* 2010; 256(2): 504–510.
34. Northcutt BG, Trakhtenbroit MA, Gomez EN, Fishman EK, Johnson PT. Adrenal adenoma and pheochromocytoma: comparison of multidetector CT venous enhancement levels and washout characteristics. *J Comput Assist Tomogr* 2016; 40: 194–200.
35. Mohamed RE, Abodewan KA, Amin MA. Diagnostic value of delayed washout rate of contrast-enhanced multi-detector computed tomography in adrenal incidentalomas. *Alexandria J Med* 2014; 50: 345–358.
36. Qin H, Sun H, Li Y, Shen B. Application of CT perfusion imaging to the histological differentiation of adrenal gland tumors. *Eur J Radiol* 2012; 81: 502–507.
37. Mohammed AR, Ahmed AT, Khalil TH, Refaie HF. Dynamic perfusion CT parameters and delayed contrast washout CT in characterization of adrenal tumors: a comparative study. *Egypt J Radiol Nucl Med* 2017; 48: 707–716.
38. Platzek I, Sieron D, Plodeck V, Borkowetz A, Laniado M, Hoffmann RT. Chemical shift imaging for evaluation of adrenal masses: a systematic review and meta-analysis. *Eur Radiol* 2019; 29(2): 806–817.
39. Hanna S, El-Kalioubie M, Badawy H, Halim M. Optimal diagnosis of adrenal masses. *Egypt J Radiol Nucl Med* 2015; 46: 511–520.
40. Bilbey JH, McLoughlin RF, Kurkjian PS, Wilkins GEL, Chan NHL, Schmidt N, Singer J. MR imaging of adrenal masses: value of chemical-shift imaging for distinguishing adenomas from other tumors. *AJR* 1995; 164: 637–642.
41. Chung JJ, Semelka RC, Martin DR. Adrenal adenomas: characteristic postgadolinium capillary blush on dynamic MR imaging. *J Magn Reson Imaging* 2001; 13: 242–248.
42. Miller FH, Wang Y, McCarthy RJ, Yaghmai V, Merrick L, Larson, Berggruen S, Casalino DD, Nikolaidis P. Utility of diffusion-weighted MRI in characterization of adrenal lesions. *AJR* 2010; 194: W179–W185.
43. Rodacki K, Ramalho M, Dale BM, Battisti S, de Campos ROP, Giardino A, Semelka RC. Combined chemical shift imaging with early dynamic serial gadolinium-enhanced MRI in the characterization of adrenal lesions. *AJR* 2014; 203: 99–106.
44. Slapa RZ, Jakubowski W, Januszewicz A, Kasperlik-Zaluska AA, Dabrowska E, Fijuth J, Feltynowski T, Tarnawski R, Krolicki L. Discriminatory power of MRI for differentiation of adrenal non-adenomas vs adenomas evaluated by means of ROC analysis: can biopsy be obviated? *Eur Radiol* 2000; 10: 95–104.
45. Afifi AH, Shafy HLA, Ramadan AA, Ataa MA, Assad SN. Role of quantitative chemical shift magnetic resonance imaging and chemical shift subtraction technique in discriminating adenomatous from non adenomatous adrenal solid lesions. *Egypt J Radiol Nucl Med* 2017; 48: 271–284.
46. Israel GM, Korobkin M, Wang C, Hecht EN, Krinsky GA.

Comparison of unenhanced CT and chemical shift MRI in evaluating lipid-rich adrenal adenomas. *AJR* 2004; 183: 215–219.

47. Fujiyoshi F, Nakajo M, Fukukura Y, Tsuchimochi S. Characterization of adrenal tumors by chemical shift fast low-angle shot MR imaging: comparison of four methods of quantitative evaluation. *AJR* 2003; 180: 1649–1657.

48. Warda MHA, Shehata SM, Zaiton F. Chemical-shift MRI versus washout CT for characterizing adrenal incidentalomas. *J Clin Imaging* 2016; 40: 780–787.

49. Seo JM, Park BK, Park SY, Kim CK. Characterization of lipid-poor adrenal adenoma: chemical-shift MRI and washout CT. *AJR* 2014; 202: 1043–1050.

50. Cicekci M, Onur MR, Aydin AM, Gul Y, Ozkan Y, Akpolat N, Kocakoc E. The role of apparent diffusion coefficient values in differentiation between adrenal masses. *J Clin Imaging* 2014; 38: 148–153.

51. Becker-Weidman D, Kalb B, Mittal PK, Harri PA, Arif-Tiwari H, Farris AB, Chen Z, Sungjin K, Martin DR. Differentiation of lipid-poor adrenal adenomas from non-adenomas with magnetic resonance imaging: utility of dynamic, contrast enhancement and single-shot T2-weighted sequences. *Eur J Radiol* 2015; 84: 2045–2051.

52. Schieda N, Blaichman JI, Costa AF, Glikstein R, Hurrell C, James M, Maralani PJ, Shabana W, Tang A, Tsampalieros A et al. Gadolinium-based contrast agents in kidney disease: a comprehensive review and clinical practice guideline issued by the Canadian association of radiologists. *Can J of Kidney Health Dis* 2018; 5: 1–17.

53. Boland GWL, Blake MA, Holalkere NS, Hahn PF. PET/CT for the characterization of adrenal masses in patients with cancer: qualitative versus quantitative accuracy in 150 consecutive patients. *AJR* 2009; 192: 956–962.

54. Papadakis GZ, Millo C, Stratakis CA. Benign hormone-secreting adenoma within a larger adrenocortical mass showing intensely increased activity on 18F-FDG PET/CT. *Endocrine* 2016; 54(1): 269–270.

55. Matsumoto S, Hosoya Y, Lefor AK, Haruta H, Ui T, Kurashina K, Saito S, Ashizawa K, Sasaki T, Kitayama et al. A black adrenal adenoma with high FDG uptake on PET/CT scan in a patient with esophageal carcinoma: a case report. *Int J Surg Case Rep* 2018; 44: 118–121.

56. Sagan D, Zdunek M, Korobowicz E. Primary myelolipoma of the chest wall. *Ann Thorac Surg* 2009; 88: e39–e41.

57. Karam AR, Nugent W, Falardeau J, Desai D, Khan A, Shankar S. Multifocal extra-adrenal myelolipoma arising in the greater omentum. *Radiology Case* 2009; 3(11): 20–23.

58. Omdal DG, Baird DE, Burton BS, Goodhue Jr WW, Giddens EM. Myelolipoma of the thoracic spine. *AJNR* 1997; 18: 977–979.

59. Kumar M, Duerinckx AJ. Bilateral extraadrenal perirenal myelolipomas: an imaging challenge. *AJR* 2004; 183: 833–836.

60. Ketelsen D, von Weyhern CH, Horger M. Diagnosis of bilateral giant adrenal myelolipoma. *J Clin Oncol* 2010; 28(33): e678–e679.

61. Chung HM, Luo FJ, Wu TM, Tsai YC. Adrenal myelolipoma with spontaneous hemorrhage. *Urol Sci* 2010; 21(3): 152–154.

62. Behan M, Martin EC, Muecke EC, Kazam E. Myelolipoma of the adrenal: two cases with ultrasound and CT findings. *AJR* 1977; 129: 993–996.

63. Lam KY, Lo CY. Adrenal lipomatous tumours: a 30 year clinico-pathological experience at a single institution. *J Clin Pathol* 2001; 54: 707–712.

64. Campbell MJ, Obasi M, Wu B, Corwin MT, Fananapazir G. The radiographically diagnosed adrenal myelolipoma: what do

we really know? *Endocrine* 2017; 58: 289–294.

65. Amano T, Takemae K, Niikura S, Kouno M, Amano M. Retroperitoneal hemorrhage due to spontaneous rupture of adrenal myelolipoma. *Int J Urol* 1999; 6: 585–588.

66. Lesbats-Jacquot V, Cucchi JM, Amoretti N, Novellas S, Chevallier P, Bruneton JN. Lipomatous tumors of the adrenals — a report on 18 cases and review of the literature. *Clin Imaging* 2007; 31: 335–339.

67. Yildiz L, Akpolat I, Erzurumlu K, Aydin O, Kandemir B. Giant adrenal myelolipoma: case report and review of the literature. *Pathol Int* 2000; 50: 502–504.

68. Musante F, Derchi LE, Zappasodi F, Bazzocchi M, Riviezzo GC, Banderali A, Cicio GR. Myelolipoma of the adrenal gland: sonographic and CT features. *AJR* 1988; 151: 961–964.

69. Sandoval MAS, Anel-Quimpo J. A giant myelolipoma discovered as an adrenal incidentaloma: radiological, endocrine and pathological evaluation. *BMJ Case Rep* 2010; doi:10.1136/bcr.05.2010.3005.

70. Slapa RZ, Kasperlik-Zaluska AA, Migda B, Otto M, Jakubowski WS. Application of parametric ultrasound contrast agent perfusion studies for differentiation of hyperplastic adrenal nodules from adenomas — initial study. *Eur J Radiol* 2015; 84: 1432–1435.

71. Hsu S, Shu K, Lee WC, Cheng YT, Chiang PH. Adrenal myelolipoma: a 10-year single-center experience and literature review. *Kaohsiung J Med Sci* 2012; 28: 377–382.

72. Littrell LA, Carter JM, Broski SM, Wenger DE. Extra-adrenal myelolipoma and extramedullary hematopoiesis: imaging features of two similar benign fat-containing presacral masses that may mimic liposarcoma. *Eur J Radiol* 2017; 93: 185–194.

73. Anis-ul-islam M, Qureshi AH, Zaidi SZ. Adrenal myelolipoma in a young male — a rare case scenario. *J Pak Med Assoc* 2016; 66(3): 342–344.

74. Hakim A, Rozeik C. Adrenal and extra-adrenal myelolipomas - a comparative case report. *Radiology Case* 2014; 8(1): 1–12.

75. Rowe SP, Javadi MS, Solnes LB, Fishman EK. Appearance of adrenal myelolipomas on 2-deoxy-2-(18F)fluoro-D-glucose positron emission tomography-computed tomography. *World J Nucl Med* 2017; 16(4): 271–274.

76. Gemmel F, Bruinsma H, Oomen P, Collins J. PET/CT incidental detection of bilateral adrenal myelolipomas in a patient with a huge maxillary sinus carcinoma. *Clin Nucl Med* 2010; 35: 132–133.

77. Babic B, Patel D, Aufforth R, Assadipour Y, Sadowski SM, Quezada M, Nilubol N, Prodanov T, Pacak K, Kebebew E. Pediatric patients with pheochromocytoma and paraganglioma should have routine preoperative genetic testing for common susceptibility genes and imaging to detect extra-adrenal and metastatic tumors. *Surgery* 2017; 161(1): 220–227.

78. Vanderveen KA, Thompson SM, Callstrom MR, Young Jr WF, Grant CS, Farley DR, Richards ML, Thompson GB. Biopsy of pheochromocytomas and paragangliomas: potential for disaster. *Surgery* 2009; 146(6): 1158–1166.

79. Casola G, Nicolet V, van Sonnenberg E, Withers C, Bretagnolle M, Saba RM, Bret PM. Unsuspected pheochromocytoma: risk of blood-pressure alterations during percutaneous adrenal biopsy. *Radiology* 1986; 159(3): 733–735.

80. Blake MA, Kalra MK, Maher MM, Sahani DV, Sweeney AT, Mueller PER, Hahn PF, Boland GW. Pheochromocytoma: an imaging chameleon. *RadioGraphics* 2004; 24:S87–S99.

81. Park BK, Kim CK, Kwon GY, Kim JH. Re-evaluation of phe-

- ochromocytomas on delayed contrast-enhanced CT: washout enhancement and other imaging features. *Eur Radiol* 2007; 17: 2804–2809.
82. Blake MA, Krishnamoorthy SK, Boland GW, Sweeney AT, Pitman MB, Harisinghani M, Mueller PR, Hahn PF. Low-density pheochromocytoma on CT: a mimicker of adrenal adenoma. *AJR* 2003; 181: 1663–1668.
83. Patel J, Davenport MS, Cohan RH, Caoili EM. Can established CT attenuation and washout criteria for adrenal adenoma accurately exclude pheochromocytoma? *AJR* 2013; 201: 122–127.
84. Kim DW, Yoon SK, Kim SH, Kang EJ, Kwon HJ. Assessment of clinical and radiologic differences between small and large adrenal pheochromocytomas. *Clin Imag* 2017; 43: 153–157.
85. Zhang GMY, Shi B, Sun H, Jin ZY, Xue HD. Differentiating pheochromocytoma from lipid-poor adrenocortical adenoma by CT texture analysis: feasibility study. *Abdom Radiol* 2017; 42: 2305–2313.
86. Schieda N, Alrashed A, Flood TA, Samji K, Shabana W, McInnes MDF. Comparison of quantitative MRI and CT washout analysis for differentiation of adrenal pheochromocytoma from adrenal adenoma. *AJR* 2016; 206: 1141–1148.
87. Huang KH, Chung SD, Chen SC, Chueh SC, Pu YS, Lai MK, Lin WC. Clinical and pathological data of 10 malignant pheochromocytomas: long-term follow up in a single institute. *Int J Urol* 2007; 14: 181–185.
88. Lenders JWM, Duh QY, Eisenhofer G, Gimenez-Roqueplo AP, Grebe SKG, Murad MH, Naruse M, Pacak K, Young Jr WF. Pheochromocytoma and paraganglioma: an endocrine society clinical practice guideline. *J Clin Endocrinol Metab* 2014; 99(6): 1915–1942.
89. Northcutt BG, Raman SP, Long C, Oshmyansky AR, Siegelman SS, Fishman EK, Johnson PT. MDCT of adrenal masses: can dual-phase enhancement patterns be used to differentiate adenoma and pheochromocytoma? *AJR* 2013; 201: 834–839.
90. Woo S, Suh CH, Kim SY, Cho JY, Kim SH. Pheochromocytoma as a frequent false-positive in adrenal washout CT: a systematic review and meta-analysis. *Eur Radiol* 2018; 28: 1027–1036.
91. Timmers HJLM, Chen CC, Carrasquillo JA, Whatley M, Ling A, Eisenhofer G, King KS, Rao JU, Wesley RA, Adams KT et al. Staging and functional characterization of pheochromocytoma and paraganglioma by 18F-fluorodeoxyglucose (18F-FDG) positron emission tomography. *J Natl Cancer Inst* 2012; 104: 700–708.
92. Nakajo M, Nakajo M, Fukurura Y, Jinguji M, Shindo T, Nakabeppu Y, Kamimura K, Yoneyama T, Takumi K, Yoshiura T. Diagnostic performances of FDG-PET/CT and diffusion-weighted imaging indices for differentiating benign pheochromocytoma from other benign adrenal tumors. *Abdom Imaging* 2015; 40: 1655–1665.
93. Hida T, Nishie A, Asayama Y, Ishigami K, Ushijima Y, Takayama Y, Fujita N, Shimamoto D, Yokomizo A, Tatsugami K et al. Apparent diffusion coefficient characteristics of various adrenal tumors. *Magn Reson Med* 2014; 13(3): 183–189.
94. Umanodan T, Fukukura Y, Kamagae Y, Shindo T, Nakajo M, Takumi K, Nakajo M, Hakamada H, Umanodan A, Yoshiura T. ADC histogram analysis for adrenal tumor histogram analysis of apparent diffusion coefficient in differentiating adrenal adenoma from pheochromocytoma. *J Magn Reson Imaging* 2017; 45: 1195–1203.
95. Chang CA, Pattison DA, Tothil RW, Kong G, Akhurst TJ, Hicks RJ, Hofman MS. 68Ga-DOTATATE and 18F-FDG PET/CT in paraganglioma and pheochromocytoma: utility, patterns and heterogeneity. *Cancer Imaging* 2016; 16(1): 22. doi 10.1186/s40644-016-0084-2.
96. Timmers HJLM, Chen CC, Carrasquillo JA, Whatley M, Ling A, Havekes B, Eisenhofer G, Martiniova L, Adams KT, Pacak K. Comparison of 18F-fluoro-L-DOPA, 18F-fluoro-deoxyglucose, and 18F-fluorodopamine PET and 123I-MIBG scintigraphy in the localization of pheochromocytoma and paraganglioma. *J Clin Endocrinol Metab* 2009; 94(12): 4757–4767.
97. Tiwari A, Shah N, Sarathi V, Malhotra G, Bakshi G, Prakash G, Khadilkar K, Pandit R, Lila A, Bandgar T. Genetic status determines 18F-FDG uptake in pheochromocytoma/paraganglioma. *J Med Imaging Radiat Oncol* 2017; 61: 745–752.
98. Timmers HJLM, Chen CC, Carrasquillo JA, Whatley M, Ling A, Eisenhofer G, King KS, Rao JU, Wesley RA, Adams KT et al. Staging and functional characterization of pheochromocytoma and paraganglioma by 18F-fluorodeoxyglucose (18F-FDG) positron emission tomography. *J Natl Cancer Inst* 2012; 104: 700–708.
99. Fiebrich HB, Brouwers AH, Kerstens MN, Pijl MEJ, Kema IP, de Jong JR, Jager PL, Elsinga PH, Dierckx RA, van der Wal JE et al. 16-F-18-fluoro-L-dihydroxyphenylalanine positron emission tomography is superior to conventional imaging with 123I-metaiodobenzylguanidine scintigraphy, computer tomography, and magnetic resonance imaging in localizing tumors causing catecholamine excess. *J Clin Endocrinol Metab* 2009; 94: 3922–3930.
100. Taieb D, Jha A, Guerin C, Pang Y, Adams KT, Chen CC, Romanet P, Roche P, Essamet W, Ling A et al. 18F-FDOPA PET/CT imaging of MAX-related pheochromocytoma. *J Clin Endocrinol Metab* 2018; 103(4): 1574–1582.
101. Feral CC, Tissot FS, Tosello L, Fakhry N, Sebag F, Pacak K, Taieb D. 18F-fluorodihydroxyphenylalanine PET/CT in pheochromocytoma and paraganglioma: relation to genotype and amino acid transport system L. *Eur J Nucl Med Mol Imaging* 2017; 44: 812–821.
102. Amodru V, Guerin C, Delcourt S, Romanet P, Loundou A, Viana B, Bru T, Castinetti F, Sebag F, Pacak K, Taieb et al D. Quantitative 18 F-DOPA PET/CT in pheochromocytoma: the relationship between tumor secretion and its biochemical phenotype. *Eur J Nucl Med Mol Imaging* 2018; 45: 278–282.
103. Wieneke JA, Thompsom LDR, Heffess CS. Adrenal cortical neoplasms in the pediatric population. *Am J Surg Pathol* 2003; 27(7): 867–881.
104. Michalkiewicz E, Santrini R, Figueiredo B, Miranda ECM, Caran E, Oliveria-Filho AG, Marques R, Pianovski MAD, Lacerda L, Cristofani LM et al. Clinical and outcome characteristics of children with adrenocortical tumors: a report from the international pediatric adrenocortical tumor registry. *J Clin Oncol* 2004; 22: 838–845.
105. Gupta N, Rivera M, Novotny P, Rodriguez V, Bancos I, Lteif A. Adrenocortical carcinoma in children: a clinicopathological analysis of 41 patients at the Mayo clinic from 1950 to 2017. *Horm Res Paediatr* 2018; 90: 8–18.
106. Yadav P, Arora S, Srivastava D, Lal H. Adrenocortical carcinoma with inferior vena cava tumour thrombus: multidetector CT (MDCT) evaluation and management. *BMJ Case Rep* 2015; doi:10.1136/bcr-2015- 213073.
107. Jiang M, Ding H, Li C, Xiang K, Tang J, Guo Y, Zhang S. Surgical resection of adrenocortical carcinoma with invasion into the inferior vena cava: a case report and literature review. *Clinical Case Reports* 2017; 5(12): 1934–1937.
108. Hussain S, Beldegrun A, Seltzer SE, Richie JP, Gittes RF, Abrams HL. Differentiation of malignant from benign adrenal masses: predictive indices on computed tomography. *AJR* 1985; 144: 61–65.
109. Petersenn S, Richter PA, Broemel T, Ritter CO, Deutschbein

- T, Bell FU, Allolio B, Fassnacht M. Computed tomography criteria for discrimination of adrenal adenomas and adrenocortical carcinomas: analysis of the German ACC registry. *Eur J Endocrinol* 2015; 172(4): 415-422.
110. Fishman EK, Deutch BM, Hartman DS, Goldman SM, Zerhouni EA, Siegelman SS. Primary adrenocortical carcinoma: CT evaluation with clinical correlation. *AJR* 1987; 148: 531-535.
111. Zhang HM, Perrier ND, Grubbs EG, Sircar K, Ye ZX, Lee JE, Ng CS. CT features and quantification of the characteristics of adrenocortical carcinomas on unenhanced and contrast-enhanced studies. *Clin Radiol* 2012; 67(1): 38-46.
112. Slattery JMA, Blake MA, Kalra MK, Misdrabi J, Sweeney AT, Copeland PM, Mueller PER, Boland GW. Adrenocortical carcinoma: contrast washout characteristics on CT. *AJR* 2006; 187: W21-W24.
113. Chen L, Zeng X, Li S, Gong C, Peng E, Wu B, Zhang W, Zhang Y. Evaluation of a large adrenal carcinoma with 3D reconstruction of computed tomography images: a case report and literature review. *J X-Ray Sci Technol* 2016; 24: 665-671.
114. Mitterberger MM, Pinggera GM, Peschel R, Bartsch G, Pallwein L, Frauscher F. The use of three-dimensional computed tomography for assessing patients before laparoscopic adrenal-sparing surgery. *BJU Int* 2006; 98: 1068-1073.
115. Belmihoub I, Silvera S, Sibony M, Dousset B, Legmann P, Bertagna X, Bertherat J, Assie G. From benign adrenal incidentaloma to adrenocortical carcinoma: an exceptional random event. *Eur J Endocrinol* 2017; 176: K15-K19.
116. Nogueira TM, Lirov R, Caoili EM, Lerario AM, Miller BS, Fragoso MCBV, DUnnick NR, Hammer GD, Else T. Radiographic characteristics of adrenal masses preceding the diagnosis of adrenocortical cancer. *Horm Canc* 2015; 6: 176-181.
117. Cistaro A, Asabella AN, Coppolino P, Quartuccio N, Altini C, Cucinotta M, Alongi P, Balma M, Sanfilippo S, Buschiazio et al. Diagnostic and prognostic value of 18F-FDG PET/CT in comparison with morphological imaging in primary adrenal gland malignancies – a multicenter experience. *Hell J Nucl Med* 2015; 18(2): 97-102.
118. Hennings J, Lindhe O, Bergstrom M, Langstrom B, Sundin A, Hellman P. 11C-Metomidate positron emission tomography of adrenocortical tumors in correlation with histopathological findings. *J Clin Endocrinol Metab* 2006; 91: 1410-1414.
119. Minn H, Salonen A, Friberg J, Roivainen A, Viljanen T, Langsjo J, Salmi J, Valimaki M, Nagren K, Nuutila P. Imaging of adrenal incidentalomas with PET using 11C-metomidate and 18F-FDG. *J Nucl Med* 2004; 45(6): 972-980.
120. Khan TS, Sundin A, Juhlin C, Langstrom B, Bergstrom M, Eriksson B. 11C-metomidate PET imaging of adrenocortical cancer. *Eur J Nucl Med* 2003; 30: 403-410.
121. Ardito A, Massaglia C, Pelosi E, Zaggiia B, Basile V, Brambilla R, Vigna-Taglianti F, Duregon E, Arena V, Perotti P, Penna D, Terzolo M. 18F-FDG PET/CT in the post-operative monitoring of patients with adrenocortical carcinoma. *Eur J Endocrinol* 2015; 173(6): 749-756.
122. Takeuchi S, Balachandran A, Habra MA, Phan AT, Bassett Jr RL, Macapinlac HA, Chuang HH. Impact of 18F-FDG PET/CT on the management of adrenocortical carcinoma: analysis of 106 patients. *Eur J Nucl Med Mol Imaging* 2014; 41: 2066-2073.
123. Park SY, Park BK, Kim CK. The value of adding 18F-FDG PET/CT to adrenal protocol CT for characterizing adrenal metastasis (≥ 10 mm) in oncologic patients. *AJR* 2014; 202: W153-W160.
124. Yoo JY, McCoy KL, Carty SE, STang MT, Armstrong MJ, Howell GM, Bartlett DL, Tublin ME, Yip L. Adrenal imaging features predict malignancy better than tumor size. *Ann Surg Oncol* 2015; 22: S721-S727.
125. Lang BHH, Cowling BJ, Li JYY, Wong KP, Wan KY. High false positivity in positron emission tomography is a potential diagnostic pitfall in patients with suspected adrenal metastasis. *World J Surg* 2015; 39: 1902-1908.
126. Kim JY, Kim SH, Lee HJ, Kim MJ, Kim YH, Cho SH, Won KS. Utilisation of combined 18F-FDG PET/CT scan for differential diagnosis between benign and malignant adrenal enlargement. *Br J Radiol* 2013; 86: 20130190.
127. Yasaka K, Gono W, Akai H, Kasura M, Akahane M, Kiryu S, Ohtomo K. Differentiation of adrenal tumors in patients with hepatocellular carcinoma: adrenal adenoma versus metastasis. *Eur J Radiol* 2013; 82: 1213-1218.
128. Hijioka S, Sawaki A, Mizuno N, Hara K, Mekky MA, El-Amin H, Sayed ZEA, Tajika M, Niwa Y, Tamao K. Contrast-enhanced endoscopic ultrasonography (CE-EUS) findings in adrenal metastasis from renal cell carcinoma. *J Med Ultrasonics* 2011; 38: 89-92.
129. Sasaguri K, Takahashi N, Takeuchi M, Carter RE, Leibovich BC, Kawashima A. Differentiation of benign from metastatic adrenal masses in patients with renal cell carcinoma on contrast-enhanced CT. *AJR* 2016; 207: 1031-1038.
130. Mouka V, Tsili AC, Messinis T, Papoudou-Bai A, Kamina S, Argyropoulou MI. Solitary adrenal metastasis from early-stage dedifferentiated endometrial carcinoma: CT findings and review of the literature. *Journal of Obstetrics and Gynaecology* 2016; 36(7): 881-882.
131. Yun M, Kim W, Alnafisi N, Lacorte L, Jang S, Alavi A. 18F-FDG PET in characterizing adrenal lesions detected on CT or MRI. *J Nucl Med* 2001; 42: 1795-1800.
132. Refaat R, Elghazaly H. Employing 18F-FDG PET/CT for distinguishing benign from metastatic adrenal masses. *Egypt J Radiol Nucl Med* 2017; 48: 1065-1071.
133. Zhao H, Lin C, Jiao B, Sa R, Hou S, Xu S. Case report of 18F-fluorodeoxyglucose positron emission tomography-computed tomography imaging of a patient with multiple endocrine gland metastases from small cell lung cancer. *Thorac Cancer* 2018; 9: 167-170.
134. Cho AR, Lim I, Na II, Choe DH, Park JY, Kim BI, Cheon GJ, Choi CW, Lim SM. Evaluation of adrenal masses in lung cancer patients using F-18 FDG PET/CT. *Nucl Med Mol Imaging* 2011; 45: 52-58.
135. Kumar R, Xiu Y, Yu JQ, Takalkar A, El-Haddad G, Potenta S, Kung J, Zhuang H, Alavi A. 18F-FDG PET in evaluation of adrenal lesions in patients with lung cancer. *J Nucl Med* 2004; 45: 2058-2062.
136. Xie J, Dai J, Zhou WL, Sun FK. Adrenal ganglioneuroma: features and outcomes of 42 cases in a Chinese population. *World J Surg* 2018; 42: 2469-2475.
137. Lee JH, Chai YJ, Kim TH, Choi JY, Lee KE, Kim HY, Yoon YS, Kim HH. Clinicopathological features of ganglioneuroma originating from the adrenal glands. *World J Surg* 2016; 40: 2970-2975.
138. Iacobone M, Torresan F, Citton M, Schiavone D, Viel G, Favia G. Adrenal ganglioneuroma: the Padua endocrine surgery unit experience. *Int J Surg* 2017; 41: S103-S108.
139. Qing Y, Bin X, Jian W, Li G, Linhui W, Bing L, Huiqing W, Yinghao S. Adrenal ganglioneuromas: a 10-year experience in a Chinese population. *Surgery* 2010; 147: 854-860.
140. Johnson GL, Hruban RH, Marshall FF, Fishman EK. Primary adrenal ganglioneuroma: CT findings in four patients. *AJR* 1997; 169: 169-171.
141. Otal P, Mezghani S, Hassissene S, Maleux G, Colombier D, Rousseau H, Joffre F. Imaging of retroperitoneal ganglioneuroma. *Eur Radiol* 2001; 11: 940-945.
142. Shawa H, Elsayes KM, Morani A, Williams MD, Lee JE,

- Waguespack SG, Busaidy NL, Vassilopoulou-Sellin R, Jimenez C et al. Adrenal ganglioneuroma: features and outcomes of 27 cases at a referral cancer centre. *Clin Endocrinol* 2014; 80: 342–347.
143. Sasaki S, Yasuda T, Kaneto H, Otsuki M, Tabuchi Y, Fujita Y, Kubo F, Tsuji M, Fujisawa K, Kasami R et al. Large adrenal ganglioneuroma. *Intern Med* 2012; 51: 2365–2370.
144. Kamoun M, Mnif MF, Rekik N, Belguith N, Charfi N, Mnif L, Mouna Elleuch, Minf F Kamoun T, Mnif Z et al. Ganglioneuroma of adrenal gland in a patient with Turner syndrome. *Ann Diagn Pathol* 2010; 14: 133–136.
145. Majbar AM, Elmouhadi S, Elaloui M, Raiss M, Sabbah F, Hrrora A, Ahallat M. Imaging features of adrenal ganglioneuroma: a case report. *BMC Res Notes* 2014; 7: 791.
146. Adas M, Koc B, Adas G, Ozulker F, Aydin T. Ganglioneuroma presenting as an adrenal incidentaloma: a case report. *J Med Case Rep* 2014; 8: 131.
147. Scherer A, Niehues T, Engelbrecht V, Modder U. Imaging diagnosis of retroperitoneal ganglioneuroma in childhood. *Pediatr Radiol* 2001; 31: 106–110.
148. Zhang X, Li C, Xu C, Hao X, Yu X, Li Q. Correlation of CT signs with lymphatic metastasis and pathology of neuroblastoma in children. *Oncol Lett* 2018; 16: 2439–2443.
149. Decarolis B, Simon T, Krug B, Leuschner I, Vokuhl C, Kaatsch P, con Schweinitz D, Klingebiel T, Mueller I, Schweigerer L et al. Treatment and outcome of ganglioneuroma and ganglioneuroblastoma intermixed. *BMC Cancer* 2016; 16: 542.
150. He WG, Yan Y, Tang W, Cai R, Ren G. Clinical and biological features of neuroblastic tumors: a comparison of neuroblastoma and ganglioneuroblastoma. *Oncotarget* 2017; 8(23): 37730–37739.
151. Patterson AR, Barker CS, Loukota RA, Spencer J. Ganglioneuroma of the mandible resulting from metastasis of neuroblastoma. *Int J Oral Maxillofac Surg* 2009; 38: 196–198.
152. Aslan M, Alis D, Kalyoncu AU, Habibi HA, Ozdemir GN, Koc B, Adaletli I. Bilateral cystic adrenal neuroblastoma with cystic liver metastasis. *APSP J Case Rep* 2017; 8: 1.
153. Mehta SV, Lim-Dunham JE. Ultrasonographic appearance of pediatric abdominal neuroblastoma with inferior vena cava extension. *J Ultrasound Med* 2003; 22: 1091–1095.
154. Cassidy C, Winters WD. Bilateral cystic neuroblastoma: imaging features and differential diagnoses. *Pediatr Radiol* 1997; 27: 758–759.
155. Chen CP, Chen SH, Chuang CY, Lee HC, Hwu YM, Chang PY, Chen ML, Chen BF. Clinical and perinatal sonographic features of congenital adrenal cystic neuroblastoma: a case report with review of the literature. *Ultrasound Obstet Gynecol* 1997; 10: 68–73.
156. White SJ, Stuck KJ, Blane CE, Silver TM. Sonography of neuroblastoma. *AJR* 1963; 141: 465–468.
157. Boyd DT, Hayeri MR, Kadom N. Parotid metastasis from adrenal neuroblastoma. *Pediatr Radiol* 2010; 40: S113–S115.
158. Werner H, Daltro P, Davaus T, Junior EA. Fetal neuroblastoma: ultrasonography and magnetic resonance imaging findings in the prenatal and postnatal IV-S stage. *Obstet Gynecol Sci* 2016; 59(5): 407–410.
159. Cohen MD, Weetman R, Provisor A, McGuire W, McKenna S, Smith JA, Carr B, Siddiqui A, Mirkin D, Seo I et al. Magnetic resonance imaging of neuroblastoma with a 0.15-T magnet. *AJR* 1984; 143: 1241–1248.
160. Leung A, Shapiro B, Hattner R, Kim E, de Kraker J, Ghazzar N, Hartmann O, Hoefnagel CA, Jamadar DA, Kloos R. Specificity of radioiodinated MIBG for neural crest tumors in childhood. *J Nucl Med* 1997; 38: 1352–1357.
161. Gelfand MJ, Elgazzar AH, Kriss VM, Masters PR, Golsch GJ. Iodine-123-MIBG SPECT versus planar imaging in children with neural crest tumors. *J Nucl Med* 1994; 35: 1753–1758.
162. Biasotti S, Garaventa A, Villavecchia GP, Cabria M, Nantron M, De Bernardi B. False-negative metaiodobenzylguanidine scintigraphy at diagnosis of neuroblastoma. *Med Pediatr Oncol* 2000; 35: 153–155.
163. Melzer HI, Coppenrath E, Schmid I, Albert MH, von Schweinitz D, Tudball C, Bartenstein P, Pfluger T. 123I-MIBG scintigraphy/SPECT versus in paediatric neuroblastoma. *Eur J Nucl Med Mol Imaging* 2011; 38: 1648–1658.
164. Kroiss AS, Uprimny C, Shulkin BL, Gruber L, Frech A, Jazbec T, Girod PP, Url C, Thome C, Riechelmann H et al. 68Ga-DOTATOC PET/CT in the localization of metastatic extra-adrenal paraganglioma and pheochromocytoma compared with 18F-DOPA PET/CT. *Rev Esp Med Nucl Imagen Mol* 2019; doi: 10.1016/j.remnm.2018.09.004.
165. Pfluger T, Schmied C, Porn U, Leinsinger G, Vollmar C, Dresel S, Schmid I, Hahn K. Integrated imaging using MRI and 123I metaiodobenzylguanidine scintigraphy to improve sensitivity and specificity in the diagnosis of pediatric neuroblastoma. *AJR* 2003; 181: 1115–1124.
166. Zhuang B, Lv DK, Gao SJ, Meng JJ. Differential diagnosis of CT images in children with neuroblastomas and ganglioneuroblastomas. *Asian Pac J Cancer Prev* 2014; 15(23): 10509–10512.
167. Gahr N, Darge K, Hahn G, Kreher BW, Von Buiren M, Uhl M. Diffusion-weighted MRI for differentiation of neuroblastoma and ganglioneuroblastoma/ganglioneuroma. *Eur J Radiol* 2011; 79: 443–446.
168. Paling MR, Williamson BRJ. Adrenal involvement in non-Hodgkin lymphoma. *AJR* 1983; 141: 303–305.
169. Tanpitukpongse TP, Kamalian S, Punsoni M, Gupta M, Katz DS. Radiology-pathology conference: primary adrenal lymphoma. *J Clin Imaging* 2012; 35: 156–159.
170. Ezer A, Parlakgumus A, Kocer NE, Colakoglu T, Nursal GN, Yildirim S. Primary adrenal non-Hodgkin's lymphoma. *Turk J Gastroenterol* 2011; 22(6): 643–647.
171. Singh D, Kumar L, Sharma A, Vijayaraghavan M, Thulker S, Tandon N. Adrenal involvement in non-Hodgkin's lymphoma: four cases and review of literature. *Leukemia & Lymphoma* 2009; 45(4): 789–794.
172. Pagliuca A, Gillett DS, Salisbury JR, Basu RN, Mufti GJ. Bilateral adrenal lymphoma presenting as Addison's disease. *Postgrad Med J* 1989; 65: 684–686.
173. Cunningham JJ. Ultrasonic findings in "primary" lymphoma of the adrenal area. *J Ultrasound Med* 1983; 2: 467–469.
174. Li Y, Sun H, Gao S, Bai R. Primary bilateral adrenal lymphoma: 2 case reports. *J Comput Assist Tomogr* 2006; 30: 791–793.
175. Joseph FG, Cook S, Gowda D. Primary adrenal lymphoma with initial presentation concerning for bilateral adrenal pheochromocytomas. *BMJ Case Rep* 2017; doi:10.1136/bcr-2017-220549.
176. Aravamudan VM, Fong PK, Sam YS, Singh P, Ng SB, Kumar GSP. A rare case of primary bilateral adrenal lymphoma. *Case Rep Med* 2017; 2017: 1251950.
177. Apter S, Avigdor A, Gayer G, Portnoy O, Zissin R, Hertz M. Calcification in lymphoma occurring before therapy: CT features and clinical correlation. *AJR* 2002; 178: 935–938.
178. Zhou L, Peng W, Wang C, Liu X, Shen Y, Zhou K. Primary adrenal lymphoma: radiological, pathological, clinical correlation. *Eur J Radiol* 2012; 81: 401–405.
179. Ekhzaimy A, Mujamammi A. Bilateral primary adrenal lymphoma with adrenal insufficiency. *BMJ Case Rep* 2016. doi:10.1136/bcr-2016-217417.

180. Altaiar A, Aslan A, Gunduz N, Alimoglu O, Ayaz E. Unilateral primary adrenal B-cell lymphoma clinically mimicking chronic gastritis. *Pol J Radiol* 2017; 82: 612–615.
181. Ram N, Rashid O, Farooq S, Ulhaq I, Islam N. Primary adrenal non-Hodgkin lymphoma: a case report and review of the literature. *J Med Case Rep* 2017; 11: 108.
182. Erdogan G, Gullu S, Colak T, Kamel AN, Baskal N, Ekinci C. Non-Hodgkin's presenting as thyroid and adrenal gland involvement. *Endocr J* 1997; 44(1): 199–203.
183. Zhou J, Zhao Y, Gou Z. High 18F-fluorodeoxyglucose uptake in primary bilateral adrenal diffuse large B-cell lymphomas with nongerminal center B-cell phenotype. *Medicine* 2018; 97(17): e0480.
184. Nishiuchi T, Imachi H, Fujiwara M, Muaro K, Onishi H, Kiguchi T, Takimoto H, Kushida Y, Haba R, Ishida T. A case of non-Hodgkin's lymphoma primary arising in both adrenal glands associated with adrenal failure. *Endocr* 2009; 35: 34–37.
185. Martinez-Esteve A, Garcia-Gomez FJ, Madrigal-Toscano MD, Borrego-Dorado I. Primary bilateral diffuse large B-cell lymphoma of the adrenals. *Br J Haematol* 2015; 170(1): 3.
186. Forbes TL. Retroperitoneal hemorrhage secondary to a ruptured cavernous hemangioma. *J Can Chir* 2005; 48(1): 78.
187. Oh BR, Jeong YY, Ryu SB, Park YI, Kang HK. A case of adrenal cavernous hemangioma. *Int J Urol* 1997; 4: 608–610.
188. Marotti M, Susic Z, Krolo I, Dimanovski J, Klaric R, Ferencic Z, Karapanda N, Babic N, Pavlekovic K. Adrenal cavernous hemangioma: MRI, CT, and US appearance. *Eur Radiol* 1997; 7: 691–694.
189. Xu HX, Liu GJ. Huge cavernous hemangioma of the adrenal gland. *J Ultrasound Med* 2003; 22: 523–526.
190. Feo CV, De Troia A, Pedriali M, Sala S, Zatelli MC, Carcoforo P, Feo CF. Adrenal cavernous hemangioma: a case report. *BMC Surg* 2018; 18(1): 103.
191. Zemni I, Haddad S, Hlali A, Manai MH, Essoussi. Adrenal gland hemangioma: a rare case of the incidentaloma: case report. *Int J Surg Case Rep* 2017; 41: 417–422.
192. Agrusa A, Romano G, Salamone G, Orlando E, Di Buono G, Chianetta D, Sorce V, Gulotta L, Galia M, Gulotta G. Large cavernous hemangioma of the adrenal gland: laparoscopic treatment. Report of a case. *Int J Surg Case Rep* 2015; 16: 150–153.
193. Arkadopoulos N, Kyriazi M, Yiallourou AI, Stafyla VK, Theodosopoulos T, Dafnios N, Smyrniotis V, Kondi-Pafiti A. A rare coexistence of adrenal cavernous hemangioma with extramedullary hemopoietic tissue: a case report and brief review of the literature. *World J Surg Oncol* 2009; 7: 13.
194. Thiele JW, Bodie B. Adrenal hemangioma. *Surgery* 2001; 129: 373–374.
195. Telem TA, Nguyen SQ, Chin EH, Weber K, Divino CM. Laparoscopic resection of giant adrenal cavernous hemangioma. *JLS* 2009; 13: 260–262.
196. Heis HA, Bani-Hani KE, Bani-Hani BK. Adrenal cavernous haemangioma. *Singapore Med J* 2008; 49(9): e236–e237.
197. Quildrian SD, Silberman EA, Vigovich FA, Porto EA. Giant cavernous hemangioma of the adrenal gland. *Int J Surg Case Rep* 2013; 4: 219–221.
198. Matsuda D, Iwamura M, Baba S. Cavernous hemangioma of the adrenal gland. *Int J Urol* 2009; 16: 424.
199. Ellis CL, Banerjee P, Carney E, Sharma R, Netto GJ. Adrenal lymphangioma: clinicopathologic and immunohistochemical characteristics of a rare lesion. *Hum Pathol* 2011; 42: 1013–1018.
200. Lin TP, Chen M, Chen CK, Hsu JM, Lin WR. Adrenal cystic lymphangioma: a case report and review of the literature. *Urol Sci* 2014; 25: 112–114.
201. Liu B, Li Y, Wang S. Adrenal lymphangioma removed by a retroperitoneoscopic procedure. *Oncol Lett* 2013; 5: 539–540.
202. Secil M, Demir O, Yorukoglu K. MRI of adrenal lymphangioma: a case report. *Quant Imaging Med Surg* 2013; 3(6): 347–348.
203. Bibi M, Sellami A, Taktak T, Chelly B, Ghorbel Z, Zouari H, Boukriba S, Boussafa H, Chehida MAB, Rhouma SB et al. Giant cystic lymphangioma of adrenal gland: a case report and review of the literature. *Urol Case Reports* 2019; 22: 6–7.
204. Rowe SP, Bishop JA, Prescott JD, Salvatori R, Fishman EK. CT appearance of adrenal cystic lymphangioma: radiologic-pathologic correlation. *AJR* 2016; 206: 81–85.
205. Zhao M, Gu Q, Li C, Yu J, Qi H. Cystic lymphangioma of adrenal gland: a clinicopathological study of 3 cases and review of literature. *Int J Exp Pathol* 2014; 7(8): 5051–5056.
206. Zemheri E, Yildirim A, Ozkanli S, Zenginkinet T, Caskurlu T. Cystic lymphangioma of the adrenal gland: case report. *World J Nephrol* 2013; 2(2): 82–84.
207. Jung HI, Ahn T, Son MW, Kim Z, Bae SH, Lee MS, Kim CH, Cho HD. Adrenal lymphangioma masquerading as a pancreatic tail cyst. *World J Gastroenterol* 2014; 20(36): 13195–13199.
208. Cakir E, Aydin E, Samdanci E, Ates M, Elmali C, Sayin S, Erdem G. Cystic adrenal lymphangioma — report of two cases and review of the literature. *J Park Med Assoc* 2012; 62(9): 962–964.
209. Jakowski JD, Wakely Jr PE, Jimenez RE. An uncommon type of adrenal incidentaloma: a case report of a schwannoma of the adrenal medulla with cytological, histological, and ultrastructural correlation. *Ann Diagn Pathol* 2008; 12: 356–361.
210. Hsiao HL, Lin HC, Yeh HC, Huang CH, Wu WJ. Adrenal schwannoma treated with laparoscopic adrenalectomy: a case report. *Kaohsiung J Med Sci* 2008; 24: 553–557.
211. Suzuki K, Nakanishi A, Kurosaki Y, Nogaki J, Takaba E. Adrenal schwannoma: CT and MRI findings. *Radiat Med* 2007; 25: 299–302.
212. Xiao C, Xu B, Ye H, Yang Q, Wang L, Sun YH. Experience with adrenal schwannoma in a Chinese population of six patients. *J Endocrinol Invest* 2011; 34: 417–421.
213. Tarcoveanu E, Dimofte G, Bradea C, Moldovanu R, Vasilescu A, Anton R, Ferariu D. Adrenal schwannoma. *JLS* 2009; 13: 116–119.
214. Zhang YM, Lei PF, Chen MN, Lv XF, Ling YH, Cai PQ, Gao JM. CT findings of adrenal schwannoma. *Clin Radiol* 2016; 71: 464–470.
215. Liu QY, Gao M, Li HG, Lin XF, Huang SQ, Liang BL. Juxta-adrenal schwannoma: dynamic multi-slice CT and MRI findings. *Eur J Radiol* 2012; 81: 794–799.
216. Hou J, Zhang L, Guo Y, Chen H, Wang W. Primary adrenal schwannoma with catecholamine hypersecretion. *Arch Med Sci* 2016; 12(3): 681–683.
217. Tang W, Yu XR, Zhou LP, Gao HB, Wang QF, Peng WJ. Adrenal schwannoma: Ct, MR manifestations and pathological correlation. *Clin Hemorheol Microcirc* 2018; 68(4): 401–412.
218. Yang CY, Chou CW, Lin MB, Li CF. Schwannomas of the left adrenal gland and posterior mediastinum. *J Chin Med Assoc* 2009; 72(2): 83–87.
219. Onoda N, Ishikawa T, Toyokawa T, Takashima T, Wakasa K, Hirakawa K. Adrenal schwannoma treated with laparoscopic surgery. *JLS* 2008; 12: 420–425.
220. Kim SH, Choi BI, Han MC, Kim YI. Retroperitoneal neurilemoma: CT and MR findings. *AJR* 1992; 159: 1023–1026.
221. Korets R, Berkenblit R, Ghavamian R. Incidentally discovered adrenal schwannoma. *JLS* 2007; 11: 113–115.
222. Adas M, Ozulker F, Adas G, Koc B, Ozulker T, Sahin IM. A rare adrenal incidentaloma: adrenal schwannoma. *Case Rep Gastroenterol* 2013; 7: 420–427.

Improving patient CT scanning protocols in the setting of polytrauma

Gerta Repečkaitė¹, Kristina Banionienė¹, Eglė Kirklienė¹, Jurgita Zaveckienė¹.

¹Department of Radiology of Lithuanian University of Health Sciences Kaunas, Lithuania.

ABSTRACT

Background: Traumatic injuries are the fourth most common cause of death in all age/race/sex groups. Computed tomography (CT) is considered to be the current gold standard when providing a quick and accurate diagnosis of multiple injuries. However, a consensus regarding the study of chest - abdomen - pelvis (C-A-P) in polytrauma patients (PP) has not been reached.

Aim: To present an attempt at reducing the dose of ionizing radiation from CT in an emergency setting.

Materials and methods: We reviewed the hospital's medical records for PP who had undergone CT scans between 2011 and 2016. We evaluated CT phase sensitivity and contribution to the radiation dose and the associated oncogenic risk, as well as the workload of a radiologist.

Results: The most common traumatic findings were blood and/or hematoma within the abdominal cavity, lung contusion, pneumothorax, parenchymal organ injury, and rib fractures. The non-enhanced phase did not supply any additional information and was inferior to contrast-enhanced phases when diagnosing parenchymal organ injury and active hemorrhaging, meanwhile, it contributed to 19.7% of the workload and 29.5% of the radiation. The mean effective doses (ED) of C-A-P CT and whole body CT (WBCT) were 61.2 (\pm 27.7) mSv and 109.4 (\pm 30.5) mSv accordingly. PP received WBCT related mean ED was associated with cancer morbidity risk of 0.5% or 1/167.

Conclusion: Non-enhanced CT scans in PP contribute to wasted resources, increased radiation doses and higher future cancer risk, and supply no additional data when diagnosing traumatic findings.

Keywords: multiple trauma, radiation dosage, diagnostic imaging

1. INTRODUCTION

Traumatic injuries are the fourth most common cause of death in all age/race/sex groups, and the leading cause of death in children and young adults below 45 years of age (1). Although there are many defining parameters of polytrauma, the medical community generally describes it as injuries to multiple organs or regions of the body (2). The trauma to various systems compromises organs and systems that were not damaged during the initial trauma. Thus polytrauma patients (PP) are expected to be at a higher risk of mortality than the summation of expected mortality owing to each injury (3). A fast and accurate diagnosis is essential, but the diagnostic value of clinical evaluation is limited. Computed tomography (CT) imaging is widely utilized to establish medical diagnoses and perform image-guided interventions (4). Due to the advancements dur-

ing the past decade, CT has become a sensitive and precise tool when diagnosing injuries following polytrauma (5). CT has also proven to be fast and thus is considered to be the current gold standard when providing a diagnosis of multiple injuries (6). However, there is still room for improvement.

An adequate sensitivity for injury detection and cost-effectiveness without any unjustified radiation has been the primary focus of numerous attempts to develop optimized trauma imaging guidelines, such as the referral guidelines for imaging of the European Commission or the American College of Radiology appropriateness criteria (7,8). In the Lithuanian University of Health Sciences Hospital of Kaunas Clinics, Emergency Clinic patient's examination is based on standardized and widely accepted Advanced Trauma Life Support (ATLS). Exams of conventional radiology, for example, chest or pelvis X-ray, Fo-

cused Assessment with Sonography in Trauma (FAST) are have indication defined rather clearly by the aforementioned guidelines, while when it comes to CT, the decision of execution and the region of body to examine is left to the leader of the trauma team (9). While multiple CT scanning protocols for PP have been suggested by the medical community, a consensus regarding the study of the thorax, abdomen, and pelvis has not been reached (10–13). Specific authors consider the non-enhanced CT scans to be necessary when detecting the hyperdensity that suggests the presence of blood (14). The aforementioned scans help to identify small mesenteric, hepatic, splenic, renal hematomas, and the presence of the hemoperitoneum (14). More recently, concern has been raised regarding the risk of carcinogenesis from medical radiation, with a focus on CT (15,16).

With CT scan implementation in emergency medicine as a necessary diagnostic tool, decreased exposure to radiation has become the primary focus of protocol optimization. The literature describes that the average effective dose (ED) of a single-phase CT study is 22–32 mSv, and one single-body CT scan with a risk of death from ionizing radiation-induced cancer is approximately 0.08% (15,17).

Multiple studies have assessed the evaluation, frequency of injuries, and effectiveness of PP treatment in Lithuanian hospitals, however, to our knowledge, none had evaluated the imaging protocols or the radiation doses and correlating risks to the relatively young PP population. (18–23)

With these concerns in mind, this paper presents an attempt at reducing the dose of ionizing radiation from CT in an emergency setting.

2. METHODS AND MATERIALS

2.1. Study design and setting

In this retrospective study, medical health records and CT scan images of patients admitted to The Hospital of Lithuanian University of Health Sciences Kaunas clinic between 2011 and 2016 were analyzed. Kaunas Regional Biomedical Research Ethics Committee (KRBREC) approved the study protocol and waived informed consent.

2.2. PATIENT SELECTION CRITERIA AND DATA ACQUISITION

We reviewed the hospital's medical records for patients who had undergone chest - abdomen - pelvis (C-A-P) CT scans for suspected polytrauma between 2011 and 2016. The initial study population ($n = 103$) data were acquired by analyzing medical health records for demographic information, trauma mechanism and severity details, and CT scan images stored in Cedara-I-Reach (TM).

For the evaluation of CT scan phase significance, we selected patients ($n = 62$) who had undergone C-A-P three sequential CT scans. Pathologic CT scan findings were separated into dichotomous groups (present/not present) and evaluated in each phase. For this study, we documented the following chest CT scan findings: pneumothorax, haemothorax, pneumomediastinum, haemopericardium, mediastinal hematoma, lung contusion and laceration, active hemorrhaging into the parenchyma, pleural cavity or mediastinum, injury of the major vessels, traumatic diaphragm or oesophageal injury and bone fractures. Assessed abdominal organ CT scan findings were: fluid, hematoma, the air in the abdominal cavity, parenchymal organ injury with/without active hemorrhaging, and bone fractures. Results in non-enhanced/arterial/venous phases were compared.

To assess the radiation doses ($n = 94$) of C-A-P CT scans and separate phases, we used fixed technical parameters. ED was calculated using standardized dose-length product (DLP) parameters and conversion coefficient k ($k = 0.015$ mSv/mGy \times cm): ED (mSv) = DLP (mGy \times cm) $\times k$ (mSv/mGy \times cm). Additionally, we estimated the future risk for cancer among patients that had undergone whole-body CT scans ($n = 49$). To measure the workload of a radiologist, the CT scan image count for all phases was documented and compared between different phases.

Patients with insufficient medical record data, poor quality or incomplete CT scans were excluded from the study.

2.3. SCANNING PARAMETERS

In each case, CT scans were performed using one of the scanners: either GE VCT 64 or GE VCT

16 slice CT. Images were acquired by using PP scanning protocols: at a slice thickness of 5 mm; pitch 0.969:1; 120 kV, 100 - 665 mA, rotation speed 0.5 s, using an intravenous contrast agent, which was injected at the speed of 2.5 ml/s. All CT scan images were reviewed using the Picture Archiving and Communication System (PACS).

2.4. STATISTICAL ANALYSIS

We analyzed all data using IBM SPSS Statistics v. 23.0 and Microsoft Office Excel 2016. Normally distributed data were expressed as the mean value (\pm standard deviation) and non-normally distributed data as the median (minimum-maximum values). We used related-samples non-parametric Qochran's Q and McNemar tests to evaluate the significance of differences between different phase findings and group homogeneity using 2, one-way ANOVA and Kruskal-Wallis tests. Values of P less than 0.05 were considered significant.

3. RESULTS

The study population consisted of 82 (79%) male and 21 (21%) female participants with the mean age of 39.8 (\pm 15.8). (Table 1) 92.6% of traumas were blunt, and merely 7.4% were penetrating. The most common reasons for polytrauma in the study population were vehicle accidents (31.2%), and falling from a height of more than 3 meters (24.7%). Falling from a height of more or less than 3 meters and motorcycle accidents were responsible for accordingly 8.6% and 10.8% of traumas within the study sample. 63,5% (n = 54) patients were haemodynamically stable; however, 36,5% (n = 31) emergency CT scans were performed on patients with unstable haemodynamics.

The most prevalent traumatic findings in the CT scans were blood and/or hematoma within the abdominal cavity (11.8%), lung contusion

(11.2%), pneumothorax (9.5%), parenchymal organ injury (hepatic - 5.9%; splenic - 4%, renal and adrenal - 3% each) and rib fractures (9.5%). (Table 2)

Within the sample of PP that had undergone C-A-P three sequential CT scans (n = 62) statistically, significant inferiority was noted when diagnosing parenchymal organ injury with and without active hemorrhaging in non-enhanced CT scans compared to arterial or venous phases ($P < 0.05$). Otherwise, no statistically significant differences were noted. (Table 3) The non-enhanced phase did not supply any additional information, however, it was useful when diagnosing blood or air in the pleural cavity, pneumomediastinum, lung lacerations and/or contusions, gastrointestinal trauma. Active hemorrhaging was detected only in contrast-enhanced CT scans. The venous phase was superior, but not statistically significant when diagnosing blood in the peritoneum and parenchymal organ injury.

We calculated the number of images analyzed and concluded that by eliminating the arterial phase from PP scanning protocols we would decrease the amount of images by 32.6%, non-enhanced - by 19.7%, both - by 52.3%. Also, several patients' scanning protocols included the late venous phase, which attributed to an additional 197.0 (\pm 58) images. (Table 4)

The mean of the determined ED of radiation for patients that had undergone C-A-P CT scan was 61.2 (\pm 27.7) mSv, and 28.2% of the reported dose could be attributed to the radiation exposure during the arterial phase, 29.5% - to the non-enhanced scan and 32.9% to the venous phase. By forgoing the non-enhanced phase, the mean ED value of C-A-P CT scan becomes statistically significantly lower ($P < 0.001$). Patients, exposed to 109.4 (\pm 30.5) mSv (mean ED value of the whole body CT scan) had the cancer morbidity risk of 0.5% or 1/167.

Table 1. Demographic and injury severity data of the study population.

Count (n = 103)		Injury severity score (ISS)	Glasgow coma scale (GCS)	Hospitalisation length (days)
Male	Female			
82 (79%)	21 (21%)	30.17 (\pm 15.05)	12.72 (\pm 3.8)	19.10 (\pm 21.92)

Table 2. Trauma related CT scan finding frequency.

Traumatic findings	Number of cases	Percentage
Blood the abdominal cavity	56	11.8
Lung contusion	53	11.2
Pneumothorax	45	9.5
Rib fractures	45	9.5
Spinal column fractures	37	7.8
Haemothorax	35	7.4
Liver injury	28	5.9
Pelvic bone fractures	27	5.7
Spleen injury	19	4.0
Renal injury	14	3.0
Suprarenal gland injury	14	3.0
Lung laceration	14	3.0
Active haemorrhaging in the abdominal cavity	12	2.5
Pneumomediastinum	8	1.7
Haematoma of the mediastinum	5	1.1
Gastrointestinal organ injury	4	0.8
Pancreatic injury	2	0.4
Heart/pericardium injury	2	0.4
Injury of the major vessels in the thorax	2	0.4
Air in the abdominal cavity	1	0.2

Table 3. Non-parametric test results representing the statistical significance of non-enhanced/arterial/venous phase sensitivity differences when detecting trauma related CT scan findings.

Statistically significant differences	Statistically insignificant differences
<u>Parenchymal organ injury without active haemorrhaging:</u> Arterial and venous phases are superior to non-enhanced (McNemar test $P = 0.001$ and $P < 0.001$ accordingly)	Pleural effusion, ($P = 1.000$) Pneumothorax and/or pneumomediastinum ($P = 1.000$), Lung laceration and/ or contusion ($P = 1.000$), Gastrointestinal injury ($P = 1.000$);
<u>Parenchymal organ injury with active haemorrhaging:</u> Arterial and venous phases are superior to non-enhanced (McNemar test $P = 0.004$ in each case)	Active haemorrhaging into pleural cavity or mediastinum ($P = 0.368$); Fluid in the abdominal cavity ($P = 0.135$); Injury of the major abdominal vessels ($P = 0.368$)

Table 4. The contribution of each CT phase to the image count.

Chest - abdomen - pelvis CT scan image count	Minimum	Maximum	Mean (CI 95%)
In total	323	1151	631.88 \pm 160.4
Non-enhanced	54	247	120.5 \pm 27.5
Arterial phase	86	417	202.09 \pm 51.7
Venous phase	107	498	239.37 \pm 63.9
Late venous phase	82	417	197.0 \pm 58

4. DISCUSSION

In this study we observed that non-contrast-enhanced CT scan images are unnecessary when evaluating PP, seeing as they do not supply any additional information. Therefore, preceding the native phase improves the PP CT scanning protocols.

The most common CT scan findings observed in this study were blood and/or hematoma within the abdominal cavity (11.8%), lung contusion (11.2%), pneumothorax (9.5%), parenchymal organ injury (hepatic - 5.9%; splenic - 4%, renal and adrenal - 3% each) and rib fractures (9.5%). These findings are in correlation with the other studies. Parenchymal organ (especially spleen and liver) injury is observed most frequently (6). Lung parenchymal lesions, pleural effusions or pneumothorax, and rib fractures are the most common findings following chest trauma (24–26). Meanwhile, blunt injury to the blood vessels is not common (27). Quick detection of the aforementioned pathological findings ensures prompt diagnosis and treatment, which in turn decreases mortality and the waste of the resources.

However, with the widespread use of CT, ionizing radiation is becoming a significant concern, prompting research into dose reduction methods. The findings of this study indicate that one of the improvement possibilities is the elimination of non-enhanced CT scan images. We have observed that precontrast images provide no additional information in the setting of common polytrauma related findings, and are inferior to contrast-enhanced images. This is in accord with other studies that support the claim that precontrast CT scan image acquisition is superfluous and injury diagnosis in PP is not improved by the use of precontrast scans. Furthermore, both studies agree that unjustified CT scans contribute to an increased radiation dose (28,29). This consecutively suggests that the elimination of non-enhanced images from emergency trauma CT scanning protocols is justified by the reduction of radiation exposure without the loss of diagnostic accuracy.

Undoubtedly, multiple other optimization possibilities have been researched. A single acquisition

WBCT scan in the setting of polytrauma could cut down both time and resource consumption in addition to reducing ED without the impairment of diagnostic quality (13,30–32). Meanwhile, a revised triphasic injection single-pass WBCT scan protocol was superior to conventional PP scanning protocols using 64-multidetector CT (MDCT) (33). A split bolus technique suggested by Leung et al. offered a comparable quality with reduced radiation dose (34). Certain studies noted the necessity of dual-phase CT scans when detecting vascular lesions following trauma (35,36).

Meanwhile, Błaż et al. argued that the arterial phase is necessary only for the thorax scans, seeing as clinically significant hemorrhaging of the abdominal arteries would be visible in the venous phase (37). In our study, we found a non-significant superiority of the venous phase when diagnosing blood in the peritoneum and parenchymal organ injury. All in all, numerous CT scanning protocol improvement possibilities today make the unjustifiable radiation dose and thus carcinogenic risk to be even more illogical, entailing an obligation to reach a consensus.

Although the radiation dose received by PP varies greatly, we found the CT related dose to range from 55.81 to 183.96 mSv with the mean value being 109.4 (\pm 30.5) mSv. These numbers are alarming, seeing as current data support, albeit inconclusively, the notion that doses from 5 mSv significantly increase the oncogenic risk (38–41), while radiation doses above 100 mSv are acknowledged by the medical community to attribute to additional cancer instances (42). CT scans deliver concerning amounts of radiation and may contribute to 29 000 new cancers each year, along with 14 500 deaths (43). To avoid unnecessary risks, exposure to radiation must be As Low As Reasonably Achievable (ALARA) (44). Bearing in mind that patients undergo additional follow-up CT scans, many PP exceeds the 100 mSv and consequently are at a higher risk of developing cancer.

Another important observation of this study was that women and children make up 21% of our study population and the mean age was 39.8 (\pm 15.8). Multiple factors determine the cancer development risk following radiation exposure:

genetics, age during exposure, sex of the subject, radiation exposure rates, etc. (38). This is important to take into consideration when preparing diagnostic protocols for PP, seeing as the majority of traumatic injuries occur to people younger than 45 years of age, including females and children, who are at a higher risk of developing oncologic diseases (1,38). According to our findings, the majority of the relatively young PP population is at a higher risk of developing oncologic diseases.

Furthermore, we found that the mean amount of CT scan images that a radiologist had to evaluate was 631.88 (± 160.4), with the highest count reaching 1151 images per case. A high count of images requiring evaluation increases the probability of missed injuries and prolongs the time to treatment (45,46). The required time for trauma-related imaging differs depending on scanning protocols. However, WBCT requires approximately 12 min, while non-WBCT requires 75 min on average to scan (47). Taking this time into consideration and factoring in the time to evaluate all the images, time to diagnosis is prolonged. In turn, transfers and/or injury management may be delayed, which negatively affects survival (48–50). Moreover, the additional workload wastes resources increases mortality and morbidity not only due to delayed treatment but also due to misdiagnosis originating from overworked radiologists (46). Therefore, optimization is beneficial both to the patient and the medical community.

It is important to note that this study had some limitations. First of all, the study population was rather small, due to the fact only PP who had undergone three phase C-A-P CT scans were included. This could attribute to decreased reliability of our findings, seeing as other PP may have been excluded. Nonetheless, our results were in agreement with the other studies (28,29). Secondly, the ED calculation was based on a standardized formula that does not take into account the weight, height and other variable parameters of the subject. This method of ED estimation, however, is utilized by other studies (28,29,51). Finally, the evaluation of CT scan findings as either present or not could have had an impact on our conclusions, seeing as the severity of an in-

jury is also an essential factor when visualization sensitivity and specificity are being evaluated.

In conclusion, non-enhanced C-A-P CT scans in PP contribute to wasted resources, increased radiation doses and oncogenic risks, and supply no additional information when diagnosing traumatic findings. Therefore, optimization of PP scanning protocols by non-enhanced phase exclusion is justified and beneficial.

REFERENCES

- Heron M. Leading Causes for 2014. *Natl Vital Stat Reports* 2016; **65**:1–95.
- Rau CS, Wu SC, Kuo PJ et al. Polytrauma defined by the new berlin definition: A validation test based on propensity-score matching approach. *Int J Environ Res Public Health* 2017; **14**:1045.
- Butcher N, Balogh ZJ. The definition of polytrauma: the need for international consensus. *Injury* 2009; **40**:12–22.
- Linsenmaier U, Rock C, Krötz M et al. Whole-body computed tomography in polytrauma : techniques and management. *Eur Radiol* 2002; **12**:1728–1740.
- Eurin M, Haddad N, Zappa M et al. Incidence and predictors of missed injuries in trauma patients in the initial hot report of whole-body CT scan. *Injury* 2012; **43**:73–77.
- Soto JA, Anderson SW. Multidetector CT of Blunt Abdominal Trauma. *Radiology* 2012; **265**:678–693.
- EUR 16262EN. European Comission: European guidelines on quality criteria for computed tomography - EU Law and Publications. Luxembourg: EUR 2000<https://publications.europa.eu/en/publication-detail/-/publication/d229c9e1-a967-49de-b169-59ee68605f1a> (accessed 1 Dec2018).
- Nagel HD, Huda W. Radiation Exposure in Computed Tomography. *Med Phys* 2002; **29**:1922–1922.
- Brasel KJ. Advanced trauma life support (ATLS??): The ninth edition. *J Trauma Acute Care Surg* 2013; **74**:1363–1366.
- Salim A, Sangthong B, Martin M et al. Whole Body Imaging in Blunt Multisystem Trauma Patients Without Obvious Signs of Injury. *Arch Surg* 2006; **141**:468.
- Holmes JF, McGahan JP, Wisner DH. Rate of intra-abdominal injury after a normal abdominal computed tomographic scan in adults with blunt trauma. *Am J Emerg Med* 2012; **30**:574–579.
- Holly BP, Steenburg SD. Multidetector CT of blunt traumatic venous injuries in the chest, abdomen, and pelvis. *RadioGraphics* 2011; **31**:1415–1424.
- Nguyen D, Platon A, Shanmuganathan K et al. Evaluation of a single-pass continuous whole-body 16-MDCT protocol for patients with polytrauma. *Am J Roentgenol* 2009; **192**:3–10.
- Kelly J, Raptopoulos V, Davidoff A et al. The value of non-contrast-enhanced CT in blunt abdominal trauma. *AJR Am J Roentgenol* 1989; **152**:41–48.
- Hendee WR, O'Connor MK. Radiation Risks of Medical Imaging: Separating Fact from Fantasy. *Radiology* 2012; **264**:312–321.
- Costello JE, Cecava ND, Tucker JE et al. CT radiation dose: Current controversies and dose reduction strategies. *AJR Am J Roentgenol* 2013; **201**:1283–1290.
- Sierink JC, Saltzherr TP, Wirtz MR et al. Radiation exposure before and after the introduction of a dedicated total-body CT protocol in multitrauma patients. *Emerg Radiol* 2013; **20**:507–512.
- Pamerneckas A, Adukauskienė D, Macas A. [Multiple trauma: evaluation of patient's condition and local injuries by trauma classification systems]. *Med* 2002; **38**:685–694.
- Pamerneckas A, Macas A, Vaitkaitis D et al. Golden hour - early postinjury period. *Med* 2003; **39**:845–851.
- Pamerneckas A, Pijadin A, Pilipavičius G et al. The assessment of clinical evaluation and treatment results of high-energy blunt polytrauma patients. *Med* 2007; **43**:137–144.
- Pamerneckas A, Petrulis A, Pilipavičius G et al. Influences on Mortality of Polytrauma Patients. *Osteosynthesis Trauma Care* 2006; **14**:98–100.
- Pamerneckas A, Macas A, Blazgys A et al. The treatment of multiple injuries: prehospital emergency aid. *Med* 2006; **42**:395–400.
- Gaidamonis E, Stanaitis J. Blužnės sužalojimai dėl uždaros pilvo traumos. *Lith Surg* 2007; **9942**:152–160.
- Rodriguez RM, Friedman B, Langdorf MI et al. Pulmonary contusion in the pan-scan era. *Injury* 2016; **47**:1031–1034.
- Di Bartolomeo S, Sanson G, Nardi G et al. A population-based study on pneumothorax in severely traumatized patients. *J Trauma* 2001; **51**:677–682.
- Mirvis SE. Imaging of Acute Thoracic Injury: The Advent of MDCT Screening. *Semin Ultrasound, CT MRI* 2005; **26**:305–331.
- Muckart DJJ, Pillay B, Hardcastle TC et al. Vascular injuries following blunt polytrauma. *Eur J Trauma Emerg Surg* 2014; **40**:315–322.
- Naulet P, Wassel J, Gervaise A et al. Evaluation of the value of abdominopelvic acquisition without contrast injection when performing a whole body CT scan in a patient who may have multiple trauma. *Diagn Interv Imaging* 2013; **94**:410–417.
- Esposito AA, Zilocchi M, Fasani P et al. The value of pre-contrast thoraco-abdominopelvic CT in polytrauma patients. *Eur J Radiol* 2015; **84**:1212–1218.
- Sedlic A, Chingko CM, Tso DK et al. Rapid imaging protocol in trauma : a whole-body dual-source CT scan. *Emerg Radiol* 2013; **20**:401–408.
- Eichler K, Marzi I, Wyen H et al. Multidetector computed tomography (MDCT): Simple CT protocol for trauma patient. *Clin Imaging* 2015; **39**:110–115.
- Hakim W, Kamanahalli R, Dick E et al. Trauma whole-body MDCT: An assessment of image quality in conventional dual-phase and modified biphasic injection. *Br J Radiol* 2016; **89**.
- Yaniv G, Portnoy O, Simon D et al. Revised protocol for whole-body CT for multi-trauma patients applying triphasic injection followed by a single-pass scan on a 64-MDCT. *Clin Radiol* 2013; **68**:668–675.
- Leung V, Sastry A, Woo TD et al. Implementation of a split-bolus single-pass CT protocol at a UK major trauma centre to reduce excess radiation dose in trauma pan-CT. *Clin Radiol* 2015; **70**:1110–1115.
- Hamilton JD, Kumaravel M, Censullo ML et al. Multidetector CT Evaluation of Active Extravasation in Blunt Abdominal and Pelvic Trauma Patients. *RadioGraphics* 2008; **28**:1603–1616.
- Iacobellis F, Ierardi AM, Mazzei MA et al. Dual-phase CT for the assessment of acute vascular injuries in high-energy blunt trauma: the imaging findings and management implications. *Br J Radiol* 2016; **89**:20150952.
- Błaż M, Palczewski P, Gołębiowski M et al. Optimization of CT protocol for imaging of polytraumatized patients. 2010; **16**:48–51.
- Hricak H, Brenner DJ, Adelstein SJ et al. Managing Radiation Use in Medical Imaging: A Multifaceted Challenge. *Radiology* 2010; **258**:889–905.
- Mayo-Smith WW, Hara AK, Mahesh M et al. How I Do It: Managing Radiation Dose in CT. *Radiology* 2014; **273**:657–672.

40. Huda W. Radiation Risks: What Is to Be Done? 2015: **204**:124–127.
41. Duncan JR, Lieber MR, Adachi N et al. Radiation Dose Does Matter: Mechanistic Insights into DNA Damage and Repair Support the Linear No-Threshold Model of Low-Dose Radiation Health Risks. *J Nucl Med* 2018; **59**:1014–1016.
42. Picano E, Vano E, Rehani MM et al. The appropriate and justified use of medical radiation in cardiovascular imaging: A position document of the ESC Associations of Cardiovascular Imaging, Percutaneous Cardiovascular Interventions and Electrophysiology. *Eur Heart J* 2014; **35**:665–672.
43. Berrington de González A, Mahesh M, Kim K-P et al. Projected Cancer Risks From Computed Tomographic Scans Performed in the United States in 2007. *Arch Intern Med* 2009; **169**:2071.
44. ICRP. ICRP Publication 105. Radiation protection in medicine. *Ann ICRP* 2007; **37**:3–5.
45. Rieger M, Czermak B, El Attal R et al. Initial Clinical Experience With a 64-MDCT Whole-Body Scanner in an Emergency Department: Better Time Management and Diagnostic Quality? *J Trauma Inj Infect Crit Care* 2009; **66**:648–657.
46. Dreizin D, Munera F. Blunt Polytrauma: Evaluation with 64-Section Whole-Body CT Angiography. *RadioGraphics* 2012; **32**:609–631.
47. Gordic S, Alkadhi H, Hodel S et al. Whole-body CT-based imaging algorithm for multiple trauma patients: radiation dose and time to diagnosis. *Br J Radiol* 2015; **88**:20140616.
48. Barbosa RR, Rowell SE, Fox EE et al. Increasing time to operation is associated with decreased survival in patients with a positive FAST examination requiring emergent laparotomy. *J Trauma Acute Care Surg* 2013; **75**:S48–S52.
49. Johns TJ. Characteristics and risk factors of trauma patients readmitted to the ICU within the same hospitalization. *J Trauma Nurs* 2014; **21**:14–21.
50. Gonzalez-Robledo J, Martin-Gonzalez F, Moreno-Garcia M., Sanchez-Barba M. S-HF. Prognostic factors associated with mortality in patients with severe trauma: From prehospital care to the Intensive Care Unit. *Med Intensiva* 2015; **39**:412–421.
51. Huda W, Ogden KM, Khorasani MR. Converting Dose-Length Product to Effective Dose at CT. *Radiology* 2008; **248**:995–1003.

Neuroimaging of headaches attributed to cranial and/or cervical vascular disorders

Gerta Repeckaite¹, Agne Smigelskyte¹, Rymante Gleizniene²

¹Lithuanian University of Health Sciences, Academy of Medicine, Faculty of Medicine, Kaunas, Lithuania

²Lithuanian University of Health Sciences, Academy of Medicine, Faculty of Medicine, Clinic of Radiology, Kaunas, Lithuania

ABSTRACT

Secondary headaches comprise approximately 10% of all headache cases. They often have a serious underlying condition that needs prompt and thorough examination, which almost always includes neuroimaging. Each imaging modality serves a different purpose, and various diagnostic methods can be utilized in the diagnostics of headaches attributed to cranial and cerebral vascular disorders which vary in both etiology and manifestation. This literature review aims to summarise and present the role of neuroimaging in the evaluation of patients with the conditions above.

Keywords: neuroimaging; headache disorders, secondary; radiology

INTRODUCTION

Headache is a recurrent or persistent pain of the head (1). It has a lifelong prevalence of 66-96% and the current prevalence of 46% (1, 2) and is a common presenting complaint in the emergency department, responsible for approximately 2% of all visits (3). Headaches are divided into primary (with no underlying cause) and secondary (caused by another condition) (4). Primary headaches are more common – they comprise 90% of all cases (5). Although rare, secondary headaches are often life-threatening and require immediate action (6). However, diagnosis more often than not requires imaging evaluation of the head. This article aims to present different aspects of secondary headaches attributed to cranial or cervical vascular disorders with a particular focus on neuroimaging of the underlying condition.

REVIEW OF LITERATURE

Headache attributed to a cerebral ischemic event Ischemic stroke is an episode of neurological dysfunction which lasts more than 24 hours and is caused by focal cerebral, spinal or retinal infarction (7). It is a common neurological disorder with an incidence ranging from 95 to 290 per 100 000 inhabitants in Europe (8). Observational studies indicate that 8%–64% of patients report a

headache at the onset of an acute ischemic stroke (9). Generally, the stroke associated headache is not severe but continuous and manifests as bilateral tension-type head pain. (10). Basilar strokes are associated with headaches more often than carotid strokes while lacunar strokes are generally not accompanied by headaches at all (9). A small number of migraine patients infrequently suffer from migrainous strokes with an incidence of 0,8 per 100 000 inhabitants (11).

Headache at stroke onset is predictive of a headache development at six months post-stroke (12). Persistent headaches attributed to past ischemic events have been estimated to occur in 10% of post-stroke patients. A post-stroke headache is predominantly characterized as a tension-type headache with a pressing quality (13).

In the setting of an acute stroke, neuroimaging is performed to exclude possible hemorrhages, to assess the degree of brain injury, and to identify the vascular lesion responsible for the ischemic deficit (14).

Non-contrast computed tomography (CT) scans are the first modality of choice in case of acute ischemic stroke because of their wide availability and rapidity of imaging (15). Non-contrast CT scans are useful in detecting large ischemic strokes after 6 to 8 hours from onset. Non-contrast CT has an overall sensitivity of 57-71% to detect an acute ischemic stroke in the first 24

hours but only 12% in the first 3 hours (16, 17). Early non-contrast CT findings include hypoattenuation in the territory of the middle cerebral artery, hypodensity of the lentiform nucleus, cortical sulcal effacement, focal parenchymal hypoattenuation, loss of the insular ribbon or obscuration of the Sylvian fissure, hyperattenuation of large vessels, loss of gray and white matter differentiation in the basal ganglia (14).

Alberta Stroke Program Early CT Score (ASPECTS) method assists in evaluating early ischemic changes in CT scans. ASPECTS is a scoring system of 10 points and can be applied only to the territory of the middle cerebral artery (18, 19).

CT angiography (CTA) provides the means to rapidly and noninvasively evaluate the intracranial and extracranial vasculature in stroke patients, thus providing valuable information about the presence of vessel occlusion or stenosis (20). CTA has a sensitivity of 92-100% and specificity of 82-100% for the detection of intracranial large vessel occlusion and stenosis (21). A noninvasive intracranial vascular study is a must before endovascular therapy (15, 20).

Magnetic Resonance Imaging (MRI) is superior to CT in detecting hyperacute stroke (14). Fluid attenuation inversion recovery (FLAIR) and T2 weighted (T2W) sequences become positive within the first 3 to 8 hours after an acute arterial occlusion. The MRI signs of acute ischemic stroke include increased brain signal intensity, swollen cortical gyri, and increased signal intensity in the lumen of vessels (16). Diffusion-weighted imaging (DWI) is a form of MRI that is capable of detecting brain tissue damage during the first 3 to 30 minutes of ischemia, making it the most sensitive early neuroimaging technique in the setting of an acute ischemic stroke (Figure 1) (23).

A transient ischemic attack is a temporary episode (less than 24 hours in duration) of neurological dysfunction caused by focal brain, spinal, or retinal ischemia without any evidence of acute infarction (7). Headache is rarely a prominent symptom of a transient ischemic attack – its frequency varies between 16 and 36% (24). In the case of transient ischemic attack, head CT or MRI must be performed to exclude infarction.

DWI can be used to distinguishing brain, spinal, or retinal ischemia from an acute infarction (25).

HEADACHE ATTRIBUTED TO NON-TRAUMATIC INTRACRANIAL HEMORRHAGE

Headache attributed to non-traumatic intracerebral hemorrhage (ICH)

Intracerebral hemorrhage (ICH) is defined as haemorrhage into the brain parenchyma and occurs with the incidence of approximately 25 cases for every 100 000 inhabitants annually (26). Non-traumatic or spontaneous ICH is caused by a variety of aetiologies, the most common reasons being hypertensive or amyloid angiopathy (27). Headache is one of the most prevalent symptoms of ICH (28). The manifestation of the headache does not depend on the cause and is usually gradual (29); however, it may also manifest as a thunderclap headache (30). Other common symptoms include nausea, vomiting, focal neurological deficit symptoms, deteriorating consciousness, etc. (31).

Since clinical presentation is not sufficient for the differentiation between ischemic and hemorrhagic focal neurological symptom origins, imaging modalities are imperative. The gold standard for acute hemorrhage detection is non-contrast CT or gradient recalled echo (GE) and T2*-susceptibility-weighted MRI (31, 32). CT scan findings assist with clinical decisions by evaluating hematoma volume and predicting the upcoming 30-day mortality (34). Contrast-enhanced CT and CTA may be useful in assessing the risk of hematoma expansion by detecting focal areas of contrast within the hematoma (known as the spot sign) (35–37) or a large number of cerebral microbleeds (38).

In the setting of ICH, CT is inferior to other imaging modalities, such as MRI and angiography, especially sometime after the onset. Nonetheless, as mentioned previously in this review, in emergency diagnostics, CT is the preferred imaging modality for its availability, cost-effectiveness, and rapidity. CT angiography/venography (CTA/CTV), and contrast-enhanced MRI or MR angiography/venography (MRA/MRV) are informative when there is suspicion of an underlying structural lesion (39). Detected hyperin-

tense lesions in DWI indicate acute or subacute ICH (Figure 2) (40). MRI and MRA are far more sensitive when diagnosing older hemorrhages, secondary (primarily structural) causes, such as arteriovenous malformations, tumors, and cerebral venous thrombosis (27, 31, 32, 40).

Headache attributed to non-traumatic subarachnoid hemorrhage (SAH)

1% of all emergency room visitors suffering from headaches are diagnosed with subarachnoid hemorrhage (SAH) (3). SAH is defined as hemorrhaging into the cerebrospinal fluid (CSF) due to corticomeningeal vessel rupture and occurs in approximately 8 out of 100 000 people per year (42). Multiple underlying conditions may be responsible for the development of SAH: various vascular disorders, traumas, blood dyscrasias, etc. (43) Common SAH manifestations include a sudden severe thunderclap headache which can be the only manifestation of the condition (43, 44). Additional symptoms involve changes in consciousness, neurological deficits, seizures, vomiting, and neck stiffness (46). Due to its high prevalence, neuroimaging in the setting of SAH is a widely researched topic. However, currently, there is a significant disparity in opinions concerning the diagnostic protocols (47).

The most common clinical practice is to perform a non-contrast CT scan, followed by lumbar puncture (LP) if the head CT scan is non-diagnostic (48). This protocol is still considered to have the highest sensitivity, while MRI/MRA and CT/CTA are alternative imaging modality protocols, useful in cases where CT/LP is contraindicated or hazardous (49). Furthermore, CT has lower sensitivity when diagnosing SAH in the posterior fossa, in patients without focal neurological abnormalities, and cases of small hemorrhaging volumes (50). Current data suggest that MRI FLAIR sequence is more sensitive than or equal to CT when detecting acute or subacute SAH (42, 50–52) and additional scanning protocols may be useful when diagnosing an underlying condition (54). Nonetheless, negative MRI would still require a follow-up LP (55).

LP is an invasive procedure, which prompts an effort to find a similar or even more sensitive diagnostic tool. It has been hypothesized that CTA could replace LP in the SAH diagnostics

as a non-invasive and thus safer procedure with relatively high sensitivity (42). However, data from the recent studies suggest that it would not be an optimal approach seeing as asymptomatic aneurysms could be unnecessarily diagnosed and the imaging modality comes with unwarranted radiation exposure as well as considerable expenses (41, 55, 56). On the other hand, modern third-generation cranial CT scans performed within the first 6 hours of headache onset and evaluated by a qualified radiologist have incredibly high specificity and sensitivity (100% each), which warrants the elimination of a follow-up tool altogether (58–60). This suggests that improved CT scanning protocols negate LP necessity and dangers, which occur due to having a higher probability of complications than of diagnosis (61–63). However, the 6-hour CT diagnostic sensitivity applies only to the patients that have no focal neurological abnormalities or changes in consciousness (64) and CT sensitivity drops to 50% at seven days. Meanwhile, LP is diagnostic from 12 hours post-ictus and up to two weeks after the onset (65).

Once a diagnosis has been established, further imaging modalities are required to determine the cause.

HEADACHE ATTRIBUTED TO NON-TRAUMATIC ACUTE SUBDURAL HEMORRHAGE (ASDH)

Acute subdural hemorrhage (ASDH) is defined as acute bleeding between the dura and arachnoid membranes usually due to damage to the bridging veins (66). Spontaneous ASDH is less common than traumatic subdural hemorrhages, however, it is more dangerous due to higher mortality (67). Non-traumatic ASDH may be caused by multiple conditions, such as impaired hemostasis, cerebral aneurysms, ruptured cortical artery, arteriovenous malformations, neoplasms, hypertensive cerebral hemorrhage, intracranial hypotension, Cerebral Amyloid Angiopathy (CAA), and acquired immune deficiency syndrome (68). The headache manifests suddenly in accordance with the site of hemorrhaging and peaks in seconds or minutes, typically just before the focal neurological symptoms (30).

Non-contrast CT is integral in both initial clinical decision making and as a follow up (67). The

main feature of ASDH as seen on a CT scan is usually a hyperdense and sometimes mixed appearance of the subdural space (69). MRI is more sensitive when diagnosing extremely thin, hemispheric or tentorial subdural hemorrhages (70). Imaging parameters, evaluated in the setting of ASDH are age or thickness of the hemorrhage, midline shift, presence of blood in the basal cisterns, ventricle obstruction. Additionally, underlying conditions may be visualized using CT, MRI, CTA, MRA and other imaging modalities (66). For example, vascular imaging of the head is advisable in patients with spontaneous ASDH without coagulopathy, due to the possibility of a ruptured cranial aneurysm (71–76).

Persistent headache following non-traumatic ICH, SAH, ASDH

Headaches that persist more than three months after a non-traumatic intracranial hemorrhage have no specific imaging characteristics and thus are not described in this review.

HEADACHE ATTRIBUTED TO UNRUPTURED VASCULAR MALFORMATION

HEADACHE ATTRIBUTED TO UNRUPTURED SACULAR ANEURYSM

An unruptured intracranial saccular aneurysm is a protrusion from a cerebral artery that consists of a damaged or absent tunica media and an internal elastic lamina (77). It occurs in 1–2% of the population (78). Sometimes unruptured intracranial aneurysms manifest as a thunderclap headache, loss of visual acuity or palsy of the 3rd cranial nerve but usually, they are asymptomatic (64, 77). Therefore, an unruptured aneurysm is often an incidental radiological finding. Aneurysms of 3 mm or larger can be identified on CT (79), but CTA is frequently required to clarify the diagnosis. CTA has specificity rates of 96–98% (90–94% for aneurysms smaller than 3 mm and up to 100% for aneurysms larger than 4 mm) and sensitivity rates of 96–98% for the detection of an intracranial unruptured saccular aneurysm (79, 80). The majority of saccular aneurysms are found around the anterior and posterior communicating arteries, the bifurcation of the middle cerebral artery, the internal carotid artery, the basilar artery, the superior cerebellar

artery and the posterior inferior cerebellar artery (64, 76). Just like CT, MRI has a somewhat limited role in detecting an unruptured saccular aneurysm. However, three-dimensional time-of-flight MRA with volume rendering at 3.0 Tesla has a sensitivity of 99% and specificity of 97% which is irrespective of aneurysm size (81, 82). Digital subtraction angiography is indicated in the case of negative CTA/MRA or before surgical or endovascular treatment to evaluate adjacent structures and blood flow patterns (Figure 3) (84).

HEADACHE ATTRIBUTED TO ARTERIOVENOUS MALFORMATION

Arteriovenous malformation (AVM) is a congenital disorder of the brain or spinal cord characterized by an abnormal tangle of arteries and veins with varying amounts of fistulas (85). Brain AVMs have a prevalence of 18 per 100 000 inhabitants (86). Presenting symptoms of AVM are intracranial bleeding, headache, seizures, and focal neurological deficits (85). Signs of AVM on non-contrast CT include a usually hyperdense nidus with enlarged draining veins in the periphery of the brain parenchyma. CTA may improve the sensitivity of CT to identify brain AVMs. (87). Signs of AVM on MRI include the nidus, feeding arteries, and draining veins that demonstrate flow void and can be seen on conventional sequences (65), while MRA may help confirm the more subtle AVMs (Figure 4) (88). The diagnosis of AVM is confirmed by cerebral angiography (87).

HEADACHE ATTRIBUTED TO DURAL ARTERIOVENOUS FISTULA

Dural arteriovenous fistula (DAVF) is an abnormal connection between meningeal arteries and dural venous sinuses or subarachnoid veins (89). It has a detection rate of 0.16–0.29 per 100 000 inhabitants each year (90). DAVF frequently presents as painful pulsatile tinnitus or a headache with other symptoms of intracranial hypertension (91). A diagnostic evaluation usually starts with head non-contrast CT or MRI (92). CTA and MRA characterize the feeding arteries, early dural sinus opacification, and prominent draining veins (89). The diagnosis is confirmed with digital subtraction angiography which remains

the gold standard in the case of DAVFs (64, 93). Headache attributed to cavernous angioma Cavernous angioma occurs in 0.4 – 0.8% of the population and is described as a vascular malformation of the brain and spinal cord characterized by a lack of tight junctions between the lining endothelial cells of pathologically dilated blood vessels and slow blood flow within the pathological structure (94). Some cavernous angiomas may trigger cluster headache-like, SUNCT-like (short-lasting unilateral neuralgiform headache with conjunctival injection and tearing) or migraine-like attacks. The location of the headache typically coincides with the site of the cavernous angioma (30). The primary imaging modality for cavernous angiomas is MRI. The most common finding is a reticulated lesion with mixed signal intensities (Figure 5) (95).

HEADACHE ATTRIBUTED TO ENCEPHALOTRIGEMINAL OR LEPTOMENINGEAL ANGIOMATOSIS (STURGE-WEBER SYNDROME)

Encephalotrigeminal or leptomeningeal angiomas (Sturge-Weber syndrome) is a congenital vascular disorder characterized by a capillary or capillary-venous malformation of the face, brain, and eye (96). It occurs in approximately 1 in every 20 000 – 50 000 newborns (97). Encephalotrigeminal or leptomeningeal angiomas may cause migraine attacks with long motor auras (30). Other symptoms include port wine stain on the face, seizures, hemiparesis, visual disorders, behavioral problems, and mental retardation (98). The primary neuroimaging technique for the diagnosis of this disorder is brain MRI with gadolinium contrast (96). Pia and cortical enhancement are usual signs of Sturge-Weber syndrome on MRI (99). CT is less useful but may detect brain calcification and atrophy (98). Angiography can reveal the lack of superficial cortical veins and tortuous veins near the vein of Galen (98). Positron Emission Tomography (PET) or Single Photon Emission Computed Tomography (SPECT) are rarely used in diagnosing Sturge-Weber syndrome, but abnormal glucose metabolism and cerebral perfusion may be detected before the presence of clinical symptoms (Figure 6) (98).

HEADACHE ATTRIBUTED TO ARTERITIS

The current gold standard for diagnosing various forms of arteritis is a vessel biopsy. However, neuroimaging plays a major role in screening and with increasing improvements may rival the sensitivity and specificity even of the aforementioned invasive procedure.

HEADACHE ATTRIBUTED TO GIANT CELL ARTERITIS

Giant cell arteritis (GCA) is a granulomatous vasculitis of medium and large arteries (100). This idiopathic and chronic condition occurs in people older than 50 years with an incidence ranging from 6,9 to 32,4 per 100 000 inhabitants (101). Headache is a presenting symptom in two-thirds of GCA patients, but it has no specific characteristics apart from the occasional complaint of scalp tenderness to touch (102). Other symptoms of GCA include fever, fatigue, weight loss, jaw claudication, and vision loss (103).

Temporal artery biopsy is the gold standard for establishing the diagnosis of GCA. However, it might not be necessary in case of typical symptoms and specific ultrasound or MRI findings (104). Colour duplex ultrasonography of the temporal arteries remains an important and widely available imaging modality of GCA. The halo sign (dark, hypoechoic circumferential wall thickening) is highly sensitive and specific to GCA (102). Meanwhile, MRI and MRA enable the evaluation of vessel wall inflammation. The sensitivity and specificity of MRI for GCA ranges from 68% to 89% and from 73% to 97% respectively (104). MRA can detect an irregular outline and diameter changes of the arteries wall (101). In cases of GCA, CT is useful when diagnosing concentric mural thickening which continues over long segments and indicates vessel inflammation, while CT angiography is more suitable in the assessment of stenotic and aneurysmal lesions of arteries that develop as complications (105). Further detection of inflammatory changes in the blood vessels can be achieved through 18F-FDG-PET (often combined with CT) based on the uptake of the radioligand. However, in comparison to MRI, this diagnostic method has lower sensitivity and specificity (77% and 66% accordingly) (106, 108).

HEADACHE ATTRIBUTED TO PRIMARY OR SECONDARY ANGIITIS OF THE CENTRAL NERVOUS SYSTEM (PACNS AND SACNS)

Angiitis of the central nervous system (CNS) refers to a broad spectrum of diseases that result in inflammation and destruction of arteries and veins of the brain, spinal cord, and meninges. Inflammation typically causes medium or small brain blood vessels to become narrowed, occluded, and thrombosed, which results in brain tissue ischemia and necrosis (17). Angiitis of the CNS could be either primary (confined to the CNS) or secondary (part of a multisystem inflammatory disease) (107). PANCS is a rare disease with an incidence of 2.4 per 1 million inhabitants (108). Headache is the dominant symptom of both primary and secondary types of angiitis. Typically it is subacute, insidious, and diffuse but may present in a variety of other characteristics. However, a thunderclap headache should raise suspicion of a reversible cerebral vasoconstriction syndrome which often mimics PACNS (109). Other symptoms of angiitis of the CNS include cognitive impairment, focal deficits, seizures, cranial nerve involvement, myelopathy, and ataxia. Weight loss, fever, or the involvement of visceral organs are usually signs of systemic vasculitis (110). Conventional cerebral angiography is often considered to be the radiological gold standard for the diagnosis of PACNS/SACNS. The typical angiographic finding is defined as beading (alternating areas of stenosis and dilatation) (110). However, some studies have shown that the sensitivity and specificity of cerebral angiography for PACNS might be as low as 70% and 30% respectively (109).

In comparison, MRI has a high sensitivity of 90-100% for diagnosing PACNS but a low specificity. Most common MRI findings, occurring in approximately 53% of patients, are multifocal brain infarcts, while parenchymal hemorrhage, leptomeningeal and parenchymal enhancement are observed less frequently (110, 113, 114). MRA and CTA are less sensitive for angiitis of the CNS than conventional cerebral angiography or MRI. They are useful in evaluating large brain vessels, but angiitis of the CNS typically involves medium and small vessels (107). Brain tissue bi-

opsy of radiographically involved areas remains the gold standard for establishing the diagnosis of PACNS (113).

HEADACHE ATTRIBUTED TO CERVICAL CAROTID OR VERTEBRAL ARTERY DISORDERS

Headache or facial or neck pain associated to cervical carotid or vertebral artery dissection

Cervical artery dissection (CAD) is a tear of the carotid or the vertebral artery wall resulting in the formation of a false lumen and intramural hematoma (114). It has an incidence of 2.6-5 per 100 000 inhabitants per year (8, 117). CAD accounts for 10% to 25% of ischemic strokes in young adults and some cases may also cause a subarachnoid hemorrhage (116). The expanding intramural hematoma of CAD may lead to local compression of adjacent nerves causing pain, lower cranial neuropathies or cervical nerve root damage (116, 119). Headache (with or without the pain of the neck) is the most common and sometimes the only manifestation of CAD occurring in 55-100% of cases (30). Pain is often unilateral (ipsilateral to the dissected artery), sudden, severe, prolonged (up to 3 months after the stabilization of CAD), and associated with Horner's syndrome, tinnitus or palsy of the 12th cranial nerve (30). In rare cases, the headache may not resolve within three months after the stabilization of CAD and become persistent (30). On the whole, the diagnosis of CAD is based on the detection of loss of integrity of the carotid or the vertebral artery wall. Ultrasound may visualize the lumen, the wall of the artery and the surrounding tissue. The most common findings of ultrasound in the case of CAD include an intramural hematoma, an echogenic intimal flap, floating thrombus within the vascular lumen, and tapering of the arterial lumen (117, 120). Doppler sonography reveals a bidirectional high resistance flow, reduced blood flow velocity or absence of flow, and no flow in the false lumen (119). The sensitivity of ultrasound for CAD is approximately 70% – 86%. Thus other neuroimaging modalities such as MRI/MRA or CTA are needed to establish the diagnosis (45, 122). MRI provides information about the occurrence of intramural hematoma, and MRA evaluates the

vascular lumen (116). The sensitivity and specificity of MRA and CTA for CAD are relatively similar (119, 123). However, CTA is used more often due to its wide availability and fast scanning speed (122). Conventional angiography for CAD is performed only in questionable cases due to its invasiveness and inability to evaluate the arterial wall. Usual signs of conventional angiography of CAD include vessel stenosis or occlusion, false or double lumen, pseudoaneurysm, irregular dilatation and, intimal flap (118). Conventional angiography used to be the gold standard for CAD, but nowadays it is replaced by MRA and CTA due to its high accuracy and wide availability (122).

POST-ENDARTERECTOMY HEADACHE

Carotid endarterectomy is a neurosurgical procedure performed to remove the atherosclerotic plaque from the inside of an artery and reestablish the diameter of the vessel lumen to prevent strokes (125, 126). There are three different types of headaches associated with carotid endarterectomy. The first type of pain is the most common. It occurs within the first few days after surgery as a diffuse and mild headache. The second type resembles a cluster headache occurring once or twice a day for roughly two weeks. The third type of headache is unilateral, pulsating and severe (30). It usually begins three days after surgery due to the hyperperfusion syndrome which is marked by an increase of cerebral blood flow, seizures, focal neurological deficits and may cause cerebral hemorrhage (125). Hyperperfusion can be detected via transcranial doppler which directly measures blood flow velocity of the middle cerebral artery (126). MRI and CT findings are indirect and include white matter edema, cerebral infarction, or hemorrhage, while perfusion-weighted MRI and single-photon-emission CT may directly indicate an increased cerebral blood flow (129, 130).

HEADACHE ATTRIBUTED TO THE CAROTID OR VERTEBRAL ANGIOPLASTY OR STENTING

Angioplasty or stenting of the carotid or the vertebral arteries is endovascular procedures performed to treat cervical artery stenosis and decrease the risk of stroke (129). Headache and

sometimes pain of the neck occur in one-third of patients and has a mild, ipsilateral, and pressing quality. Pain begins within one week and resolves within one month after the endovascular procedure (30). The cause of headache associated with angioplasty or stenting of the carotid or the vertebral arteries is the hyperperfusion syndrome which has already been described in the previous section (126, 131). Imaging modalities are utilized only when there is suspicion of other conditions or complications of the procedure.

Headache attributed to cranial venous disorder Cerebral venous thrombosis (CVT) is a potentially lethal condition and is most common in adults (with a mean age of 39 years), more so in women than in men (130). The incidence of this condition is 1.3 per 100 000 adults and maybe even higher in developing countries (131). A severe slow-onset diffuse headache is a common manifestation, occurring in more than 90% of cases, and usually accompanied by focal neurological symptoms that are a sign of a brain parenchymal lesion, and/or seizures that occur in 40% of all CVT cases (132, 134). Rarely the headache presents unilaterally, suddenly, thunder-likely, or mildly, not unlike a migraine (30).

Although CVT is a rather rare condition, early diagnosis and treatment, which are heavily dependent on the knowledge of neuroimaging methods and signs, are crucial (133). As usual, the primary imaging modality in the emergency department is non-contrast CT, which is often insufficient for diagnosis. However, increased attenuation of the obstructed cortical vein ("cord sign"), dural or the posterior portion of the superior sagittal sinus ("dense triangle sign") is indicative of CVT (136, 137). Additionally, Hounsfield unit (HU) to hematocrit ratio measurement has been suggested as a rather sensitive diagnostic criterion for CVT. However, further studies are required (136). In contrast-enhanced CT CVT manifests as the "empty delta sign": a contrast-enhanced wall of the thrombosed posterior superior sagittal sinus (137). Further indirect signs of CVT can be observed in CT scans: dilation of the venous structures, small ventricles, brain parenchymal lesions, falx and tentorium enhancement (138). Unfortunately, neither contrast-enhanced nor non-contrast negative

CT scans can rule out CVT.

In cases of CVT, MRI and MRV are the preferred modalities in all stages (133). MRV and CTV are both adequate for assessing changes in the venous system. However, CTV is inferior for the visualization of changes in the brain parenchyma (136, 141, 142). CTV is superior to Time-of-Flight MRV when diagnosing partial vessel occlusion (141). MRV as a separate imaging modality is not sufficient. CVT diagnosis requires a full MRI in addition to MRV (141, 144). The signal intensity of the thrombus depends on its age (139), and specific sequences have their advantages: susceptibility weighted or T2*W GE sequences are most beneficial when evaluating the obstruction in an acute setting or of the cortical vein (143). Contrast-enhanced MRV is superior to Time-of-Flight MRV for assessing smaller sinuses or slow blood flow (144). All in all, neither MRI nor CT is sufficient, and CTV or MRV are necessary when clinical suspicion of CVT is high (Figure 7). Catheter angiography is considered to be the most accurate diagnostic tool; however, due to its invasive nature, this method is rarely applied in clinical practice (135, 147).

Another reason for headaches, related to the cranial venous sinuses, is stenting. It is the most common adverse effect of the procedure, which occurs ipsilaterally to the stent and lasts for a few days. The precise frequency is difficult to determine due to many other stent unrelated types of headaches that patients experience following the procedure (146). The aforementioned adverse reaction to the cranial venous sinus stenting needs to be differentiated from other conditions, such as complications or comorbidities. However, neuroimaging has no different role to play in the diagnosis of this type of headache.

HEADACHE ATTRIBUTED TO OTHER ACUTE INTRACRANIAL ARTERIAL DISORDER

INTRACRANIAL ENDARTERIAL PROCEDURE RELATED HEADACHE AND ANGIOGRAPHY HEADACHE

Headaches associated to intracranial end-arterial procedures (IEP) include angioplasty, embolization, stenting, and typically develop within

the first week and resolve within a month, while headaches attributed to angiography develop within a day and resolve in 72 hours after the procedure (30). Typically, they are different in types of severity and duration; symptoms may be migraine-like in patients with an underlying migraine. IEP related headaches are typically unilateral (30). However, head imaging is required only when there is suspicion of complications, such as stent thrombosis or stroke.

Headache attributed to RCVS

Reversible cerebral vasoconstriction syndromes (RCVS) are known as a group of conditions that clinically manifest during physical exertion, sexual activity, Valsalva maneuvers, bathing, or emotional stress as a thunderclap headache due to a reversible multifocal dilation and constriction of the cerebral arteries (29, 149). Although the precise incidence is not known, it is believed that the condition is relatively common (112). RCVS is considered the most common cause of thunderclap headache in patients without an aneurysmal subarachnoid hemorrhage, and the most common recurrent thunderclap headache (148). The thunderclap headache can be accompanied by nausea, photosensitivity, and focal deficits (151, 152). Additionally, a small percentage of RCVS patients report atypical headaches (151, 152). RCVS can lead to various types of intracranial hemorrhages (convexal subarachnoid, intracerebral, subdural hemorrhages), as well as posterior reversible encephalopathy syndrome (PRES) and ischemic stroke (151).

The prevention of the complications above requires early diagnosis and management of the RCVS (152–154). Imaging is an indispensable part of the diagnostic workup. However, various means of evaluation can be utilized: angiography, transcranial Doppler sonography, CT or MR angiography. More than a third of initial CT/MRI scans are normal in the presence of cerebral vasoconstriction (114, 151, 152). Nonetheless, imaging evaluation should begin with non-contrast CT. Convex subarachnoid hemorrhage especially in patients younger than 60 years of age, signs of previous and/or current multifocal infarcts, and typical clinical findings should raise suspicion of RCVS (157, 158). Further assessment requires CT angiography, MR angiography or conven-

tional angiography. CT angiography is less sensitive than conventional angiography; however, it is the setting of proximal branch involvement, CTA detects the segments of vasoconstriction in addition to possible comorbidities or complications (157).

MRI is superior to CT when evaluating possible complications and alternative diagnoses, yet remains insufficient for the diagnosis of RCVS (151, 152, 159). Hyperintense vessels along cerebral sulci in T2 FLAIR imaging, while not specific, are indicative of RCVS and higher risk of ischemic stroke and PRES incidence (152, 160, 161). Although MRA is less sensitive than conventional angiography, it is often utilized because of the non-invasive nature (155). MRA is used to assess the extent, distribution, and progression of the arterial constriction and associated complications (160). Even transcranial ultrasound has been utilized. However, this modality cannot exclude the diagnosis or RCVS (161).

Conventional cerebral angiography, although invasive, is considered to be the gold standard (151, 157). It has the superior spatial resolution to MRA and CTA and enables the assessment of small and distal cerebral arteries, which is why MRA and CTA sensitivity for RCVS-related arterial stenoses is 80% in comparison to conventional angiography (162, 164). Typical angiography findings in RCVS are segments of arterial constriction and dilatation, known as 'string of beads' or 'sausage on a string' signs (162).

Certain conditions, especially primary angiitis of the CNS, may manifest similarly to RCVS. Imaging plays a critical role in differentiation (155). Vessel Wall Imaging is an MR technique, useful when differentiating vasculitis from RCVS among other things. RCVS related wall thickening is less often enhanced, unlike in the setting of central nervous system vasculitis (165, 166). Perfusion imaging enables the detection of multifocal hypoperfusion areas, which helps with the evaluation of progression and treatment response in addition to the effects of specific segment stenosis (167, 168).

Persistent RCVS related headaches are longer than three months and persist even after the cerebral arteries normalize (30).

Headache attributed to intracranial artery

dissection

Intracranial artery dissection (IAD) is best known for its association with severe subarachnoid hemorrhages that tend to recur (169, 170). Headaches attributed to IAD present unilaterally and suddenly and may progress as subarachnoid hemorrhage or stroke (29, 171). The precise incidence is not known, however, it is believed to be less than 2.6 - 3.0 per 100 000 people (170).

Clinical presentation is not specific, and imaging evaluation is not always conclusive. Typical radiological signs include mural hematoma, intimal flap, and a double lumen (170). It is important to note that no modality can detect all of these findings, seeing as CT and MRI visualize the extraluminal, while CT/MR/conventional angiography detects intraluminal changes. In the setting of IAD, a mural hematoma is associated with enlarged external diameter, which is not related to other conditions that can manifest as intramural hematomas as well (170). 2 - 3 days following the onset of the IAD, MRI T1W sequence and exceptionally high-resolution 3 Tesla MRI that includes three-dimensional fat-suppressed T1W images with a black-blood effect can detect the hyperintense hematoma (171). An intimal flap is best observed in digital subtraction angiography (170). Dissection may also be accompanied by aneurysmal dilatation, which indicates a higher risk of subarachnoid hemorrhage, while segmental stenosis and occlusion in subarachnoid haemorrhage is indicative of IAD (172, 174, 175). CTA and MRA are useful when diagnosing intraluminal changes, while digital subtraction angiography is utilized only in cases of negative CT/MRI, before surgical or endovascular treatment, and when patients present with subarachnoid hemorrhage (170). Depending on the findings, a combination of CT/MRI and intraluminal imaging is often required to confirm the diagnosis of IAD.

HEADACHE ATTRIBUTED TO GENETIC VASCULOPATHY

HEADACHE ATTRIBUTED TO CADASIL

Cerebral Autosomal Dominant Arteriopathy with Subcortical Infarcts and Leukoencephalopathy (CADASIL) is a small vessel disease de-

terminated by a mutation in the NOTCH3 gene (174). It is considered to be the most frequent of all small vessel diseases and hereditary stroke disorders with a prevalence of approximately 2-5 cases per 100 000 inhabitants (11, 176–179). It manifests by the late middle age most frequently as a migraine with prolonged aura (29, 180). Additional symptoms include transient ischemic attacks and strokes, cognitive impairment, changes in mood and gait, epilepsy, and others (179). Neuroimaging plays a significant role in the diagnosis of CADASIL, even in patients presenting with no symptoms whatsoever (180). Typically, CADASIL is differentiated from other small vessel diseases by detecting early subcortical ischemic changes that progress to involve the anterior temporal poles and less frequently the external capsule or the superior frontal gyrus (182, 183). MRI T2W and FLAIR sequences show the extent and age of the white matter abnormalities that typically progress with years, while the DW sequence enables the quantification of chronic white matter changes (184, 185). Other less prevalent pathological MRI findings, common to CADASIL are CSF filled lacunas, cortical infarctions, and involvement of corpus callosum (182, 185, 186).

Other imaging modalities are less sensitive when detecting changes, common to CADASIL. In the preliminary stages of the disease, CT imaging may reveal nonspecific periventricular white matter hypodensities. However, the common anterior temporal lobe abnormalities can be diagnosed only in the advanced stages of CADASIL (181). Therefore, CT may indicate the disease. However, MRI is necessary to confirm the diagnosis (Figure 8). Few studies analyze the diagnostic value of FDG-PET and diffusion tensor imaging. However, even those studies suggest that findings are not specific to CADASIL (181). Headache attributed to MELAS

Mitochondrial Encephalopathy, Lactic Acidosis and Stroke-like episodes (MELAS) are known as one of the maternally inherited mitochondrial metabolic diseases that often manifest before the fourth decade of life as a multisystemic disorder (186). Certain features of MELAS overlap with CADASIL, but the main symptoms include migraine-like attacks, stroke-like episodes, and

encephalopathy often with dementia and/or seizures (187).

The clinical manifestation of MELAS is intricate. Nonetheless, brain imaging visualizes white and grey matter changes that are characteristic and aid the diagnosis of MELAS. In patients, presenting with stroke-like symptoms, infarction simulating lesions are unlike the vascular territories, develop slowly, may change location, and progress into atrophic regions with time (189, 190). Typically, the involvement of parietal and occipital lobes is observed (189). While MRI findings are similar to CADASIL (both conditions are known for the subcortical white matter damage), cortical area involvement with vasogenic edema and mass effect in acute and subacute phases is more indicative of MELAS (190). Seeing as typical radiological findings are brain parenchymal lesions, MRI is the preferred modality (189, 192). Common CT scan findings include bilateral basal ganglia and thalamic calcifications (192). DWI is useful when differentiating cytotoxic from vasogenic edema, the latter usually but not always manifesting in MELAS as elevated ADC and sometimes progressing to cytotoxic (193–198). SPECT findings differ between studies and depend on the acuity of MELAS (198, 200–202). CTA, MRA, and catheter angiography may be utilized to evaluate the obstruction of cerebral arteries and in MELAS; it is common to find the arteries of the seemingly ischemic zones to be patent (201). Other imaging modalities, such as PET, Arterial Spin Labeling, Oxygen Extraction Fraction, Magnetoencephalography, and transcranial ultrasound may be utilized when there are doubts concerning the diagnosis (202–206).

HEADACHE ATTRIBUTED TO MMA

Moyamoya angiopathy (MMA) is described as a chronic progressive disease, defined by an abnormal vasculature at the base of a brain following bilateral stenosis and/or occlusion of the terminal inferior cerebral artery branches (207). This disease is most prevalent in Asia, with 10.4 cases per 100 000 patients in Japan (208). MMA is yet another condition, associated with recurring and migraine-like headaches, which may manifest as a stroke in early childhood or adolescence (30). Neuroimaging enables the confirmation of the

diagnosis. Head CT scan visualizes infraction of both cortical and subcortical areas or parenchymal hemorrhages into the basal ganglia, thalamus, ventricles, however, it does not provide information on the vasculature itself (209–211). MRI is more sensitive than CT when diagnosing MMA and enables the detection of findings that suggest MMA even in asymptomatic cases. Characteristic findings indicative to MMA are the dilatation of leptomeningeal and cortical collateral vessels (known as the “ivy sign”), absent flow voids in the distal portions of inferior and middle cerebral arteries, and absent signal in the basal ganglia (212–216). High-resolution MRI further increases the sensitivity of this modality, by visualizing the narrowing of the outer arterial wall diameter, and long-segment concentric enhancement of the inferior or middle cerebral artery. These findings raise the suspicion of MMA even in the early stages (217–220). Other, MMA common findings observed on MRI are ischemic lesions in deep watershed zones (221), and asymptomatic cerebral microbleeds (223, 224). Noninvasive or catheter angiography is required for the detection of steno-occlusion of the inferior, middle, and/or anterior cerebral artery, and grading, according to Suzuki’s six stages (224). Conventional angiography is performed usually in cases when bypass surgery is being considered (212). Additional studies may be utilized for the evaluation of intracranial hemodynamics: transcranial sonography, perfusion CT, MRI, PET, SPECT, arterial spin labeling, etc. (225–230).

HEADACHE ATTRIBUTED TO CAA

Cerebral Amyloid Angiopathy (CAA) is a small and medium-sized vessel disease that affects the walls of the leptomeninges and cerebral cortex vessels due to the accumulation of amyloid- β (231). The prevalence of the disease increases with age and dementia development: autopsy results observed CAA related changes in up to 60% of dementia patients and 28–38% of nondementia patients (232). Patients suffer from late-onset auras, typically without or with a mild headache as well as other typical CAA dementia symptoms (30).

Although definite diagnosis requires validation by pathological brain tissue examination, neuro-

imaging can detect findings indicative of CAA (233). Lobar hemorrhages, commonly in the temporal and occipital regions, usually visualized by T2*W GE MRI sequences, raise suspicions of CAA in dementia patients (234, 235). Although CAA may be the reason for ICH, it has been concluded that the vast majority of CAA patients do not suffer ICH (235).

In patients over 60, CAA is considered to be the most common cause of convex subarachnoidal hemorrhage (156), which in turn increases the risk of future ICH (236). Another finding, common to small vessel disease, is cerebral microbleeds, which are seen as small hypointense areas on blood-sensitive T2*W GE or susceptibility-weighted MRI sequences (237). Cerebral microbleeds correlate with microvascular leakage and are not specific to any condition. However, lobar cerebral microbleeds are indicative of CAA and increased intracerebral hemorrhage and ischemic stroke risks (237–242). White matter hyperintensity (leukoaraiosis) is a specific diagnostic term, which is used to describe low-density areas on CT scans and high signal areas on T2W MRI scans. It has been hypothesized that particular localization (occipital region) of leukoaraiosis may indicate CAA, even though white matter hyperintensity is common in most small vessel disease (243).

Meanwhile, cortical superficial siderosis is identified by specific MRI sequences and occurs more often in CAA patients than in the general population (Figure 9) (245, 246). In addition, cortical superficial siderosis indicates a high risk of recurrent ICH (246). Finally, PET assessment of amyloid deposit localization has diagnostic value and may predict the occurrence of CAA related ICH (247).

HEADACHE ATTRIBUTED TO RVCLSM

Retinal vasculopathy with cerebral leukoencephalopathy and systemic manifestations (RVCLSM) is a hereditary neurovascular syndrome caused by mutations in the TREX1 gene (248). This condition is best known for retinal vasculopathy, brain dysfunction, in addition to white matter and intracerebral mass lesions on neuroimaging, while systematic manifestations are less frequent (248). The headache is defined as mi-

graine-like episodes, often without aura, with or without other clinical features (30).

The diagnosis is based on genetic testing, while characteristic neuroimaging manifestations occur and progress from the fifth decade (249). CT is not sufficient as the disease affects mostly the white matter of the brain and merely focal calcifications can be observed (248). MRI is superior and can detect punctate non-enhancing T2-hyperintense lesions in the periventricular and subcortical white matter, or enhanced punctate lesions either with DWI related restriction or with various rim enhancements (more familiar to the later stages) that are generally associated with edema and mass effect (248). Typical enhanced lesions as seen on an MRI are considered to be the major diagnostic criteria, while the aforementioned non-enhanced MRI and focal calcifications on CT are minor criteria of the RVCLSM (248).

HEADACHE ATTRIBUTED TO OTHER CHRONIC INTRACRANIAL VASCULOPATHY

In theory, all intracranial vasculopathy can cause migraine-like attacks. However, this group includes migraine-like headaches with and without aura by any chronic vasculopathy (30). There are no specific neuroimaging indications or findings. Thus the imaging evaluation of these headaches is not discussed in this review.

HEADACHE ATTRIBUTED TO PITUITARY APOPLEXY

Pituitary apoplexy (PA) is a potentially life-threatening clinical syndrome that is characterized by the sudden enlargement of the pituitary gland frequently following infarction of a preexisting pituitary adenoma (250). It is a rare condition with an estimated 6.2 cases per 100 000 inhabitants (251). PA often manifests as a sudden and severe thunderclap headache, commonly accompanied by visual disturbances, diplopia, changes in consciousness, less frequently nausea, vomiting, and hypotension (253, 254).

Imaging plays a crucial role in the diagnosis of PA. It helps to rule out other conditions, such as subarachnoid hemorrhage, meningitis, cerebral sinus thrombosis, midbrain infarction, migraine, and aneurysms (250). The measurement

of the pituitary mass influences clinical decisions (252). Due to the sudden onset of the condition, the first diagnostic test is usually a non-contrast CT of the head. However, in cases of a negative CT, patients should undergo an MRI scan, seeing as MRI is far more accurate when diagnosing subacute PA (253, 255–257). Two signs of PA can be observed on a CT scan: an interstellar mass (80% of cases) and hemorrhagic components (20–30% of cases) (253, 258). In contrast-enhanced CT certain features of the pituitary tumor may become visible: inhomogeneous enhancement with or without ring enhancement (258). It has been reported that MRI findings are sensitive enough to be comparable to histopathological conclusions (259). T1W sequences are useful for detecting altered signal intensity sella turcica lesions, while T2W images detect hemorrhages (260). T2*W GE imaging increases the sensitivity of blood product detection even further (261). All in all, imaging, especially MRI, plays a crucial role in diagnosis and decision making in the setting of PA (Figure 10).

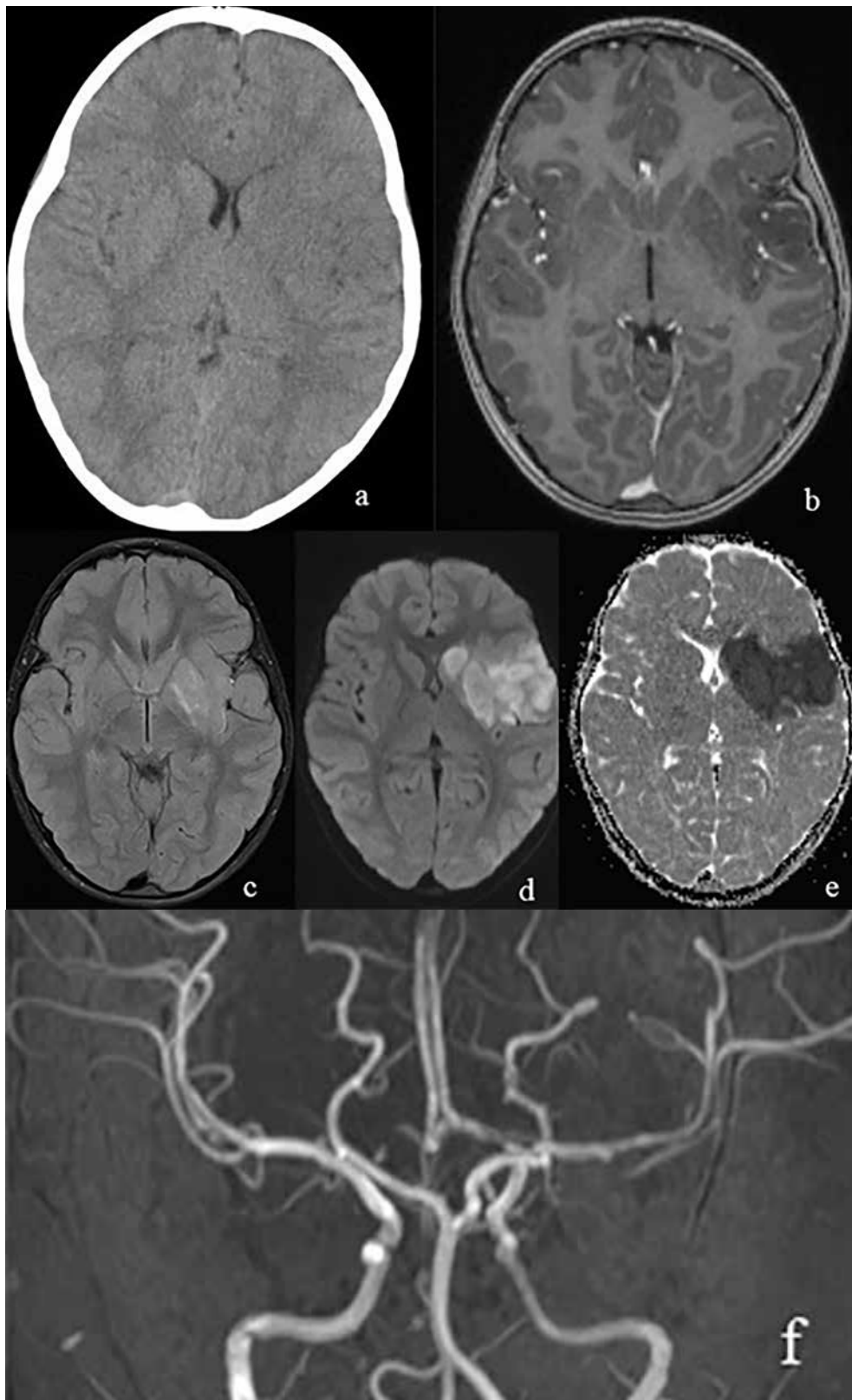


Figure 1. CT and MRI of an ischemic stroke in the left MCA (a - axial CT showing no features of stroke in the early stages; b-f MRI: b - T1W axial; c - T2W FLAIR axial; d - DW axial; e - ADC axial; f - TOF)

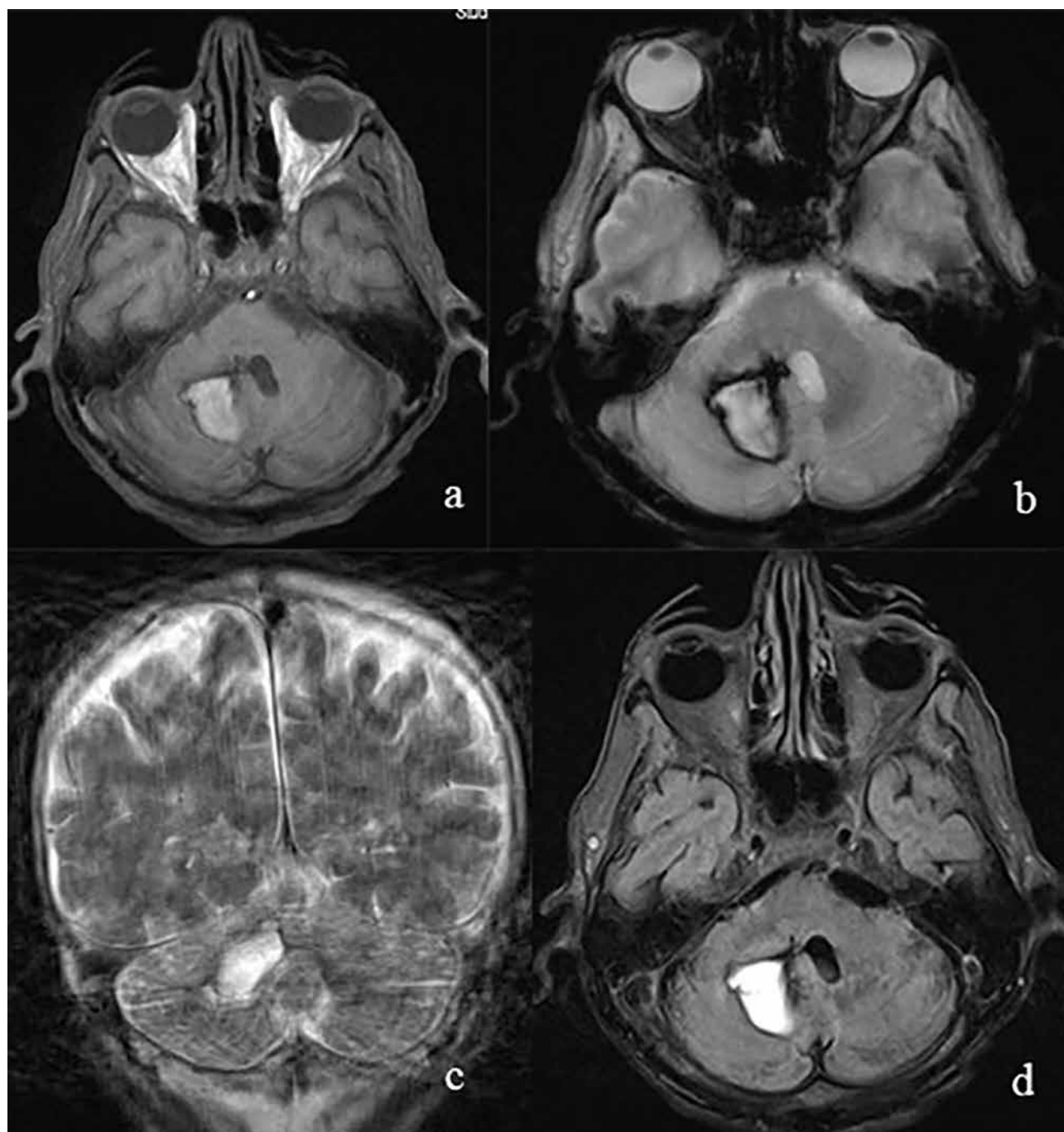


Figure 2. MRI of a non-traumatic haemorrhage at the right cerebellum hemisphere (a -T1W axial; b- T2W f12d hemo axial; c- T2W coronal (movement artefacts); d- T2W FLAIR axial).

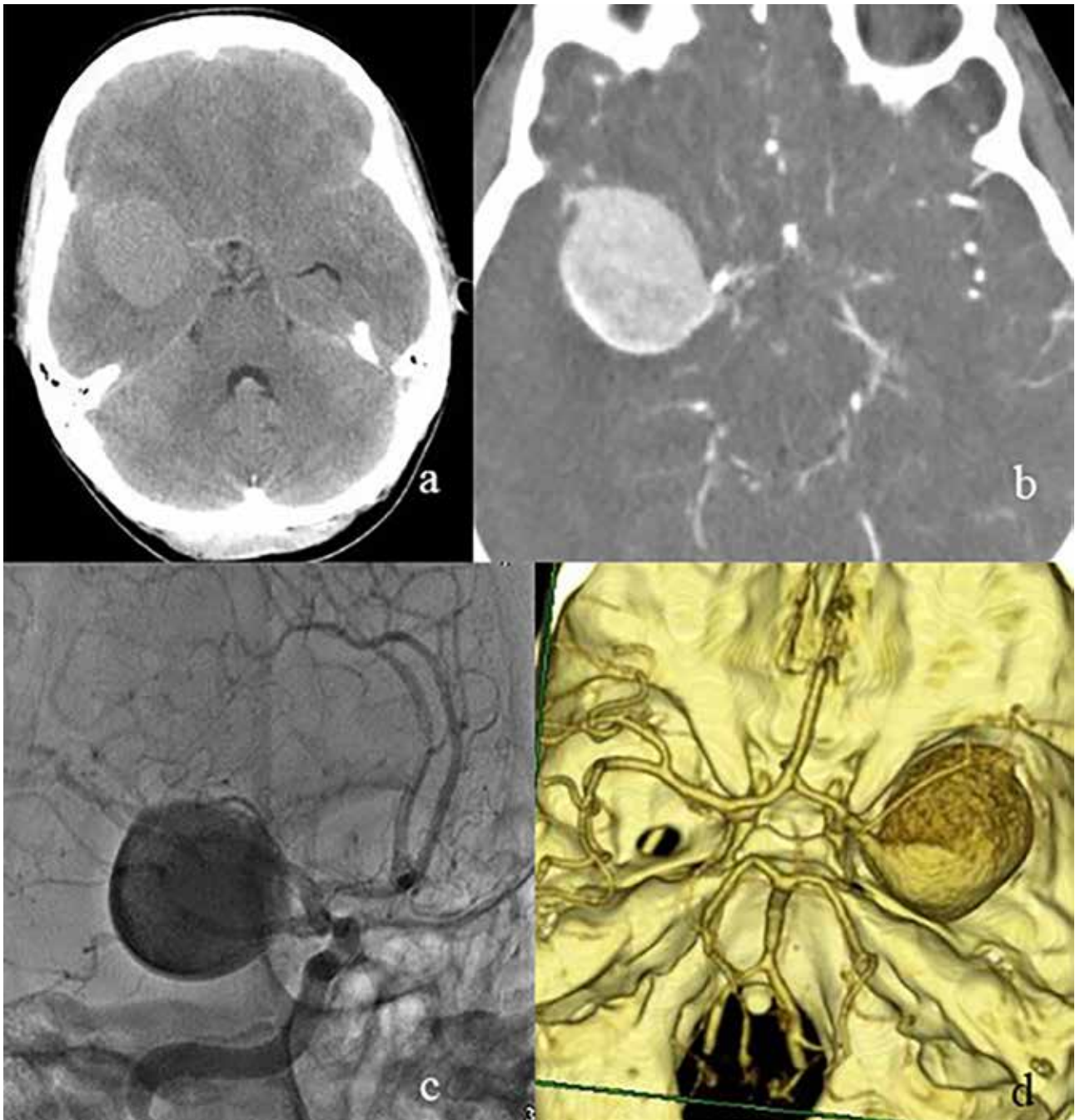


Figure 3. Saccular aneurysm at ACM dex. vessel: a - axial CT; b - CT angiography basic; c - angiography; d - CT angiography 3D reconstruction.

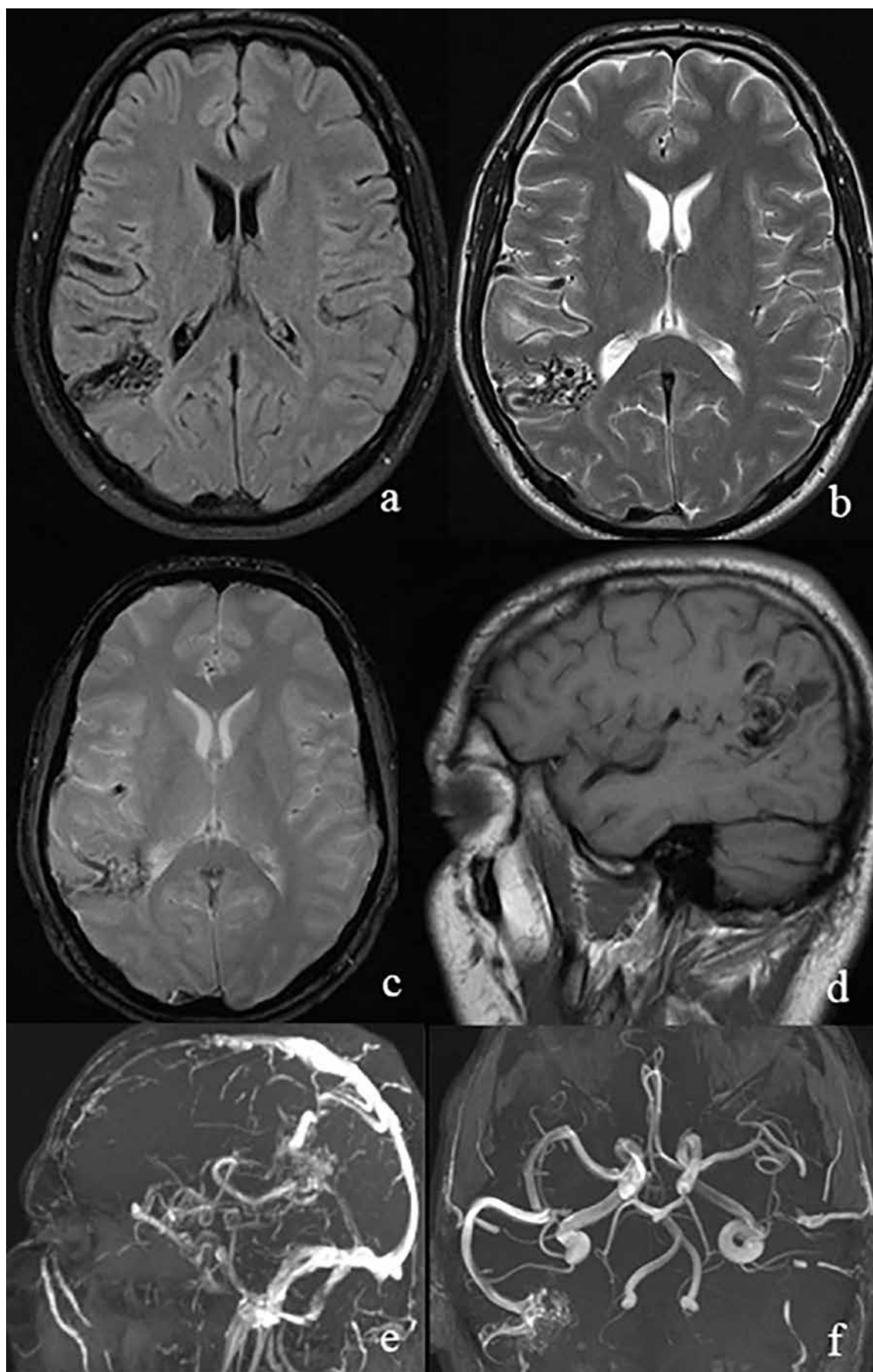


Figure 4. Arteriovenous malformation, MRI (a - T2W FLAIR axial; b - T2W axial; c - T2W fl2d hemo axial; d - T1W sagittal; e - TOF vein; f - TOF arterial).

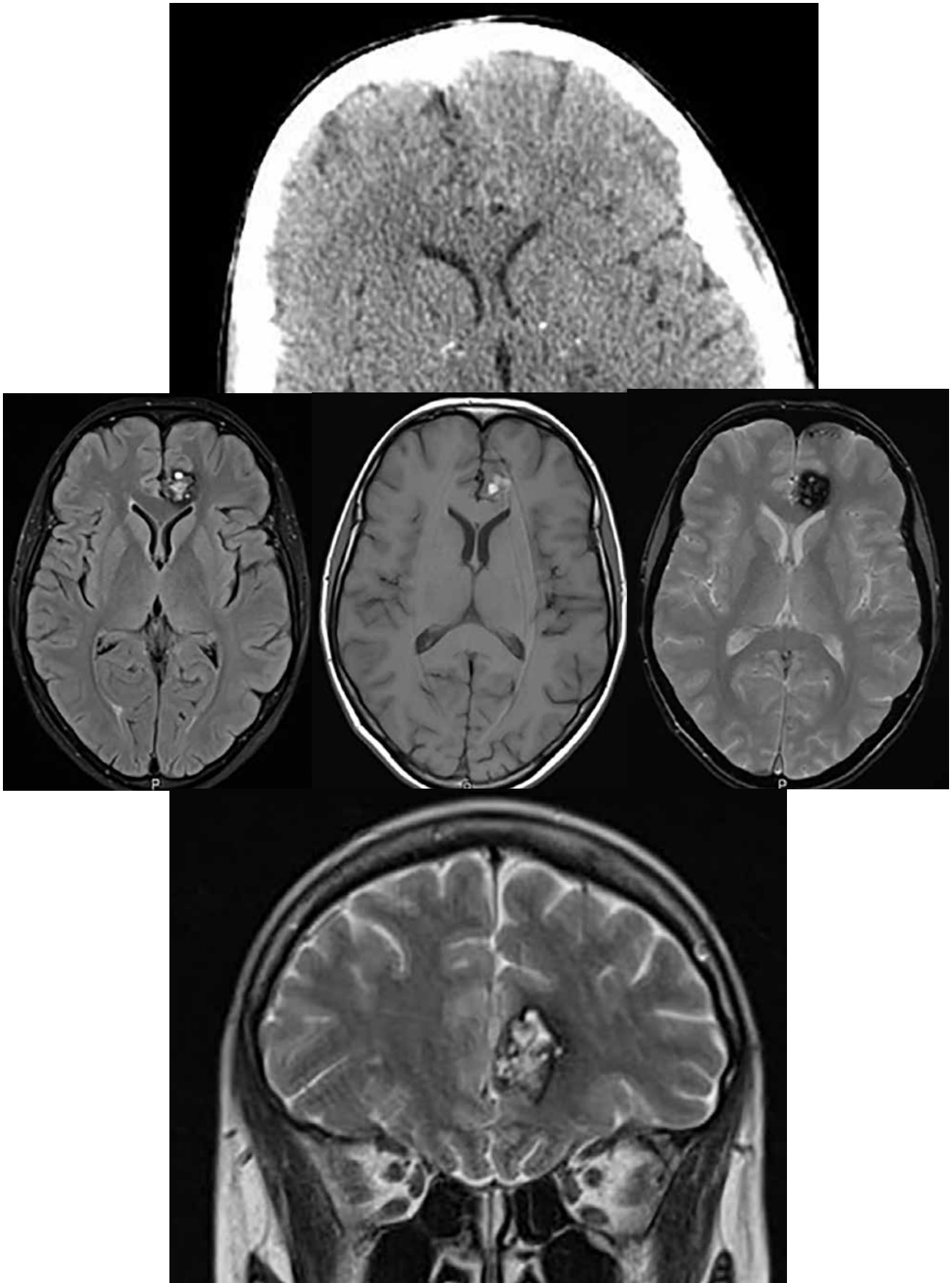


Figure 5. Cavernoma at the left frontal lobe (a - axial CT; MRI: b - T2W/FLAIR axial; c - T1W axial; d - T2W f12 hemo axial; e - T2W coronal).

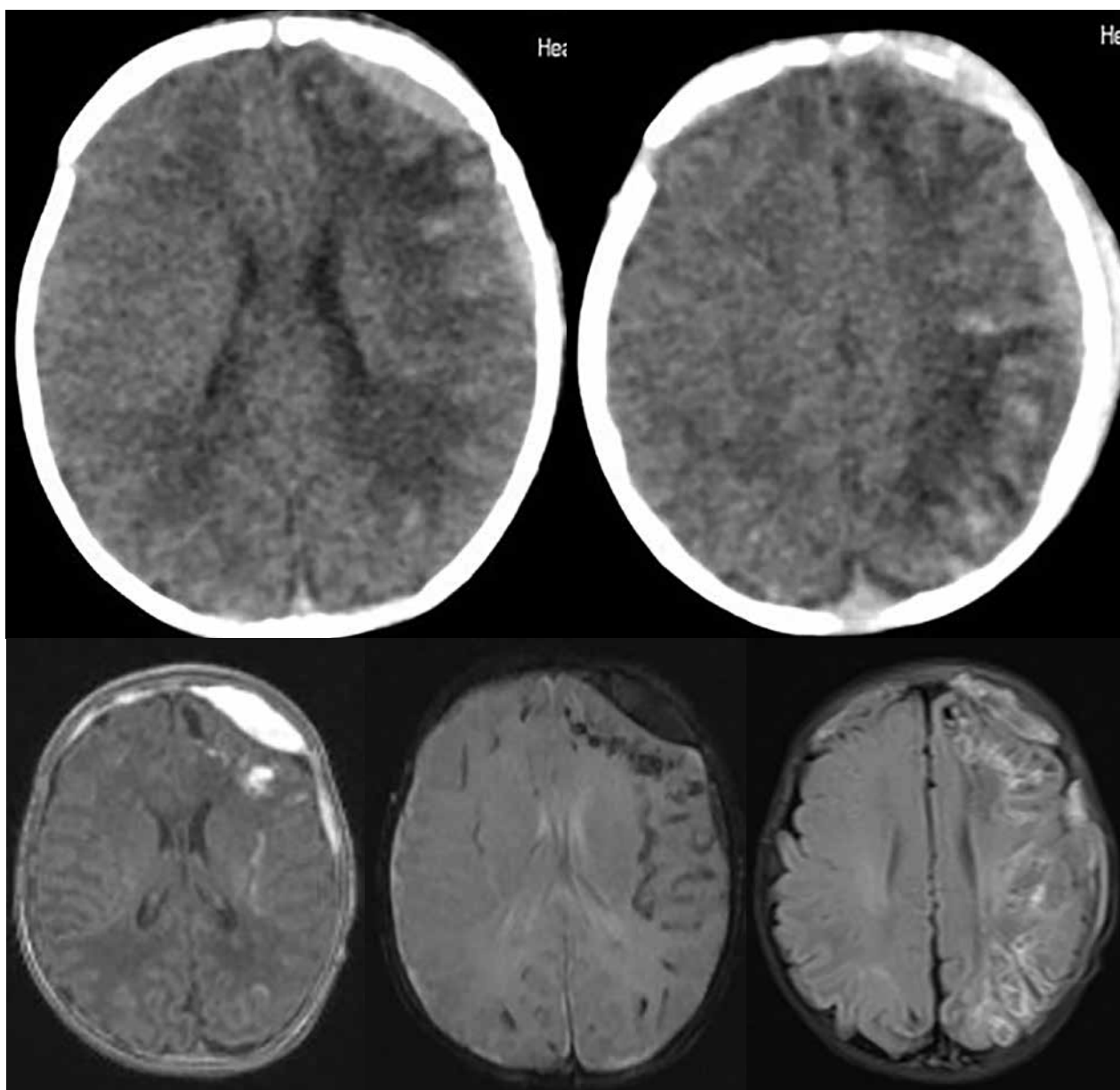


Figure 6. Sturge-Weber syndrome with an acute epidural haematoma at the left frontal lobe as a concomitant pathology (a, b – axial CT; axial MRI: c - T1W; d - T2W fl2d hemo; e - T2W FLAIR).

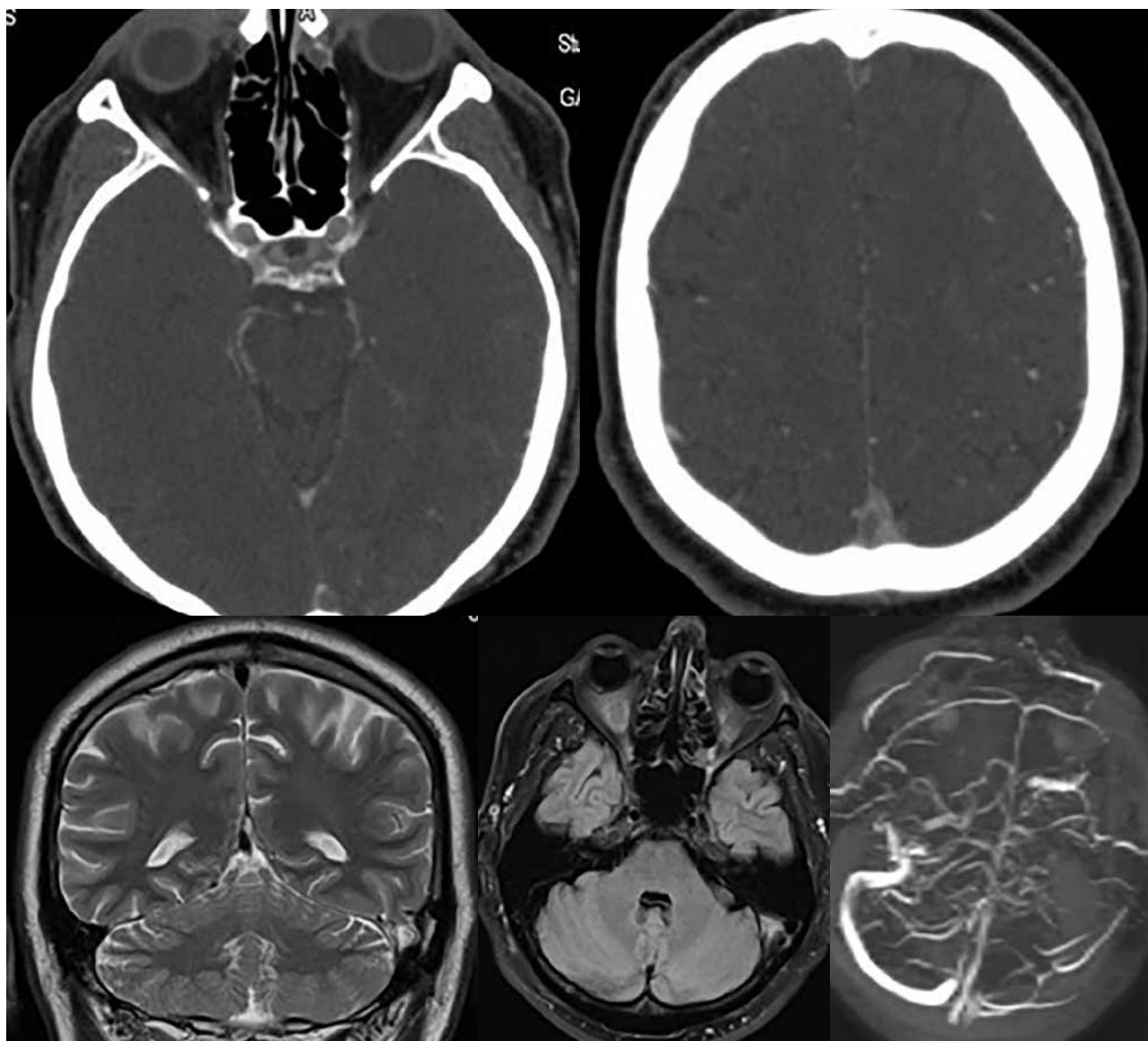


Figure 7. Multiple different venous sinus thromboses (thrombosis of the superior sagittal sinus: a, b - axial CT; and thrombosis of the left transversal sinus vein MRI: c - T2W coronal; d - T2W FLAIR axial; e - TOF).

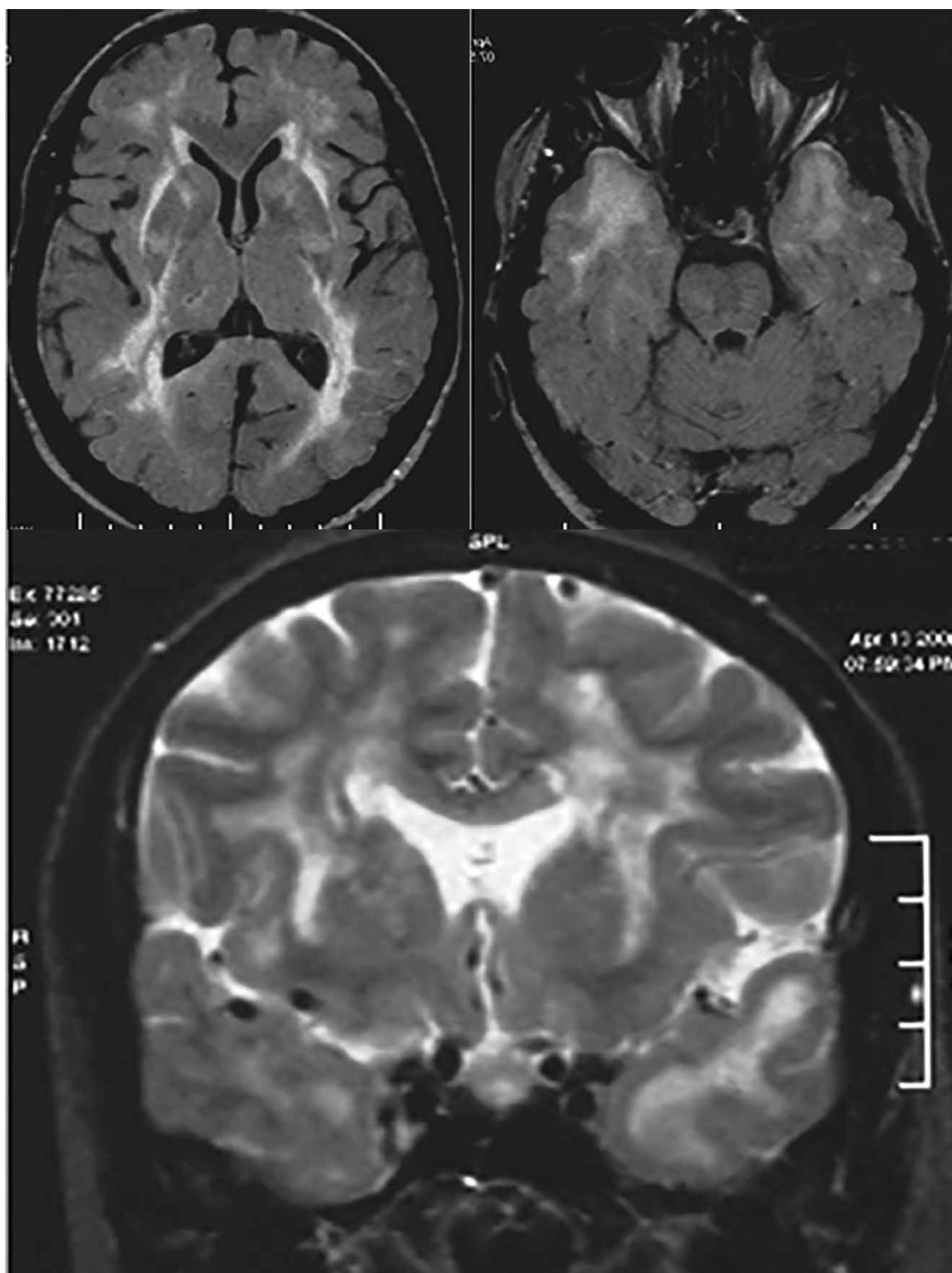


Figure 8. CADASIL, MRI (a, b - T2W FLAIR axial; c - T2W coronal).

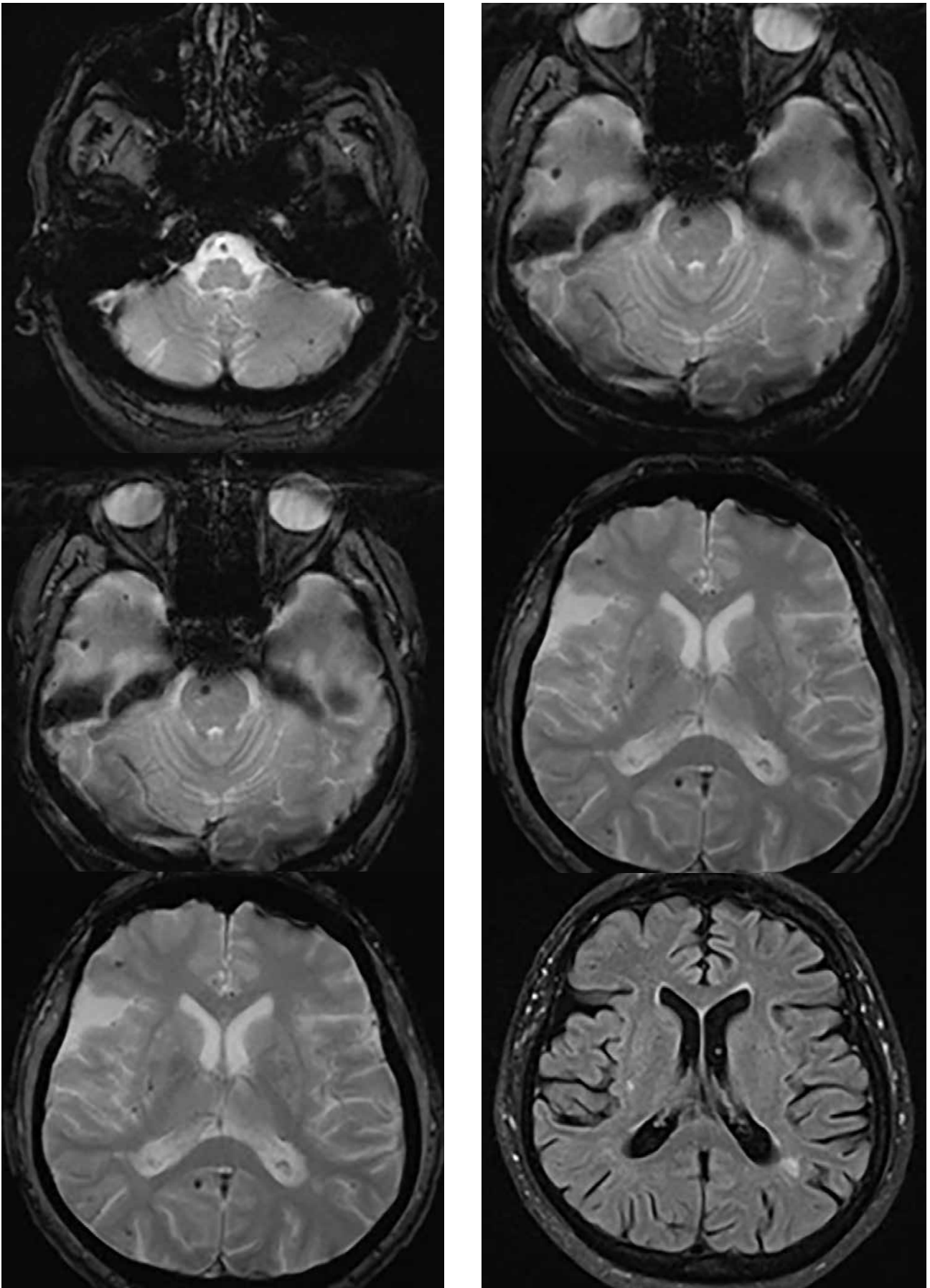


Figure 9. Cerebral amyloid angiopathy and encephalopathy, MRI (a - e T2W fl2d hemo axial; f - T2W/FLAIR axial).

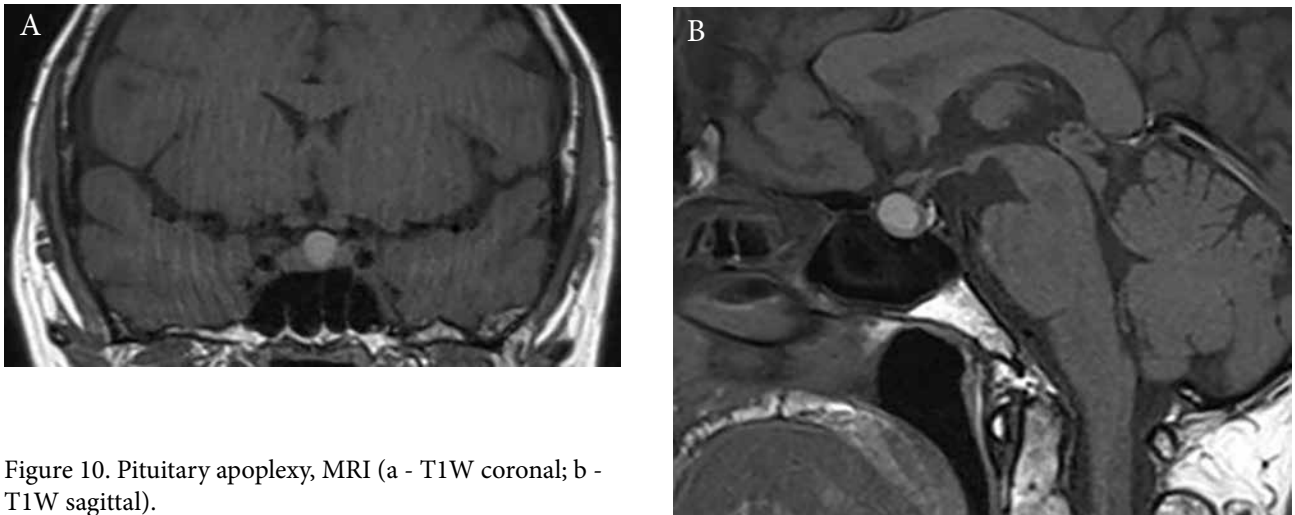


Figure 10. Pituitary apoplexy, MRI (a - T1W coronal; b - T1W sagittal).

CONCLUSIONS

Headaches attributed to cranial and cerebral vascular disorders vary in etiology, clinical and radiological manifestation. Therefore, a good understanding of the purpose that each imaging modality serves is required. CT imaging is a widely available and a quick diagnostic tool which, unfortunately, is also associated with ionizing radiation. MRI is a sensitive brain parenchymal lesion evaluation tool that does not expose patients to radiation and enables the evaluation of small pathological structures in different sequences. However, MRI scans take longer, are more expensive, and not as widely accessible as CT scanners. Other imaging modalities provide additional information on the intraluminal, metabolic, or perfusion changes in the brain when initial imaging is not sufficient and requires clarification.

REFERENCES

- Paul Rizzoli WJM. Headache. *Am J Med*. 2017;325–46.
- Stovner L, Hagen K, Jensen R, Katsarava Z, Lipton R, Scher A, et al. The Global Burden of Headache: A Documentation of Headache Prevalence and Disability Worldwide. *Cephalalgia*. 2007;27(3):193–210.
- Goldstein J, Camargo C, Pelletier A, Edlow J. Headache in United States Emergency Departments. *Cephalalgia*. 2006;26(6):684–90.
- Starling AJ. Diagnosis and Management of Headache in Older Adults [Internet]. Vol. 93, Mayo Clinic Proceedings. Elsevier; 2018. p. 252–62.
- Newell KA. Headache Mistakes You Do Not Want to Make [Internet]. Vol. 2, Physician Assistant Clinics. Elsevier; 2017. p. 503–17.
- Long BJ, Koyfman A. Benign Headache Management in the Emergency Department. *J Emerg Med*. 2018;54(4):458–68.
- Sacco RL, Kasner SE, Broderick JP, Caplan LR, Connors JJ, Culebras A, et al. An updated definition of stroke for the 21st century: A statement for healthcare professionals from the American heart association/American stroke association. *Stroke*. 2013;44(7):2064–89.
- Béjot Y, Bailly H, Durier J, Giroud M. Epidemiology of stroke in Europe and trends for the 21st century. *Press Med*. 2016;45(12):e391–8.
- Pollak L, Shlomo N, Korn Lubetzki I. Headache in stroke according to National Acute Stroke Israeli Survey. *Acta Neurol Scand*. 2016;135(4):469–75.
- Jamieson DG, Cheng NT, Skliut M. Headache and Acute Stroke. *Curr Pain Headache Rep*. 2014;18(9):444.
- Lester MS, Liu BP. Imaging in the Evaluation of Headache. *Med Clin North Am*. 2013;97(2):243–65.
- Hansen AP, Marcussen NS, Klit H, Andersen G, Finnerup NB, Jensen TS. Pain following stroke: A prospective study. *Eur J Pain (United Kingdom)*. 2012;16(8):1128–36.
- Harrison RA, Field TS. Post Stroke Pain: Identification, Assessment, and Therapy. *Cerebrovasc Dis*. 2015;39(3–4):190–201.
- Cassella CR, Jagoda A. Ischemic Stroke: Advances in Diagnosis and Management [Internet]. Vol. 35, Emergency Medicine Clinics of North America. Elsevier; 2017. p. 911–30.
- Powers WJ, Rabinstein AA, Ackerson T, Adeoye OM, Bambakidis NC, Becker K, et al. 2018 Guidelines for the Early Management of Patients With Acute Ischemic Stroke: A Guideline for Healthcare Professionals From the American Heart Association/American Stroke Association. *Stroke*. 2018;49(3):e46–99.
- Vilela P, Rowley HA. Brain ischemia: CT and MRI techniques in acute ischemic stroke. *Eur J Radiol*. 2017;96:162–72.
- Powers WJ, Derdeyn CP, Biller J, Coffey CS, Hoh BL, Jauch EC, et al. 2015 American Heart Association/American Stroke Association Focused Update of the 2013 Guidelines for the Early Management of Patients With Acute Ischemic Stroke Regarding Endovascular Treatment. *Stroke*. 2015;46(10):3020–35.
- Wardlaw JM, Mielke O. Early Signs of Brain Infarction at CT: Observer Reliability and Outcome after Thrombolytic Treatment—Systematic Review. *Radiology*. 2005;235(2):444–53.
- Schröder J, Thomalla G. A critical review of Alberta stroke program early CT score for evaluation of acute stroke imaging. *Front Neurol*. 2017;7:245.
- Jauch EC, Saver JL, Adams HP, Bruno A, Connors JJ (Buddy), Demaerschalk BM, et al. Guidelines for the Early Management of Patients With Acute Ischemic Stroke. 2013;
- Latchaw RE, Alberts MJ, Lev MH, Connors JJ, Harbaugh RE, Higashida RT, et al. Recommendations for Imaging of Acute Ischemic Stroke. *Stroke*. 2009;40(11):3646–78.
- Wintermark M, Professor A, Sanelli P, Albers GW, Bello J, Derdeyn C, et al. Imaging Recommendations for Acute Stroke and Transient Ischemic Attack Patients: A Joint Statement by the American Society of Neuroradiology, the American College of Radiology and the Society of NeuroInterventional Surgery. *AJNR Am J Neuroradiol*. 2013;34(11):117–27.
- González RG. Clinical MRI of acute ischemic stroke. *J Magn Reson Imaging*. 2012;36(2):259–71.
- Lebedeva ER, Gurary NM, Olesen J. Headache in transient ischemic attacks. *J Headache Pain*. 2018;19(1):60.
- Lee W, Frayne J. Transient ischaemic attack clinic: An evaluation of diagnoses and clinical decision making. *J Clin Neurosci*. 2015;22(4):645–8.
- van Asch CJ, Luitse MJ, Rinkel GJ, van der Tweel I, Algra A, Klijn CJ. Incidence, case fatality, and functional outcome of intracerebral haemorrhage over time, according to age, sex, and ethnic origin: a systematic review and meta-analysis. *Lancet Neurol*. 2010;9(2):167–76.
- Meretoja A, Strbian D, Putaala J, Curtze S, Haapaniemi E, Mustanoja S, et al. SMASH-U: A proposal for etiologic classification of intracerebral hemorrhage. *Stroke*. 2012;43(10):2592–7.
- Koivunen R-J, Satopää J, Meretoja A, Strbian D, Haapaniemi E, Niemelä M, et al. Incidence, risk factors, etiology, severity and short-term outcome of non-traumatic intracerebral hemorrhage in young adults. *Eur J Neurol*. 2015;22(1):123–32.
- Rothrock JF. Headaches caused by vascular disorders. *Neurol Clin*. 2014;32(2):305–19.
- (IHS) HCC of the IHS. Headache Classification Committee of the International Headache Society (IHS) The International Classification of Headache Disorders, 3rd edition. *Cephalalgia*. 2018;38(1):1–211.
- Alerhand S, Lay C. Spontaneous Intracerebral Hemorrhage. In: Emergency Medicine Clinics of North America. Elsevier; 2017. p. 825–45.
- Chalela JA, Kidwell CS, Nentwich LM, Luby M, Butman JA, Demchuk AM, et al. Magnetic resonance imaging and computed tomography in emergency assessment of patients with suspected acute stroke: a prospective comparison. *Lancet*. 2007;369(9558):293–8.
- Fiebach JB, Schellinger PD, Gass A, Kucinski T, Siebler M, Villringer A, et al. Stroke magnetic resonance imaging is accurate in hyperacute intracerebral hemorrhage: a multicenter study on the validity of stroke imaging. *Stroke*. 2004;35(2):502–6.
- Safatli D, Günther A, Schlattmann P, Schwarz F, Kalff R, Ewald C. Predictors of 30-day mortality in patients with spontaneous primary intracerebral hemorrhage. *Surg Neurol Int*. 2016;7(19):510.
- Wada R, Aviv RI, Fox AJ, Sahlas DJ, Gladstone DJ, Tomlinson G, et al. CT Angiography “Spot Sign” Predicts Hema-

- toma Expansion in Acute Intracerebral Hemorrhage. *Stroke*. 2007;38(4):1257–62.
36. Demchuk AM, Dowlatshahi D, Rodriguez-Luna D, Molina CA, Blas YS, Dzialowski I, et al. Prediction of haematoma growth and outcome in patients with intracerebral haemorrhage using the CT-angiography spot sign (PREDICT): a prospective observational study. *Lancet Neurol*. 2012;11(4):307–14.
 37. Park SY, Kong MH, Kim JH, Kang DS, Song KY, Huh SK. Role of “Spot Sign” on CT Angiography to Predict Hematoma Expansion in Spontaneous Intracerebral Hemorrhage. *J Korean Neurosurg Soc*. 2010;48(5):399.
 38. Martí-Fàbregas J, Delgado-Mederos R, Granell E, Morenas Rodríguez E, Marín Lahoz J, Dinia L, et al. Microbleed Burden and Hematoma Expansion in Acute Intracerebral Hemorrhage. *Eur Neurol*. 2013;70(3–4):175–8.
 39. Hemphill JC, Greenberg SM, Anderson CS, Becker K, Bendok BR, Cushman M, et al. Guidelines for the Management of Spontaneous Intracerebral Hemorrhage: A Guideline for Healthcare Professionals from the American Heart Association/American Stroke Association. *Stroke*. 2015;46(7):2032–60.
 40. Shoamanesh A, Catanese L, Sakai O, Pikula A, Kase CS. Diffusion-Weighted imaging hyperintensities in intracerebral hemorrhage: Microinfarcts or microbleeds? *Ann Neurol*. 2013;73(6):795–6.
 41. Kamel H, Navi BB, Hemphill JC. A Rule to Identify Patients Who Require Magnetic Resonance Imaging After Intracerebral Hemorrhage. *Neurocrit Care*. 2013;18(1):59–63.
 42. McCormack RF, Hutson A. Can Computed Tomography Angiography of the Brain Replace Lumbar Puncture in the Evaluation of Acute-onset Headache After a Negative Noncontrast Cranial Computed Tomography Scan? *Acad Emerg Med*. 2010;17(4):444–51.
 43. Ashraf R, Akhtar M, Akhtar S, Manzoor I. Diagnostic accuracy of flair in detection of acute subarachnoid hemorrhage in patients presenting with severe headache. *Journal of Neuroradiology*. 2018;
 44. Yesilaras M, Kilic TY, Yesilaras S, Atilla OD, Öncel D, Çamlar M. The diagnostic and prognostic value of the optic nerve sheath diameter on CT for diagnosis spontaneous subarachnoid hemorrhage. *Am J Emerg Med*. 2017;35(10):1408–13.
 45. van Gijn J, Kerr RS, Rinkel GJ. Subarachnoid haemorrhage. *Lancet*. 2007;369(9558):306–18.
 46. Tabatabai RR, Swadron SP. Headache in the Emergency Department: Avoiding Misdiagnosis of Dangerous Secondary Causes. *Emerg Med Clin North Am*. 2016;34(4):695–716.
 47. Rogers A, Furry J, Banks C, Chu K. Diagnosis of subarachnoid haemorrhage: A survey of Australasian emergency physicians and trainees. *Emerg Med Australas*. 2014;26(5):468–73.
 48. Swadron SP. Pitfalls in the Management of Headache in the Emergency Department. *Emerg Med Clin North Am*. 2010;28(1):127–47.
 49. Farzad A, Radin B, Oh JS, Teague HM, Euerle BD, Nable J V, et al. Emergency diagnosis of subarachnoid hemorrhage: An evidence-based debate [Internet]. Vol. 44, *Journal of Emergency Medicine*. 2013. p. 1045–53.
 50. Bonita R, Thomson S. Subarachnoid hemorrhage: Epidemiology, diagnosis, management, and outcome. *Stroke*. 1985;16(4):591–4.
 51. Byyny RL, Mower WR, Shum N, Gabayan GZ, Fang S, Baraff LJ. Sensitivity of Noncontrast Cranial Computed Tomography for the Emergency Department Diagnosis of Subarachnoid Hemorrhage. *Ann Emerg Med*. 2008;51(6):697–703.
 52. Wiesmann M, Mayer TE, Yousry I, Medele R, Hamann GF, Brückmann H. Detection of hyperacute subarachnoid hemorrhage of the brain by using magnetic resonance imaging. *J Neurosurg*. 2002;96(4):684–9.
 53. Mitchell P, Wilkinson ID, Hoggard N, Paley MN, Jellinek DA, Powell T, et al. Detection of subarachnoid haemorrhage with magnetic resonance imaging. *J Neurol Neurosurg Psychiatry*. 2001;70(2):205–11.
 54. Graff-Radford J, Fugate JE, Klaas J, Flemming KD, Brown RD, Rabinstein AA. Distinguishing clinical and radiological features of non-traumatic convexal subarachnoid hemorrhage. *Eur J Neurol*. 2016;23(5):839–46.
 55. Connolly ES, Rabinstein AA, Carhuapoma JR, Derdeyn CP, Dion J, Higashida RT, et al. Guidelines for the management of aneurysmal subarachnoid hemorrhage: A guideline for healthcare professionals from the american heart association/american stroke association [Internet]. Vol. 43, *Stroke*. 2012. p. 1711–37.
 56. Wu X, Kalra VB, Forman HP, Malhotra A. Cost-effectiveness analysis of CTA and LP for evaluation of suspected SAH after negative non-contrast CT. *Clin Neurol Neurosurg*. 2016;142:104–11.
 57. Edlow JA. What Are the Unintended Consequences of Changing the Diagnostic Paradigm for Subarachnoid Hemorrhage After Brain Computed Tomography to Computed Tomographic Angiography in Place of Lumbar Puncture? *Acad Emerg Med*. 2010;17(9):991–5.
 58. Dubosh NM, Bellolio MF, Rabinstein AA, Edlow JA. Sensitivity of Early Brain Computed Tomography to Exclude Aneurysmal Subarachnoid Hemorrhage. *Stroke*. 2016;47(3):750–5.
 59. Blok KM, Rinkel GJE, Majoie CBLM, Hendrikse J, Braaksmma M, Tijssen CC, et al. CT within 6 hours of headache onset to rule out subarachnoid hemorrhage in nonacademic hospitals. *Neurology*. 2015;84(19):1927–32.
 60. Perry JJ, Stiell IG, Sivilotti MLA, Bullard MJ, Émond M, Symington C, et al. Sensitivity of computed tomography performed within six hours of onset of headache for diagnosis of subarachnoid haemorrhage: Prospective cohort study. *BMJ*. 2011;343(7817):d4277.
 61. Carpenter CR, Hussain AM, Ward MJ, Zipfel GJ, Fowler S, Pines JM, et al. Spontaneous Subarachnoid Hemorrhage: A Systematic Review and Meta-analysis Describing the Diagnostic Accuracy of History, Physical Examination, Imaging, and Lumbar Puncture With an Exploration of Test Thresholds. *Acad Emerg Med*. 2016;23(9):963–1003.
 62. Migdal VL, Wu WK, Long D, McNaughton CD, Ward MJ, Self WH. Risk-benefit analysis of lumbar puncture to evaluate for nontraumatic subarachnoid hemorrhage in adult ED patients. *Am J Emerg Med*. 2015;33(11):1597–601.
 63. Cooper JG, Smith B, Hassan TB. A retrospective review of sudden onset severe headache and subarachnoid haemorrhage on the clinical decision unit. *Eur J Emerg Med*. 2016;23(5):356–62.
 64. Mark DG, Hung Y-Y, Offerman SR, Rauchwerger AS, Reed ME, Chettipally U, et al. Nontraumatic Subarachnoid Hemorrhage in the Setting of Negative Cranial Computed

- Tomography Results: External Validation of a Clinical and Imaging Prediction Rule. *Ann Emerg Med*. 2013;62(1):1–10.e1.
65. Mortimer AM, Bradley MD, Stoodley NG, Renowden SA. Thunderclap headache: Diagnostic considerations and neuroimaging features [Internet]. Vol. 68, *Clinical Radiology*. W.B. Saunders; 2013. p. e101–13.
 66. Al-Mufti F, Mayer SA. Neurocritical Care of Acute Subdural Hemorrhage. *Neurosurg Clin N Am*. 2017;28(2):267–78.
 67. Vega RA, Valadka AB. Natural History of Acute Subdural Hematoma. *Neurosurg Clin N Am*. 2017;28(2):247–55.
 68. Avis SP. Nontraumatic Acute Subdural Hematoma: A Case Report and Review of the Literature. *Am J Forensic Med Pathol*. 1993;14(2):130–4.
 69. Carroll JJ, Lavine SD, Meyers PM. Imaging of Subdural Hematomas. *Neurosurg Clin N Am*. 2017;28(2):179–203.
 70. Gentry LR, Godersky JC, Thompson B, Dunn VD. Prospective comparative study of intermediate-field MR and CT in the evaluation of closed head trauma. *AJR Am J Roentgenol*. 1988;150(3):673–82.
 71. Thapa A, KC B, Shakya B. Pure Acute-on-Chronic Subdural Hematoma Due to Ruptured Posterior Communicating Artery Aneurysm: Unsuspecting Entity. *World Neurosurg*. 2018;114:335–8.
 72. Verhey LH, Wang W, Adel JG. True Cortical Saccular Aneurysm Presenting as an Acute Subdural Hematoma. *World Neurosurg*. 2018;113:58–61.
 73. Mathais Q, Esnault P, Dagain A, Sellier A, Simon PY, Prunet B, et al. Spontaneous pure subacute subdural haematoma without subarachnoid haemorrhage caused by rupture of middle cerebral artery aneurysm. *Anaesth Crit Care Pain Med*. 2018;37(6):623–4.
 74. Koerbel A, Ernemann U, Freudenstein D. Acute subdural haematoma without subarachnoid haemorrhage caused by rupture of an internal carotid artery bifurcation aneurysm: Case report and review of literature. *Br J Radiol*. 2005;78(931):646–50.
 75. Awaji K, Inokuchi R, Ikeda R, Haisa T. Nontraumatic Pure Acute Subdural Hematoma Caused by a Ruptured Cortical Middle Cerebral Artery Aneurysm: Case Report and Literature Review [Internet]. Vol. 3, *NMC Case Report Journal*. 2016. p. 63–6.
 76. Inokuchi G, Makino Y, Yajima D, Motomura A, Chiba E, Torimitsu S, et al. A case of acute subdural hematoma due to ruptured aneurysm detected by postmortem angiography. *Int J Legal Med*. 2016;130(2):441–6.
 77. Brisman JL, Song JK, Newell DW. Cerebral Aneurysms. *N Engl J Med*. 2006;355(9):928–39.
 78. Brown RD, Broderick JP. Unruptured intracranial aneurysms: epidemiology, natural history, management options, and familial screening. *Lancet Neurol*. 2014;13(4):393–404.
 79. Schwartz RB, Tice HM, Hooten SM, Hsu L, Stieg PE. Evaluation of cerebral aneurysms with helical CT: correlation with conventional angiography and MR angiography. *Radiology*. 1994;192(3):717–22.
 80. Hacin-Bey L, Provenzale JM. Current imaging assessment and treatment of intracranial aneurysms. *Am J Roentgenol*. 2011;196:32–44.
 81. Pradilla G, Wicks RT, Hadelsberg U, Gailloud P, Coon AL, Huang J, et al. Accuracy of computed tomography angiography in the diagnosis of intracranial aneurysms. *World Neurosurg*. 2013;80(6):845–52.
 82. Li M-H, Li Y-D, Tan H-Q, Gu B-X, Chen Y-C, Wang W, et al. Contrast-free MRA at 3.0 T for the detection of intracranial aneurysms. *Neurology*. 2011;77(7):667–76.
 83. Sailer AMH, Wagemans BAJM, Nelemans PJ, De Graaf R, Van Zwam WH. Diagnosing intracranial aneurysms with mr angiography : Systematic review and meta-analysis. *Stroke*. 2014;45(1):119–26.
 84. Stafa A, Leonardi M. Role of Neuroradiology in Evaluating Cerebral Aneurysms. *Interv Neuroradiol*. 2008;14:23–37.
 85. Dalton A, Dobson G, Prasad M, Mukerji N. De novo intracerebral arteriovenous malformations and a review of the theories of their formation. *Br J Neurosurg*. 2018;32(3):305–11.
 86. Mohr JP, Kejda-Scharler J, Pile-Spellman J. Diagnosis and treatment of arteriovenous malformations topical collection on stroke. *Curr Neurol Neurosci Rep*. 2013;13(2):324.
 87. Lang S-S, Beslow LA, Bailey RL, Vossough A, Ekstrom J, Heuer GG, et al. Follow-up imaging to detect recurrence of surgically treated pediatric arteriovenous malformations. *J Neurosurg Pediatr*. 2012;9(5):497–504.
 88. Saleh RS, Singhal A, Lohan D, Duckwiler G, Finn P, Ruehm S. Assessment of cerebral arteriovenous malformations with high temporal and spatial resolution contrast-enhanced magnetic resonance angiography: A review from protocol to clinical application [Internet]. Vol. 19, *Topics in Magnetic Resonance Imaging*. 2008. p. 251–7.
 89. Serulle Y, Miller TR, Gandhi D. Dural Arteriovenous Fistulae: Imaging and Management [Internet]. Vol. 26, *Neuroimaging Clinics of North America*. 2016. p. 247–58.
 90. Elhammady MS, Ambekar S, Heros RC. Epidemiology, clinical presentation, diagnostic evaluation, and prognosis of cerebral dural arteriovenous fistulas. In: *Handbook of Clinical Neurology*. 2017. p. 99–105.
 91. Srinivasan VM, Chintalapani G, Duckworth EAM, Kan P. Application of 4-Dimensional Digital Subtraction Angiography for Dural Arteriovenous Fistulas. *World Neurosurg*. 2016;96:24–30.
 92. Tsai L-K, Liu H-M, Jeng J-S. Diagnosis and management of intracranial dural arteriovenous fistulas. *Expert Rev Neurother*. 2016;16(3):307–18.
 93. Naserrudin NS, Mohammad Raffiq MA. Dural arteriovenous fistula mimicking temporal arteritis. *Clin Neurol Neurosurg*. 2019;176:44–6.
 94. Stapleton CJ, Barker FG. Cranial Cavernous Malformations. *Stroke*. 2018;49(4):1029–35.
 95. Daniele Rigamonti, M.D., Mark N. Hadley, M.D., Burton P. Drayer, M.D., Peter C. Johnson, M.D., M.A., Karen Hoenig-Rigamonti, M.D., J. Thomas Knight, M.D., and Robert F. Spetzler MD. Cerebral cavernous malformations. *N Engl J Med*. 1998;319(6):343–7.
 96. Comi AM. Sturge-Weber syndrome. *Handb Clin Neurol*. 2015;132:157–68.
 97. Higueros E, Roe E, Granell E, Baselga E. Síndrome de Sturge-Weber: revisión [Internet]. Vol. 108, *Actas Dermo-Sifilograficas*. Elsevier; 2017. p. 407–17.
 98. Sudarsanam A, Ardern-Holmes SL. Sturge-Weber syndrome: From the past to the present [Internet]. Vol. 18, *European Journal of Paediatric Neurology*. W.B. Saunders; 2014. p. 257–66.

99. Pinto AL, Chen L, Friedman R, Grant PE, Poduri A, Takeoka M, et al. Sturge-Weber Syndrome: Brain Magnetic Resonance Imaging and Neuropathology Findings. *Pediatr Neurol*. 2016;58:25–30.
100. Koster MJ, Matteson EL, Warrington KJ. Large-vessel giant cell arteritis: Diagnosis, monitoring and management [Internet]. Vol. 57, *Rheumatology (United Kingdom)*. 2018. p. ii32–ii42.
101. Christoph BT, Gregor S, Markus A, Daniel S, Christof R, Thomas D. The clinical benefit of imaging in the diagnosis and treatment of giant cell arteritis [Internet]. Vol. 148, *Swiss Medical Weekly*. EMH Media; 2018.
102. Nesher G. The diagnosis and classification of giant cell arteritis. *J Autoimmun*. 2014;48–49:73–5.
103. Hyeon Jeong Cho, MS, Justin Bloomberg, DO, Jeffrey Nichols M. Giant Cell Arteritis. *Disease-a-month*. 2017;367–87.
104. Buttgerief F, Dejaco C, Matteson EL, Dasgupta B. Polymyalgia Rheumatica and Giant Cell Arteritis. *JAMA*. 2016;315(22):2442–58.
105. Jem Ninan, Susan Lester CH. Giant Cell Arteritis. *Best Pract Res Clin Rheumatol*. 2016;367–87.
106. Frohman L, Wong ABC, Matheos K, Leon-Alvarado LG, Danesh-Meyer H V. New developments in giant cell arteritis. *Surv Ophthalmol*. 2016;61(4):400–21.
107. Mandal J, Chung SA. Primary Angiitis of the Central Nervous System [Internet]. Vol. 43, *Rheumatic Disease Clinics of North America*. Elsevier; 2017. p. 503–18.
108. Salvarani C, Brown RD, Calamia KT, Christianson TJH, Weigand SD, Miller D V, et al. Primary central nervous system vasculitis: analysis of 101 patients. *Ann Neurol*. 2007;62(5):442–51.
109. Rodriguez-Pla A, Monach PA. Primary Angiitis of the Central Nervous System in Adults and Children. *Rheum Dis Clin North Am*. 2015;41(1):47–62.
110. Hajj-Ali RA, Calabrese LH. Primary angiitis of the central nervous system. *Autoimmun Rev*. 2013;12(4):463–6.
111. Boulouis G, De Boysson H, Zuber M, Guillemin L, Meary E, Costalat V, et al. Primary Angiitis of the Central Nervous System: Magnetic Resonance Imaging Spectrum of Parenchymal, Meningeal, and Vascular Lesions at Baseline. *Stroke*. 2017;48(5):1248–55.
112. Singhal AB, Topcuoglu MA, Fok JW, Kursun O, Nogueira RG, Frosch MP, et al. Reversible cerebral vasoconstriction syndromes and primary angiitis of the central nervous system: clinical, imaging, and angiographic comparison. *Ann Neurol*. 2016;79(6):882–94.
113. Gan C, Maingard J, Giles L, Phal PM, Tan KM. Primary angiitis of the central nervous system presenting as a mass lesion. *J Clin Neurosci*. 2015;22(9):1528–31.
114. Engelter ST, Traenka C, Von Hessling A, Lyrer PA. Diagnosis and treatment of cervical artery dissection. *Neurol Clin*. 2015;33(2):421–41.
115. Kim Y-K, Schulman S. Cervical artery dissection: Pathology, epidemiology and management. *Thromb Res*. 2009;123(6):810–21.
116. Robertson JJ, Koefman A. Cervical Artery Dissections: A Review. *J Emerg Med*. 2016;51(5):508–18.
117. Mattioni A, Paciaroni M, Sarchielli P, Murasecco D, Pelliccioli GP, Calabresi P. Multiple cranial nerve palsies in a patient with internal carotid artery dissection. *Eur Neurol*. 2007;58(2):125–7.
118. Dittrich R, Ritter MA, Ringelstein EB. Ultrasound in spontaneous cervical artery dissection. *Perspect Med*. 2012;1–12:250–4.
119. Kim YK, Schulman S. Cervical artery dissection: Pathology, epidemiology and management [Internet]. Vol. 123, *Thrombosis Research*. Pergamon; 2009. p. 810–21.
120. Debette S, Leys D. Cervical-artery dissections: pre-disposing factors, diagnosis, and outcome. *Lancet Neurol*. 2009;8(7):668–78.
121. Provenzale JM, Sarikaya B. Comparison of test performance characteristics of MRI, MR angiography, and CT angiography in the diagnosis of carotid and vertebral artery dissection: A review of the medical literature [Internet]. Vol. 193, *American Journal of Roentgenology*. 2009. p. 1167–74.
122. Hanning U, Sporns PB, Schmiedel M, Ringelstein EB, Heindel W, Wiendl H, et al. CT versus MR Techniques in the Detection of Cervical Artery Dissection. *J Neuroimaging*. 2017;27(6):607–12.
123. Thomas MA, Pearce WH, Rodriguez HE, Helenowski IB, Eskandari MK. Durability of Stroke Prevention with Carotid Endarterectomy and Carotid Stenting. *Surgery*. 2018;164(6):1271–8.
124. Galyfos G, Sianou A, Filis K. Cerebral hyperperfusion syndrome and intracranial hemorrhage after carotid endarterectomy or carotid stenting: A meta-analysis. *J Neurol Sci*. 2017;381:74–82.
125. Kirchoff-Torres KF, Bakradze E. Cerebral Hyperperfusion Syndrome After Carotid Revascularization and Acute Ischemic Stroke. *Curr Pain Headache Rep*. 2018;22(4):24.
126. Doepp F, Kebelmann-Betz C, Kivi A, Schreiber SJ. Stenosis or Hyperperfusion in Sickle Cell Disease - Ultrasound Assessment of Cerebral Blood Flow Volume. *Ultrasound Med Biol*. 2012;38(8):1333–8.
127. Van Mook WNKA, Rennenberg RJMW, Schurink GW, Van Oostenbrugge RJ, Mess WH, Hofman PAM, et al. Cerebral hyperperfusion syndrome. *Lancet Neurol*. 2005;4(12):877–88.
128. Zhang Y, Kumar A, Tezel JB, Zhou Y. Imaging Evidence for Cerebral Hyperperfusion Syndrome after Intravenous Tissue Plasminogen Activator for Acute Ischemic Stroke. *Case Rep Neurol Med*. 2016;2016:1–5.
129. Yoo DH, Roh HG, Choi SS, Moon J, Lee J, Cho YD, et al. Staged carotid artery stenting in patients with severe carotid stenosis: Multicenter experience. *J Clin Neurosci*. 2018;53:74–8.
130. Ferro JM, Canhão P, Stam J, Boussier MG, Barinagarrementeria F. Prognosis of Cerebral Vein and Dural Sinus Thrombosis: Results of the International Study on Cerebral Vein and Dural Sinus Thrombosis (ISCVT). *Stroke*. 2004;35(3):664–70.
131. Coutinho JM, Zuurbier SM, Aramideh M, Stam J. The incidence of cerebral venous thrombosis: A cross-sectional study. *Stroke*. 2012;43(12):3375–7.
132. Coutinho JM. Cerebral venous thrombosis. *J Thromb Haemost*. 2015;13:S238–44.
133. Rizzo L, Crasto SG, Rudà R, Gallo G, Tola E, Garaballo D, et al. Cerebral venous thrombosis: role of CT, MRI and MRA in the emergency setting. *Radiol Med*. 2010;115(2):313–25.
134. Saposnik G, Barinagarrementeria F, Brown RD, Bushnell CD, Cucchiara B, Cushman M, et al. Diagnosis and manage-

- ment of cerebral venous thrombosis: A statement for healthcare professionals from the American Heart Association/American Stroke Association. *Stroke*. 2011;42(4):1158–92.
135. Rodallec MH, Krainik A, Feydy A, Hélias A, Colombani J-M, Jullès M-C, et al. Cerebral Venous Thrombosis and Multidetector CT Angiography: Tips and Tricks. *RadioGraphics*. 2006;26(suppl_1):S5–18.
 136. Buyck P-J, De Keyser F, Vanneste D, Wilms G, Thijs V, De-maerel P. CT Density Measurement and H:H Ratio Are Useful in Diagnosing Acute Cerebral Venous Sinus Thrombosis. *Am J Neuroradiol*. 2013;34(8):1568–72.
 137. Goldberg AL, Rosenbaum AE, Wang H, Kim WS, Lewis VL, Hanley DF. Computed tomography of dural sinus thrombosis. *J Comput Assist Tomogr*. 1986;10(1):16–20.
 138. Long B, Koyfman A, Runyon MS. Cerebral Venous Thrombosis: A Challenging Neurologic Diagnosis. *Emerg Med Clin North Am*. 2017;35(4):869–78.
 139. Leach JL, Fortuna RB, Jones B V., Gaskill-Shipley MF. Imaging of Cerebral Venous Thrombosis: Current Techniques, Spectrum of Findings, and Diagnostic Pitfalls. *RadioGraphics*. 2006;26(suppl_1):S19–41.
 140. Gratama van Andel HA, van Boven LJ, van Walderveen MA, Venema HW, van Rijn JC, Stam J, et al. Interobserver variability in the detection of cerebral venous thrombosis using CT venography with matched mask bone elimination. *Clin Neurol Neurosurg*. 2009;111(9):717–23.
 141. Ozsvath RR, Casey SO, Lustrin ES, Alberico RA, Hassankhani A, Patel M. Cerebral Venography: Comparison of CT and MR Projection Venography. *Am J Roentgenol*. 1997;169(6):1699–707.
 142. Ayanzen RH, Bird CR, Keller PJ, McCully FJ, Theobald MR, Heiserman JE. Cerebral MR venography: Normal anatomy and potential diagnostic pitfalls. *Am J Neuroradiol*. 2000;21(1):74–8.
 143. Boukobza M, Crassard I, Bousser MG, Chabriat H. MR imaging features of isolated cortical vein thrombosis: Diagnosis and follow-up. *Am J Neuroradiol*. 2009;30(2):344–8.
 144. Farb RI, Scott JN, Willinsky RA, Montanera WJ, Wright GA, TerBrugge KG. Intracranial Venous System: Gadolinium-enhanced Three-dimensional MR Venography with Auto-triggered Elliptic Centric-ordered Sequence—Initial Experience. *Radiology*. 2003;226(1):203–9.
 145. Silvis SM, de Sousa DA, Ferro JM, Coutinho JM. Cerebral venous thrombosis. *Nat Rev Neurol*. 2017;13(9):555–65.
 146. Dinkin MJ, Patsalides A. Venous Sinus Stenting for Idiopathic Intracranial Hypertension: Where Are We Now? *Neurol Clin*. 2017;35(1):59–81.
 147. Ducros A. Reversible cerebral vasoconstriction syndrome. *Lancet Neurol*. 2012;11(10):906–17.
 148. Ducros A, Wolff V. The Typical Thunderclap Headache of Reversible Cerebral Vasoconstriction Syndrome and its Various Triggers. *Headache J Head Face Pain*. 2016;56(4):657–73.
 149. Ducros A, Boukobza M, Porcher R, Sarov M, Valade D, Bousser M-G. The clinical and radiological spectrum of reversible cerebral vasoconstriction syndrome. A prospective series of 67 patients. *Brain*. 2007;130(12):3091–101.
 150. Singhal AB, Hajj-Ali RA, Topcuoglu MA, Fok J, Bena J, Yang D, et al. Reversible Cerebral Vasoconstriction Syndromes. *Arch Neurol*. 2011;68(8):1005–12.
 151. Wolff V, Ducros A. Reversible Cerebral Vasoconstriction Syndrome Without Typical Thunderclap Headache. *Headache J Head Face Pain*. 2016;56(4):674–87.
 152. Wolff V, Armspach J-P, Lauer V, Rouyer O, Ducros A, Marescaux C, et al. Ischaemic Strokes with Reversible Vasoconstriction and without Thunderclap Headache: A Variant of the Reversible Cerebral Vasoconstriction Syndrome? *Cerebrovasc Dis*. 2015;39(1):31–8.
 153. Katz BS, Fugate JE, Ameriso SF, Pujol-Lereis VA, Mandrekar J, Flemming KD, et al. Clinical Worsening in Reversible Cerebral Vasoconstriction Syndrome. *JAMA Neurol*. 2014;71(1):68–73.
 154. Marder CP, Donohue MM, Weinstein JR, Fink KR. Multimodal imaging of reversible cerebral vasoconstriction syndrome: A series of 6 cases. *Am J Neuroradiol*. 2012;33(7):1403–10.
 155. Miller TR, Shivashankar R, Mossa-Basha M, Gandhi D. Reversible Cerebral Vasoconstriction Syndrome, Part 2: Diagnostic Work-Up, Imaging Evaluation, and Differential Diagnosis. *Am J Neuroradiol*. 2015;36(9):1580–8.
 156. Kumar S, Goddeau RP, Selim DMH, Thomas PA, Schlaug G, Alhazzani PA, et al. Atraumatic convexal subarachnoid hemorrhage Clinical presentation, imaging patterns, and etiologies. *Neurology*. 2010;74(11):893–9.
 157. Lin C-H, Chen Y-Y, Chiu L-A, Lee K-W. Dual energy computed tomography angiography for the rapid diagnosis of reversible cerebral vasoconstriction syndromes: report of a case. *Acta Neurol Taiwan*. 2013;22(1):36–42.
 158. Kameda T, Namekawa M, Shimazaki H, Minakata D, Matsura T, Nakano I. Unique combination of hyperintense vessel sign on initial FLAIR and delayed vasoconstriction on MRA in reversible cerebral vasoconstriction syndrome: A case report. *Cephalalgia*. 2014;34(13):1093–6.
 159. Chen S-P, Fuh J-L, Lirng J-F, Wang S-J. Hyperintense vessels on flair imaging in reversible cerebral vasoconstriction syndrome. *Cephalalgia*. 2012;32(4):271–8.
 160. Chen S-P, Fuh J-L, Wang S-J, Chang F-C, Lirng J-F, Fang Y-C, et al. Magnetic resonance angiography in reversible cerebral vasoconstriction syndromes. *Ann Neurol*. 2010;67(5):648–56.
 161. Chen S-P, Fuh J-L, Chang F-C, Lirng J-F, Shia B-C, Wang S-J. Transcranial color doppler study for reversible cerebral vasoconstriction syndromes. *Ann Neurol*. 2008;63(6):751–7.
 162. Ducros A, Bousser M-G. Reversible cerebral vasoconstriction syndrome. *Pract Neurol*. 2009;9(5):256–67.
 163. Mandell DM, Matouk CC, Farb RI, Krings T, Agid R, terBrugge K, et al. Vessel Wall MRI to Differentiate Between Reversible Cerebral Vasoconstriction Syndrome and Central Nervous System Vasculitis. *Stroke*. 2012;43(3):860–2.
 164. Obusez EC, Hui F, Hajj-ali RA, Cerejo R, Calabrese LH, Hammad T, et al. High-Resolution MRI Vessel Wall Imaging: Spatial and Temporal Patterns of Reversible Cerebral Vasoconstriction Syndrome and Central Nervous System Vasculitis. *Am J Neuroradiol*. 2014;35(8):1527–32.
 165. Komatsu T, Kimura T, Yagishita A, Takahashi K, Koide R. A case of reversible cerebral vasoconstriction syndrome presenting with recurrent neurological deficits: Evaluation using noninvasive arterial spin labeling MRI. *Clin Neurol Neurosurg*. 2014;126:96–8.
 166. Rosenbloom MH, Singhal AB. CT Angiography and Diffusion-Perfusion MR Imaging in a Patient with Ipsilateral Reversible Cerebral Vasoconstriction after Carotid Endarterectomy. *Am J Neuroradiol*. 2007;28(5):920–2.

167. Zhao WY, Krings T, Alvarez H, Ozanne A, Holmin S, Lasjaunias P. Management of spontaneous haemorrhagic intracranial vertebrobasilar dissection: review of 21 consecutive cases. *Acta Neurochir (Wien)*. 2007;149(6):585–96; discussion 596.
168. Santos-Franco JA, Zenteno M, Lee A. Dissecting aneurysms of the vertebrobasilar system. A comprehensive review on natural history and treatment options. *Neurosurg Rev*. 2008;31(2):131–40.
169. Metso A, Metso T, Salonen O, Tatlisumak T. Response to Letter by Arnold et al. *Stroke*. 2007;38(11):141.
170. Debette S, Compter A, Labeyrie M-A, Uyttenboogaart M, Metso TM, Majersik JJ, et al. Epidemiology, pathophysiology, diagnosis, and management of intracranial artery dissection. *Lancet Neurol*. 2015;14(6):640–54.
171. Wang Y, Lou X, Li Y, Sui B, Sun S, Li C, et al. Imaging investigation of intracranial arterial dissecting aneurysms by using 3 T high-resolution MRI and DSA: from the interventional neuroradiologists' view. *Acta Neurochir (Wien)*. 2014;156(3):515–25.
172. Mizutani T. Natural course of intracranial arterial dissections. *J Neurosurg*. 2011;114(4):1037–44.
173. Ahn SS, Kim BM, Suh SH, Kim DJ, Kim DI, Shin YS, et al. Spontaneous Symptomatic Intracranial Vertebrobasilar Dissection: Initial and Follow-up Imaging Findings. *Radiology*. 2012;264(1):196–202.
174. Kilarski LL, Rutten-Jacobs LCA, Bevan S, Baker R, Hassan A, Hughes DA, et al. Prevalence of CADASIL and fabry disease in a cohort of MRI defined younger onset Lacunar Stroke. *Kaya N*, editor. *PLoS One*. 2015;10(8):e0136352.
175. Moreton FC, Razvi SSM, Davidson R, Muir KW. Changing clinical patterns and increasing prevalence in CADASIL. *Acta Neurol Scand*. 2014;130(3):197–203.
176. Razvi SSM, Davidson R, Bone I, Muir K. The prevalence of cerebral autosomal dominant arteriopathy with subcortical infarcts and leukoencephalopathy (CADASIL) in the west of Scotland. *J Neurol Neurosurg Psychiatry*. 2005;76(5):739–41.
177. Narayan SK, Gorman G, Kalaria RN, Ford GA, Chinnery PF. The minimum prevalence of CADASIL in northeast England. *Neurology*. 2012;78(13):1025–7.
178. Kilarski LL, Rutten-Jacobs LCA, Bevan S, Baker R, Hassan A, Hughes DA, et al. Prevalence of CADASIL and fabry disease in a cohort of MRI defined younger onset Lacunar Stroke. *Kaya N*, editor. *PLoS One*. 2015;10(8):e0136352.
179. Chabriat H, Joutel A, Dichgans M, Tournier-Lasserre E, Boussier M-G. CADASIL. *Lancet Neurol*. 2009;8(7):643–53.
180. Stromillo ML, Dotti MT, Battaglini M, Mortilla M, Bianchi S, Plewnia K, et al. Structural and metabolic brain abnormalities in preclinical cerebral autosomal dominant arteriopathy with subcortical infarcts and leukoencephalopathy. *J Neurol Neurosurg Psychiatry*. 2009;80(1):41–7.
181. Zhu S, Nahas SJ. CADASIL: Imaging Characteristics and Clinical Correlation. *Curr Pain Headache Rep*. 2016;20(10):57.
182. Auer DP, Pütz B, Gössel C, Elbel G-K, Gasser T, Dichgans M. Differential Lesion Patterns in CADASIL and Sporadic Subcortical Arteriosclerotic Encephalopathy: MR Imaging Study with Statistical Parametric Group Comparison. *Radiology*. 2001;218(2):443–51.
183. Di Donato I, Bianchi S, De Stefano N, Dichgans M, Dotti MT, Düring M, et al. Cerebral Autosomal Dominant Arteriopathy with Subcortical Infarcts and Leukoencephalopathy (CADASIL) as a model of small vessel disease: update on clinical, diagnostic, and management aspects. *BMC Med*. 2017;15(1):41.
184. Singhal S, Rich P, Markus HS. The spatial distribution of MR imaging abnormalities in cerebral autosomal dominant arteriopathy with subcortical infarcts and leukoencephalopathy and their relationship to age and clinical features. *Am J Neuroradiol*. 2005;26(10):2481–7.
185. Coulthard A, Blank SC, Bushby K, Kalaria RN, Burn DJ. Distribution of cranial MRI abnormalities in patients with symptomatic and subclinical CADASIL. *Br J Radiol*. 2000;73(867):256–65.
186. Pavlakis SG, Phillips PC, DiMauro S, De Vivo DC, Rowland LP. Mitochondrial myopathy, encephalopathy, lactic acidosis, and stroke-like episodes: A distinctive clinical syndrome. *Ann Neurol*. 1984;16(4):481–8.
187. Hirano M, Ricci E, Koenigsberger MR, Defendini R, Pavlakis SG, DeVivo DC, et al. Melas: an original case and clinical criteria for diagnosis. *Neuromuscul Disord*. 1992;2(2):125–35.
188. Malhotra K, Liebeskind DS. Imaging of MELAS. *Curr Pain Headache Rep*. 2016;20(9):54.
189. Ito H, Mori K, Kagami S. Neuroimaging of stroke-like episodes in MELAS. *Brain Dev*. 2011;33(4):283–8.
190. Walecka A. CT and MRI imaging of the brain in MELAS syndrome. *Polish J Radiol*. 2013;78(3):61–5.
191. Pauli W, Zarzycki A, Krzyształowski A, Walecka A. CT and MRI imaging of the brain in MELAS syndrome. *Polish J Radiol*. 2013;78(3):61–5.
192. Kim IO, Kim JH, Kim WS, Hwang YS, Yeon KM, Han MC. Mitochondrial myopathy-encephalopathy-lactic acidosis-and stroke-like episodes (MELAS) syndrome: CT and MR findings in seven children. *AJR Am J Roentgenol*. 1996;166(3):641–5.
193. Schaefer PW, Buonanno FS, Gonzalez RG, Schwamm LH. Diffusion-weighted imaging discriminates between cytotoxic and vasogenic edema in a patient with eclampsia. *Stroke*. 1997;28(5):1082–5.
194. Kim JH, Lim MK, Jeon TY, Rha JH, Eo H, Yoo SY, et al. Diffusion and perfusion characteristics of MELAS (mitochondrial myopathy, encephalopathy, lactic acidosis, and stroke-like episode) in thirteen patients. *Korean J Radiol*. 2011;12(1):15–24.
195. Yonemura K, Hasegawa Y, Kimura K, Minematsu K, Yamaguchi T. Diffusion-weighted MR imaging in a case of mitochondrial myopathy, encephalopathy, lactic acidosis, and stroke-like episodes. *AJNR Am J Neuroradiol*. 2001;22(2):269–72.
196. Abe K, Yoshimura H, Tanaka H, Fujita N, Hikita T, Sakoda S. Comparison of conventional and diffusion-weighted MRI and proton MR spectroscopy in patients with mitochondrial encephalomyopathy, lactic acidosis, and stroke-like events. *Neuroradiology*. 2004;46(2):113–7.
197. Ito H, Mori K, Harada M, Minato M, Naito E, Takeuchi M, et al. Serial brain imaging analysis of stroke-like episodes in MELAS. *Brain Dev*. 2008;30(7):483–8.
198. Tzoulis C, Bindoff LA. Serial Diffusion Imaging in a Case of Mitochondrial Encephalomyopathy, Lactic Acidosis, and Stroke-Like Episodes. *Stroke*. 2009;40(2):e15–7.
199. Koga Y, Akita Y, Nishioka J, Yatsuga S, Povalko N, Tanabe Y, et al. L-Arginine improves the symptoms of stroke-like epi-

- sodes in MELAS. *Neurology*. 2005;64(4):710–2.
200. Nishioka J, Akita Y, Yatsuga S, Katayama K, Matsuishi T, Ishibashi M, et al. Inappropriate intracranial hemodynamics in the natural course of MELAS. *Brain Dev*. 2008;30(2):100–5.
201. Yeh H-L, Chen Y-K, Chen W-H, Wang H-C, Chiu H-C, Lien L-M, et al. Perfusion status of the stroke-like lesion at the hyperacute stage in MELAS. *Brain Dev*. 2013;35(2):158–64.
202. Ikawa M, Okazawa H, Arakawa K, Kudo T, Kimura H, Fujibayashi Y, et al. PET imaging of redox and energy states in stroke-like episodes of MELAS. *Mitochondrion*. 2009;9(2):144–8.
203. Ikawa M, Yoneda M, Muramatsu T, Matsunaga A, Tsujikawa T, Yamamoto T, et al. Detection of preclinically latent hyperperfusion due to stroke-like episodes by arterial spin-labeling perfusion MRI in MELAS patients. *Mitochondrion*. 2013;13(6):676–80.
204. Xie S. MR OEF Imaging in MELAS. *Methods Enzymol*. 2014;547:433–44.
205. Kamada K, Takeuchi F, Houkin K, Kitagawa M, Kuriaki S, Ogata A, et al. Reversible brain dysfunction in MELAS: MEG, and (1)H MRS analysis. *J Neurol Neurosurg Psychiatry*. 2001;70(5):675–8.
206. Kodaka R, Itagaki Y, Matsumoto M, Nagai T, Okada S. A transcranial doppler ultrasonography study of cerebrovascular CO₂ reactivity in mitochondrial encephalomyopathy. *Stroke*. 1996;27(8):1350–3.
207. Suzuki J, Kodama N. Moyamoya disease--a review. *Stroke*. 1983;14(1):104–9.
208. Baba T, Houkin K, Kuroda S. Novel epidemiological features of moyamoya disease. *J Neurol Neurosurg Psychiatry*. 2008;79(8):900–4.
209. Xie A, Luo L, Ding Y, Li G. Ischemic and hemorrhagic moyamoya disease in adults: CT findings. *Int J Clin Exp Med*. 2015;8(11):21351–7.
210. Takahashi M, Miyauchi T, Kowada M. Computed tomography of Moyamoya disease: demonstration of occluded arteries and collateral vessels as important diagnostic signs. *Radiology*. 1980;134(3):671–6.
211. Kim J-M, Lee S-H, Roh J-K. Changing ischaemic lesion patterns in adult moyamoya disease. *J Neurol Neurosurg Psychiatry*. 2009;80(1):36–40.
212. Fujimura M, Bang OY, Kim JS. Moyamoya disease. *Front Neurol Neurosci*. 2016;40:204–20.
213. Yamada I, Matsushima Y, Suzuki S. Moyamoya disease: diagnosis with three-dimensional time-of-flight MR angiography. *Radiology*. 1992;184(3):773–8.
214. Brady AP, Stack JP, Ennis JT. Moyamoya disease--imaging with magnetic resonance. *Clin Radiol*. 1990;42(2):138–41.
215. Yamada I, Suzuki S, Matsushima Y. Moyamoya disease: comparison of assessment with MR angiography and MR imaging versus conventional angiography. *Radiology*. 1995;196(1):211–8.
216. Ohta T, Tanaka H, Kuroiwa T. Diffuse leptomeningeal enhancement, "ivy sign," in magnetic resonance images of moyamoya disease in childhood: case report. *Neurosurgery*. 1995;37(5):1009–12.
217. Le-Bao Yu L-B, Zhang Q, Shi Z-Y, Wang M-Q, Zhang D. High-resolution Magnetic Resonance Imaging of Moyamoya Disease. *Chin Med J (Engl)*. 2015;128(23):3231.
218. Yuan M, Liu Z, Wang Z, Li B, Xu L, Xiao X. High-resolution MR imaging of the arterial wall in moyamoya disease. *Neurosci Lett*. 2015;584:77–82.
219. Ryoo S, Cha J, Kim SJ, Choi JW, Ki C-S, Kim KH, et al. High-Resolution Magnetic Resonance Wall Imaging Findings of Moyamoya Disease. *Stroke*. 2014;45(8):2457–60.
220. Kim YJ, Lee DH, Kwon JY, Kang DW, Suh DC, Kim JS, et al. High resolution MRI difference between moyamoya disease and intracranial atherosclerosis. *Eur J Neurol*. 2013;20(9):1311–8.
221. Rafay MF, Armstrong D, Dirks P, MacGregor DL, deVeber G. Patterns of cerebral ischemia in children with moyamoya. *Pediatr Neurol*. 2015;52(1):65–72.
222. Kuroda S, Kashiwazaki D, Ishikawa T, Nakayama N, Houkin K. Incidence, Locations, and Longitudinal Course of Silent Microbleeds in Moyamoya Disease. *Stroke*. 2013;44(2):516–8.
223. Kikuta K, Takagi Y, Nozaki K, Sawamoto N, Fukuyama H, Hashimoto N. The presence of multiple microbleeds as a predictor of subsequent cerebral hemorrhage in patients with moyamoya disease. *Neurosurgery*. 2008;62(1):104–11.
224. Suzuki J, Takaku A. Cerebrovascular “Moyamoya” Disease. *Arch Neurol*. 1969;20(3):288.
225. Sasagawa A, Mikami T, Hirano T, Akiyama Y, Mikuni N. Characteristics of cerebral hemodynamics assessed by CT perfusion in moyamoya disease. *J Clin Neurosci*. 2018;47:183–9.
226. Toscano M, Puledda F, Viganò A, Vicenzini E, Guidetti G, Lenzi GL, et al. Hemodynamic features of non-aneurysmal subarachnoid hemorrhage in a case of familial moyamoya disease: a transcranial Doppler ultrasound study. *Eur Neurol*. 2014;72(5–6):330–2.
227. Lee W-J, Jung K-H, Lee K-J, Kim J-M, Lee S-T, Chu K, et al. Sonographic findings associated with stenosis progression and vascular complications in moyamoya disease. *J Neurosurg*. 2016;125(3):689–97.
228. Hara S, Tanaka Y, Ueda Y, Hayashi S, Inaji M, Ishiwata K, et al. Noninvasive Evaluation of CBF and Perfusion Delay of Moyamoya Disease Using Arterial Spin-Labeling MRI with Multiple Postlabeling Delays: Comparison with ¹⁵O-Gas PET and DSC-MRI. *Am J Neuroradiol*. 2017;38(4):696–702.
229. Kuhn FP, Warnock G, Schweingruber T, Sommerauer M, Buck A, Khan N. Quantitative H₂[15O]-PET in Pediatric Moyamoya Disease: Evaluating Perfusion before and after Cerebral Revascularization. *J Stroke Cerebrovasc Dis*. 2015;24(5):965–71.
230. Lee M, Zaharchuk G, Guzman R, Achrol A, Bell-Stephens T, Steinberg GK. Quantitative hemodynamic studies in moyamoya disease. *Neurosurg Focus*. 2009;26(4):E5.
231. Pantoni L. Cerebral small vessel disease: from pathogenesis and clinical characteristics to therapeutic challenges. *Lancet Neurol*. 2010;9(7):689–701.
232. Keage HA, Carare RO, Friedland RP, Ince PG, Love S, Nicoll JA, et al. Population studies of sporadic cerebral amyloid angiopathy and dementia: a systematic review. *BMC Neurol*. 2009;9(1):3.
233. Gorelick PB, Scuteri A, Black SE, DeCarli C, Greenberg SM, Iadecola C, et al. Vascular Contributions to Cognitive Impairment and Dementia. *Stroke*. 2011;42(9):2672–713.
234. Rosand J, Muzikansky A, Kumar A, Wisco JJ, Smith EE, Betensky RA, et al. Spatial clustering of hemorrhages in probable cerebral amyloid angiopathy. *Ann Neurol*. 2005;58(3):459–62.

235. Wilson D, Charidimou A, Werring DJ. Advances in understanding spontaneous intracerebral hemorrhage: insights from neuroimaging. *Expert Rev Neurother*. 2014;14(6):661–78.
236. Wilson D, Hostettler IC, Ambler G, Banerjee G, Jäger HR, Werring DJ. Convexity subarachnoid haemorrhage has a high risk of intracerebral haemorrhage in suspected cerebral amyloid angiopathy. *J Neurol*. 2017;264(4):664–73.
237. Greenberg SM, Vernooij MW, Cordonnier C, Viswanathan A, Al-Shahi R, Salman E, et al. Cerebral Microbleeds: A Field Guide to their Detection and Interpretation. *Lancet Neurol*. 2009;8(2):165–74.
238. Charidimou A, Werring DJ. Cerebral microbleeds: detection, mechanisms and clinical challenges. 2011;6(5):587–611.
239. Maxwell SS, Jackson CA, Paternoster L, Cordonnier C, Thijs V, Salman RA-S, et al. Genetic associations with brain microbleeds: Systematic review and meta-analyses. *Neurology*. 2011;77(2):158–67.
240. van Rooden S, van der Grond J, van den Boom R, Haan J, Linn J, Greenberg SM, et al. Descriptive Analysis of the Boston Criteria Applied to a Dutch-Type Cerebral Amyloid Angiopathy Population. *Stroke*. 2009;40(9):3022–7.
241. Greenberg SM, Eng JA, Ning M, Smith EE, Rosand J. Hemorrhage Burden Predicts Recurrent Intracerebral Hemorrhage After Lobar Hemorrhage. *Stroke*. 2004;35(6):1415–20.
242. Akoudad S, Portegies MLP, Koudstaal PJ, Hofman A, van der Lugt A, Ikram MA, et al. Cerebral Microbleeds Are Associated With an Increased Risk of Stroke. *Circulation*. 2015;132(6):509–16.
243. Charidimou A, Boulouis G, Haley K, Auriel E, Etten ES van, Fotiadis P, et al. White matter hyperintensity patterns in cerebral amyloid angiopathy and hypertensive arteriopathy. *Neurology*. 2016;86(6):505–11.
244. Linn J, Halpin A, Demaerel P, Ruhland J, Giese AD, Dichgans M, et al. Prevalence of superficial siderosis in patients with cerebral amyloid angiopathy. *Neurology*. 2010;74(17):1346–50.
245. Vernooij MW, Lugt A van der, Ikram MA, Wielopolski PA, Niessen WJ, Hofman A, et al. Prevalence and risk factors of cerebral microbleeds. *Neurology*. 2008;70(14):1208–14.
246. Roongpiboonsopit D, Charidimou A, William CM, Lauer A, Falcone GJ, Martinez-Ramirez S, et al. Cortical superficial siderosis predicts early recurrent lobar hemorrhage. *Neurology*. 2016;87(18):1863–70.
247. Charidimou A, Farid K, Baron J-C. Amyloid-PET in sporadic cerebral amyloid angiopathy. *Neurology*. 2017;89(14):1490–8.
248. Stam AH, Kothari PH, Shaikh A, Gschwendter A, Jen JC, Hodgkinson S, et al. Retinal vasculopathy with cerebral leukoencephalopathy and systemic manifestations. *Brain*. 2016;139(11):2909–22.
249. Pelzer N, Hoogeveen ES, Haan J, Bunnik R, Poot CC, van Zwet EW, et al. Systemic features of retinal vasculopathy with cerebral leukoencephalopathy and systemic manifestations: a monogenic small vessel disease. *J Intern Med*. 2018;
250. Glezer A, Bronstein MD, Glezer A, Bronstein MD. Pituitary apoplexy: pathophysiology, diagnosis and management. *Arch Endocrinol Metab*. 2015;59(3):259–64.
251. Fernandez A, Karavitaki N, Wass JAH. Prevalence of pituitary adenomas: a community-based, cross-sectional study in Banbury (Oxfordshire, UK). *Clin Endocrinol (Oxf)*. 2010;72(3):377–82.
252. Briet C, Salenave S, Bonneville J-F, Laws ER, Chanson P. Pituitary Apoplexy. *Endocr Rev*. 2015;36(6):622–45.
253. Randeve HS, Schoebel J, Byrne J, Esiri M, Adams CBT, Wass JAH. Classical pituitary apoplexy: clinical features, management and outcome. *Clin Endocrinol (Oxf)*. 1999;51(2):181–8.
254. Pötting M, Tampieri D, Rüfenacht DA, Mohr G, Garant M, Del Carpio R, et al. The various MRI patterns of pituitary apoplexy. *Eur Radiol*. 1999;9(5):918–23.
255. Laidlaw JD, Tress B, Gonzales MF, Wray AC, Ng WH, O'Brien JM. Coexistence of aneurysmal subarachnoid haemorrhage and pituitary apoplexy: Case report and review of the literature. *J Clin Neurosci*. 2014;10(4):478–82.
256. Sibal L, Ball SG, Connolly V, James RA, Kane P, Kelly WF, et al. Pituitary Apoplexy: A Review of Clinical Presentation, Management and Outcome in 45 Cases. *Pituitary*. 2004;7(3):157–63.
257. Gruber A, Clayton J, Kumar S, Robertson I, Howlett TA, Mansell P. Pituitary apoplexy: retrospective review of 30 patients—is surgical intervention always necessary? *Br J Neurosurg*. 2006;20(6):379–85.
258. Flanagan EP, Leep Hunderfund A, Giannini C, Meissner I. Addition of magnetic resonance imaging to computed tomography and sensitivity to blood in pituitary apoplexy. *Arch Neurol*. 2011;68(10):1336–7.
259. Semple PL, Jane JA, Lopes MBS, Laws ER. Pituitary apoplexy: correlation between magnetic resonance imaging and histopathological results. *J Neurosurg*. 2008;108(5):909–15.
260. Dubuisson AS, Beckers A, Stevenaert A. Classical pituitary tumour apoplexy: Clinical features, management and outcomes in a series of 24 patients. *Clin Neurol Neurosurg*. 2007;109(1):63–70.
261. Tosaka M, Sato N, Hirato J, Fujimaki H, Yamaguchi R, Kohga H, et al. Assessment of hemorrhage in pituitary macroadenoma by T2*-weighted gradient-echo MR imaging. *Am J Neuroradiol*. 2007;28(10):2023–9.

The value of magnetic resonance imaging in the assessment of chemoradiotherapy of cancer of cervix uteri

Vaida Atstupėnaitė¹, Ieva Kraujutienė¹, Rūta Jonė Nakaitė¹, Edita Bieliūnienė¹, Algidas Basevičius¹

¹ Faculty of Medicine, Lithuanian University of Health Sciences, Kaunas, Lithuania,

ABSTRACT

Background and aim. Magnetic resonance imaging (MRI) is one of the most useful and frequent methods of examinations to monitor patients after chemoradiotherapy, in order to assess residual tumor tissue and relapse of the disease. This study aims to evaluate the diagnostic value of MRI in the assessment of the effectiveness of the treatment of cancer of cervix uteri.

Materials and methods. Retrospective data of 52 patients were obtained. All these patients underwent pelvic MRI in the Hospital of Lithuanian University of Health Sciences Kauno klinikos to assess the malignant tumor of cervix six months after chemoradiotherapy in the year 2010. MRI diagnostic value characteristics were calculated, compared with clinical data, obtained in the period of 5 or more years after chemoradiotherapy.

Results. Residual tumor tissue was found in 25.0 % of patients. In 28.2 % of patients with non-keratinizing squamous cell carcinoma, in 20.0 % of patients with keratinizing squamous cell carcinoma and 0.0 % of patients with adenocarcinoma, the residual tumor was found. In 100 % of patients with G1 tumors, in 23.4 % of patients with G2 tumors and 25.0 % of patients with G3 tumors, residual tumor tissue was found. In 12.5 % of cases the residual tumor was diagnosed within the range of 1.0-3.0 cm, in 19.2 % – within the range of 3.0-5.0 cm, in 25.0 % – within the range of 5.0-7.0 cm, in 75.0 % – within the range of 7.0-9.0 cm, in 75.0 % – within the range of 7.0-9.0 cm. In 26.5 % of patients with tumor extension to parametrium, in 28.6 % of patients with tumor extension to corpus uteri/vagina, in 60.0 % of patients with tumor extension to bladder/rectum and 28.1 % of patients with abnormal pelvic lymph nodes, residual tumor tissue was found. The specificity of MRI in the detection of residual tumor was 100.0%, sensitivity – 63.6%, positive prognostic value (PPV) – 100.0%, negative prognostic value (NPV) – 78.9% and accuracy – 84.6%. Matthews correlation coefficient (MCC) was 0.71.

Conclusions. MRI allowed diagnosing residual tumor tissue in 25.0 % of patients. Residual tumor tissue was most commonly diagnosed in patients with non-keratinizing squamous cell carcinoma, G1 carcinoma, large tumors and tumors with invasion to bladder and rectum. In the diagnostic of residual tumor tissue, MRI showed moderate sensitivity, high specificity, accuracy, PPV and NPV.

Keywords: magnetic resonance imaging, cancer of cervix uteri, chemoradiotherapy, residual tumor tissue.

INTRODUCTION

Cancer of cervix uteri is the second most frequent cancer and the third cause of death in the world [1–3]. Disease relapses and causes death in approximately 30 % of female patients. According to the literature data, 5-years survival is only 64 % [3, 4].

According to the data presented by the National Cancer Institute, in 2012 the incidence of cancer of cervix uteri in all age groups accounted for 5 % of all malignant tumors in females. The incidence of the cancer of cervix uteri in females in the age group of 15-29 years was the second

after the incidence of thyroid cancer and accounted for 13 % of all cancers. In 2012, mortality from cancer of cervix uteri in Lithuania in all age groups accounted for 6 % of all malignant tumors. Mortality from cancer of cervix uteri in the age group of 35-54 years was the second after mortality from breast cancer and accounted for 15 % [5].

Accurate assessment of the extent of the spread of cancer is extremely important for the selection of the appropriate treatment modality. However, the medical examination does not allow identification of the size of a tumor, especially when infiltrative tumors are diagnosed and tumor in-

filtrates parametrium and pelvic wall and when lymph node metastases are observed. A biopsy may not agree with the results of postoperative histopathological examination because tumors are often heterogenic. Non-invasive visualization methods provide useful additional information which is necessary for precise evaluation of the clinical stage [6].

The prognosis of the disease depends on the stage at the time of diagnosis, the size of the tumor, its histological type, stromal infiltration, local and distant metastases [6]. Magnetic resonance imaging (MRI) is extremely valuable for the evaluation of the local extent of cancer of cervix uteri which predetermines the selection of treatment modality and prognosis of the disease. MRI is especially valuable in patients selected for chemoradiotherapy when radical hysterectomy is impossible [2, 7].

It is essential to monitor patients after chemoradiotherapy in order to assess residual tumor tissue and relapse of the disease. In this case, clinical examination is not very accurate. Computed tomography (CT) does not allow precisely to differentiate residual tumor tissue with radiation fibrosis and other possible abnormalities, and therefore MRI is one of the most useful and frequent methods of examinations. When a residual tumor is detected, and additional chemotherapy and radiotherapy are applied survival prognosis improves, and therefore, early diagnosis of relapse or residual tumor is of extreme value [8, 9].

AIM

To evaluate the diagnostic value of MRI in the assessment of the effectiveness of the treatment of cancer of cervix uteri.

OBJECTIVES

1. To determine the number of patients with residual tumor tissue detected by the MRI method.
2. To assess the distribution of residual tumor tissue according to the size of the previous tumor, local extension, histological type and grade of differentiation.
3. To calculate the sensitivity of MRI, its specificity, accuracy, positive prognostic value (PPV), negative prognostic value (NPV) in the evaluation of the effectiveness of treatment.

MATERIALS AND METHODS

Retrospective data of 52 (n=52) patients were obtained from the Registration Office of the Department of Obstetrics and Gynaecology of the Hospital of Lithuanian University of Health Sciences Kauno klinikos archive and Hospital Information System (HIS). All these patients underwent pelvic MRI in the Department of Radiology to assess the malignant tumor of cervix six months after chemoradiotherapy in the year 2010.

Pelvic MRIs were performed by 1.5 T MRI scanner "Siemens Magnetom Avanto Syngo MR B 15", equipped with a pelvic coil, with patients in a supine position, their hands raised overhead, and legs straighten. Anterior, lateral, axial and axial oblique plains were employed according to pelvic examination protocol.

The first phase involved a native scan in T1W/TIRM, T1W/TSE, and T2W/TSE sequences. The second stage included a DW/EPI sequence using b values of 50, 400 and 800 s/mm². ADC maps were reconstructed from DW images. The third phase consisted of T1W/TSE and T1W/SE/FS sequences using an intravenous gadolinium-based contrast medium. Contrast medium was injected into a peripheral vein; the precise amount was calculated according to the patient's body weight: 1 ml product / 5 kg body weight or 15 ml / 75 kg.

The following patients' characteristics were used for the research data analysis: patients' age, tumor size and extent before treatment, histological type, and differentiation grade. Tumor size and extent were assessed using MRI data obtained before chemoradiotherapy. Assessment of tumor histological type and differentiation grade were based on data of morphological examination of biopsy specimens obtained before initiation of treatment. The number of cases with residual tumor detected using MRI 6 months after chemoradiotherapy was also assessed. MRI sensitivity, specificity, and accuracy were also calculated as well as PPV and NPV compared with clinical data obtained in the period of 5 or more years after chemoradiotherapy.

According to various authors, a 5-years survival period after the treatment of cancer of cervix uteri was selected because a statistically signifi-

cant decrease in a number of relapses after that period is observed and follow-up visits are required only once yearly. This period is sufficient to determine the absence of relapse or residual tumor tissue as weighted regression [10].

The Matthews correlation was used to identify classification quality.

The obtained data were analyzed using software packages "SPSS 17.0" and "Excel 2016". The selected level of statistical significance was $p < 0.05$. Quantitative data were presented as an average and a standard deviation. Qualitative data were presented as absolute numbers and percentages.

RESULTS

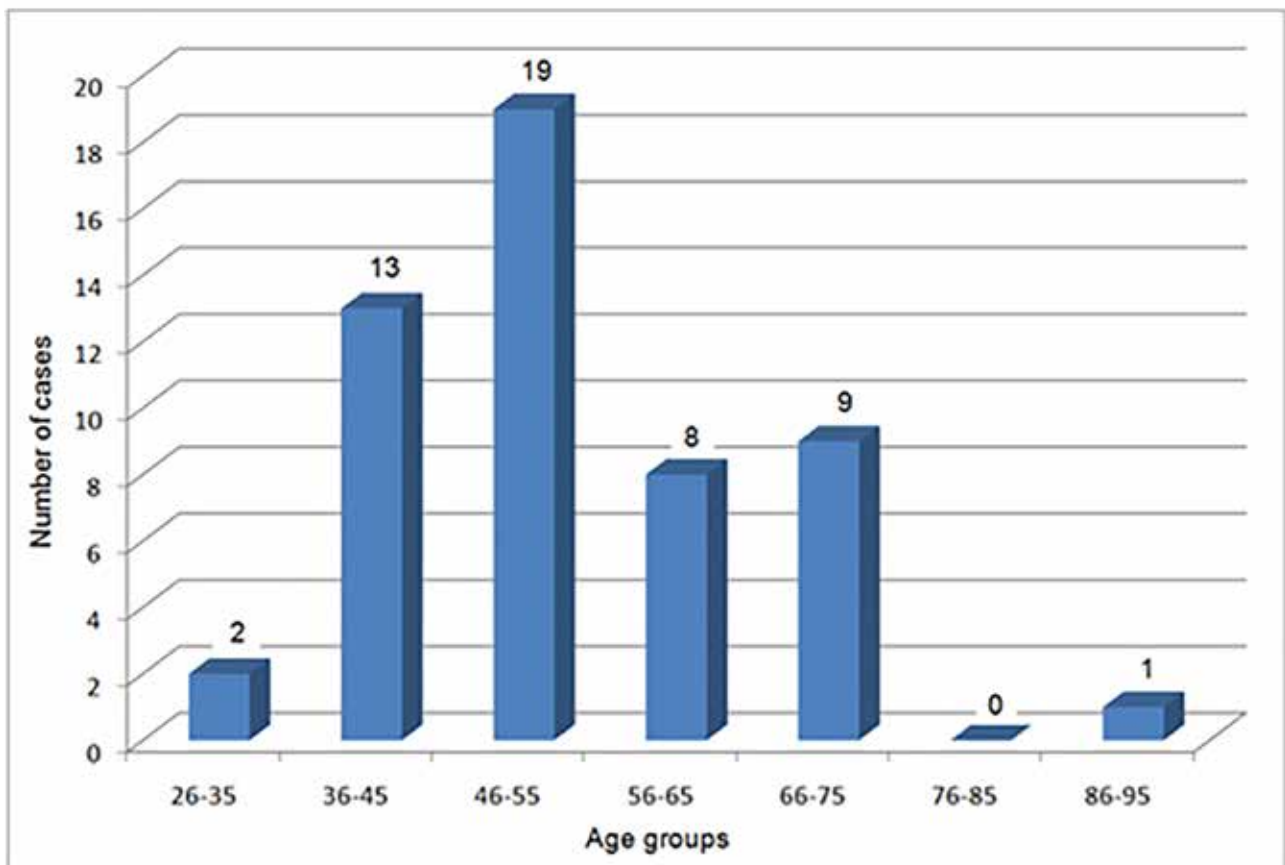
In 2010 in the Clinic of Radiology MRI to assess the tumor of cervix uteri six months after

chemoradiotherapy was performed in 52 patients. Patients' age ranged from 29 to 86 years, the average age was 52.9 ± 11.86 years (Figure 1). Histological examination showed keratinizing squamous cell carcinoma in 39 patients (75.0 %), non-keratinizing squamous cell carcinoma in 10 patients (19.2 %) and adenocarcinomas in 3 patients (5.8 %).

In 1 patient (1.9 %) G1 grade was established at diagnosis, in 47 patients (90.4 %) – G2 grade, and in 4 patients (7.7 %) – G3 grade.

Tumor distribution by tumor sizes was assessed, it ranged from 1.2 to 11.0 cm, average was 4.74 ± 1.90 cm. 8 number of cases (15.4 %) were within 1.0 – 3.0 cm, 26 (50.0 %) – within 3.0 – 5.0 cm, 12 (23.1 %) – within 5.0 – 7.0 cm, 4 (7.7 %) – within 7.0 – 9.0 cm, 2 (3.8 %) – within 9.0 – 11.0 cm range.

Figure 1. Patients' distribution by age groups



The local extension of the tumor was assessed. Invasion to parametrium was diagnosed in 49 patients (94.2 %), invasion to corpus uteri/vagina was diagnosed in 28 patients (53.8 %) and invasion to bladder/rectum was diagnosed in 5

patients (9.6 %).

MRI performed six months after chemoradiotherapy was used to assess the number of patients with residual tumor; it was diagnosed in 13 patients (25.0 %) (Figure 2).



Figure 2. Pelvic MRI, T2W/TSE sequence, lateral (A) and axial (B) planes. Cervix uteri are large; its structure is heterogeneous – changes after chemoradiotherapy. Infiltration with abnormal SI is observed along the cervical canal – residual tumor masses

Residual tumor tissue was not found in 39 patients (75.0 %) (Figure 3).

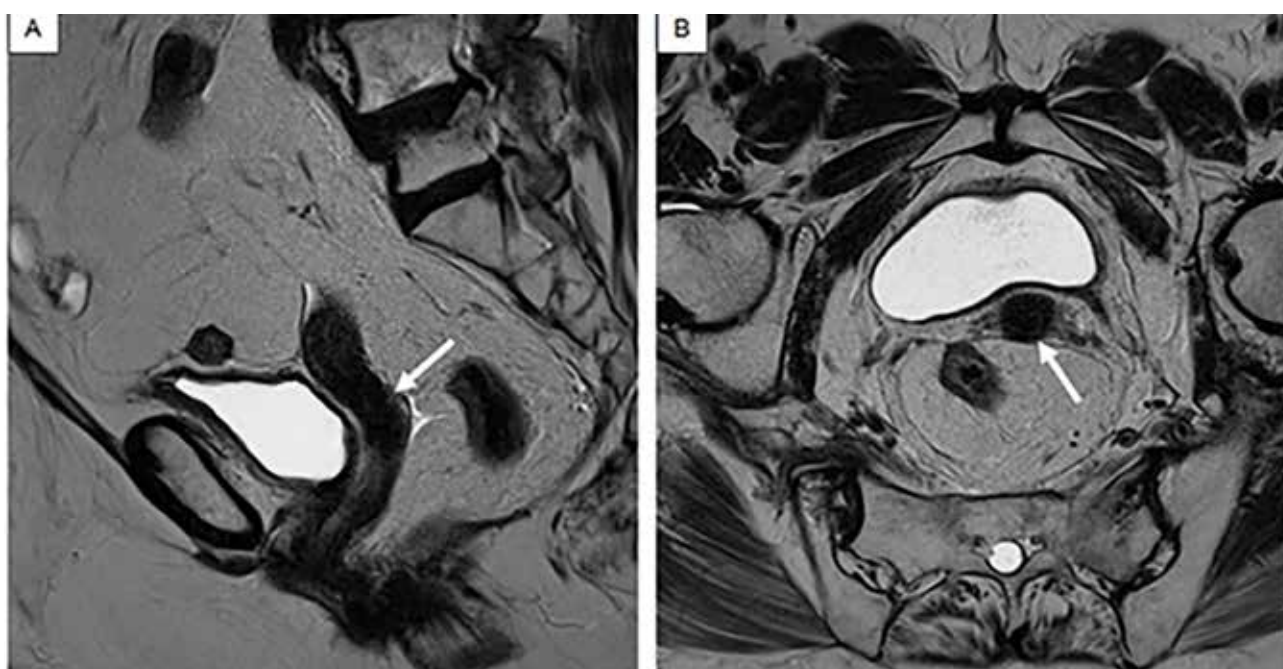
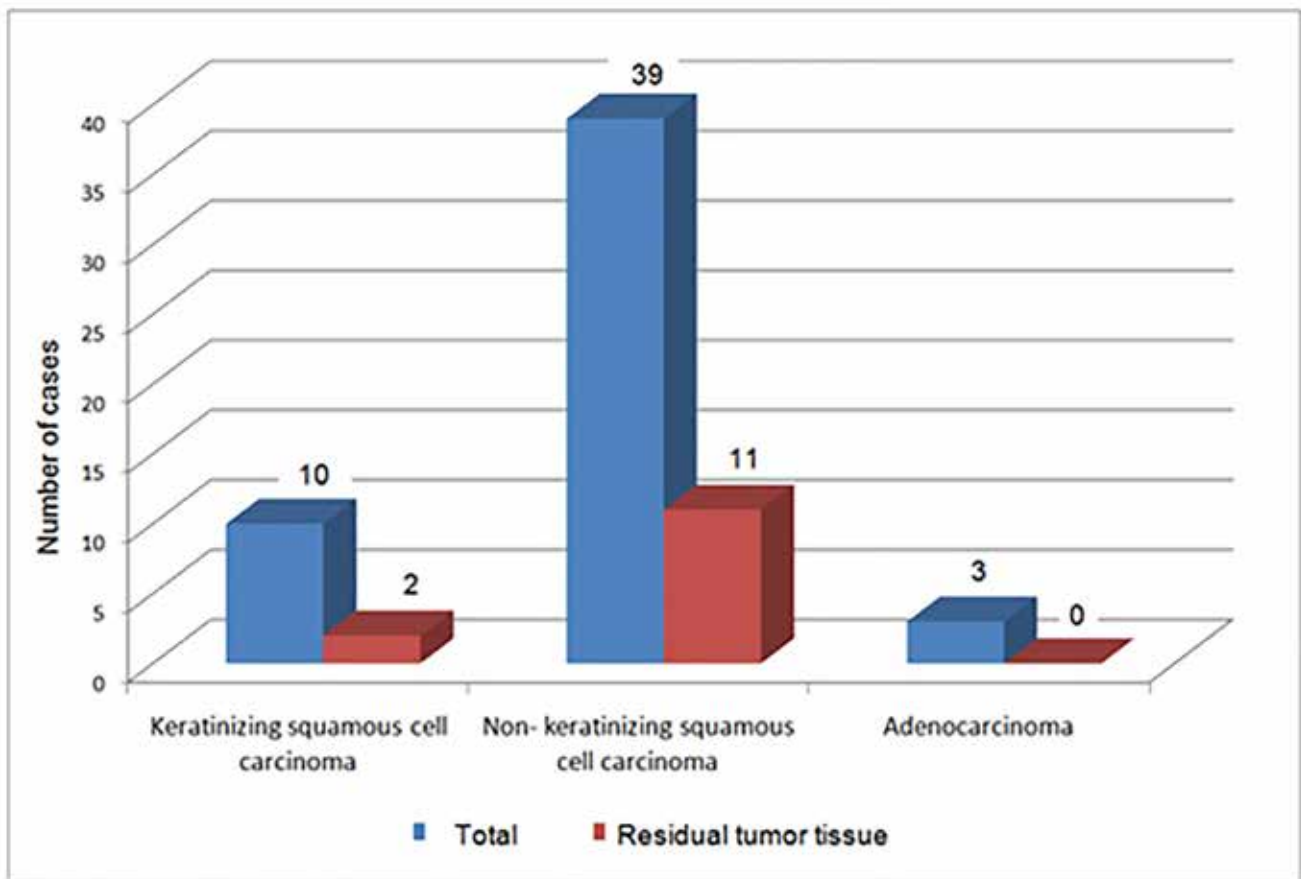


Figure 3. Pelvic MRI, T2W/TSE sequence, lateral (A) and axial (B) planes. Changes after chemoradiotherapy are visible. Cervix uteri are small in size, homogeneous; no unusual SI lesions are observed (arrows).

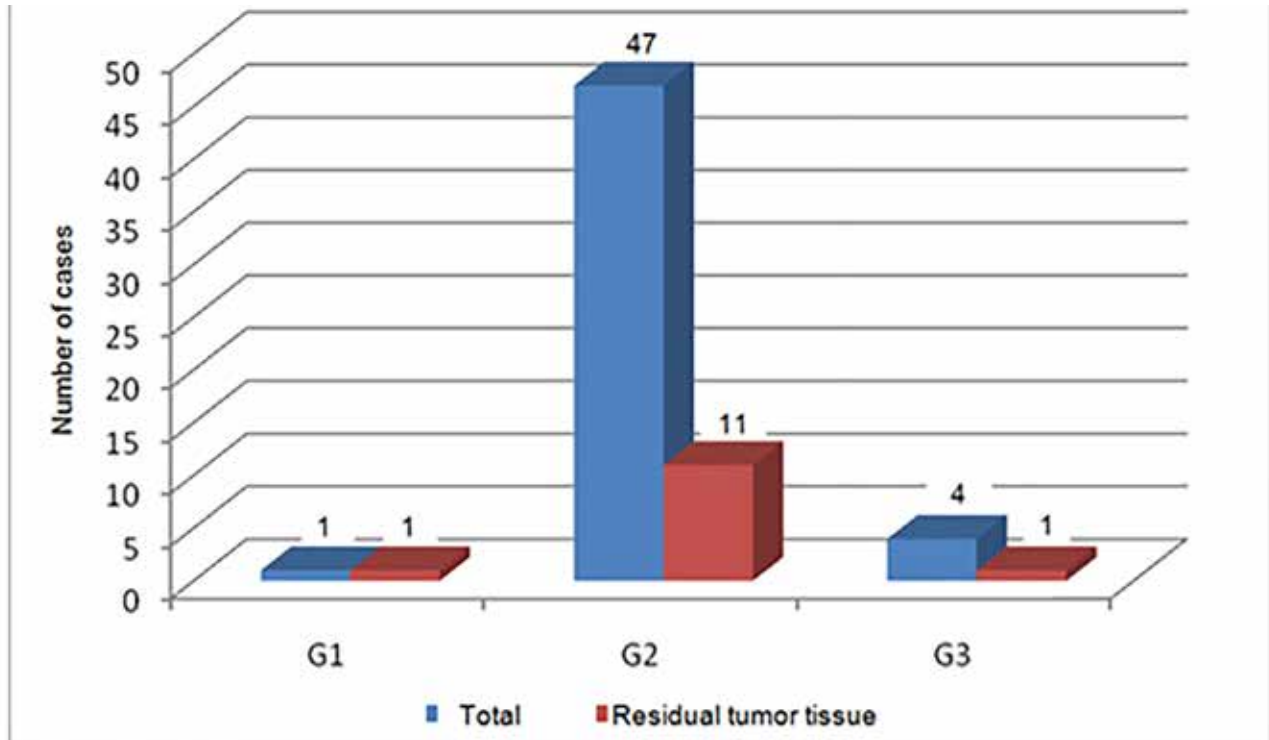
The distribution of residual tumor tissue by tumor histological type was analyzed. In 11 out of 39 patients (28.2 %) with non-keratinizing squamous cell carcinoma, residual tumor was found. In 2 out of 10 patients (20.0 %) with keratinizing squamous cell carcinoma, the residual tumor was found. Moreover, in 0 out of 3 patients with residual adenocarcinoma tumor was found (0.0 %) (Figure 4).

Figure 4. Residual tumor tissue distribution by histological type



The distribution of residual tumor tissue by tumor differentiation grade was presented. In 1 out of 1 (100 %) patient with a G1 tumor, residual tumor tissue was found. In 11 out of 47 (23.4 %) patients with a G2 tumor, residual tumor tissue was found. Moreover, in 1 patient out of 4 (25.0 %) with a G3 tumor, residual tumor tissue was found (Figure 5).

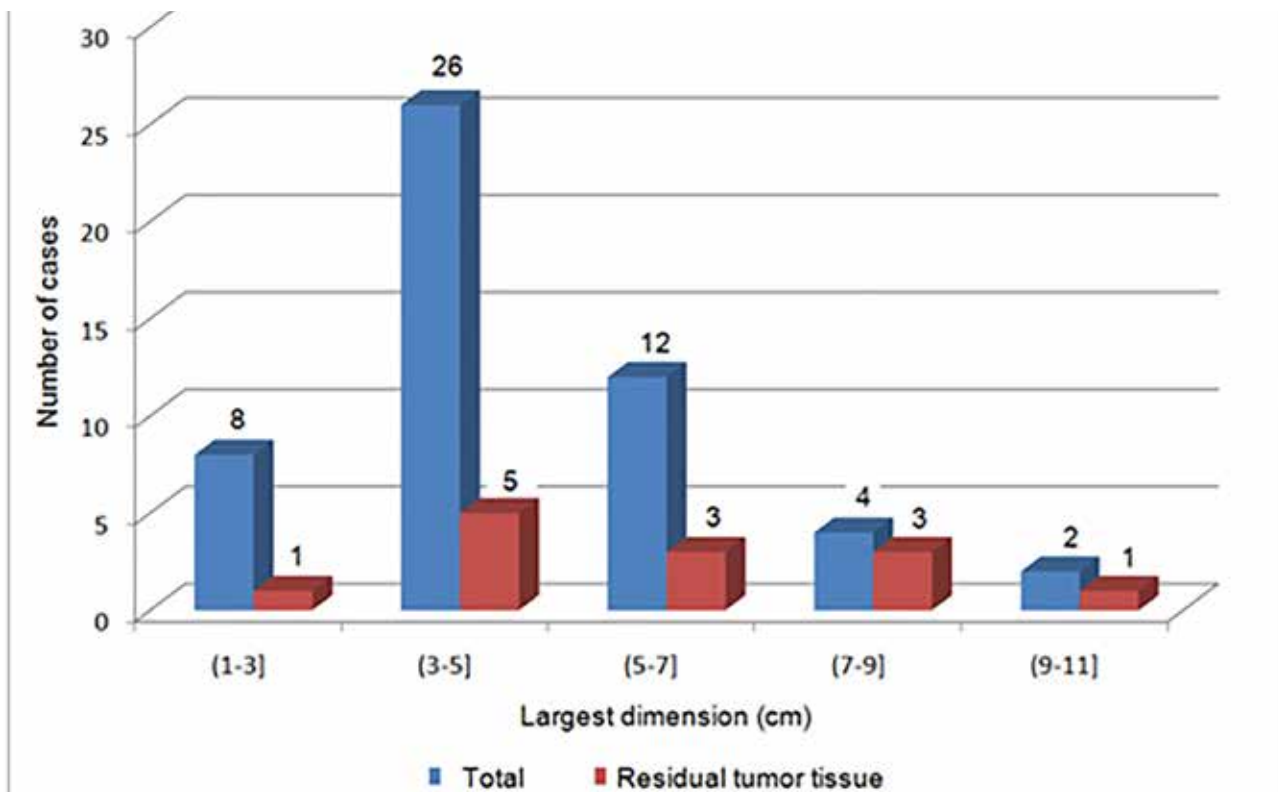
Figure 5. Residual tumor tissue distribution by tumor grade



The number of cases with residual tumor tissue before treatment was compared with the tumor size (largest dimension). 1 out of 8 (12.5 %) residual tumor was diagnosed within the range of 1.0-3.0 cm. 5 out of 26 (19.2 %) residual tumor was diagnosed within the range of 3.0-5.0 cm. 3

out of 12 (25.0 %) residual tumor was diagnosed within the range of 5.0-7.0 cm. 3 out of 4 (75.0 %) residual tumor was diagnosed within the range of 7.0-9.0 cm. 1 out of 4 (75.0 %) residual tumor was diagnosed within the range of 7.0-9.0 cm (Figure 6).

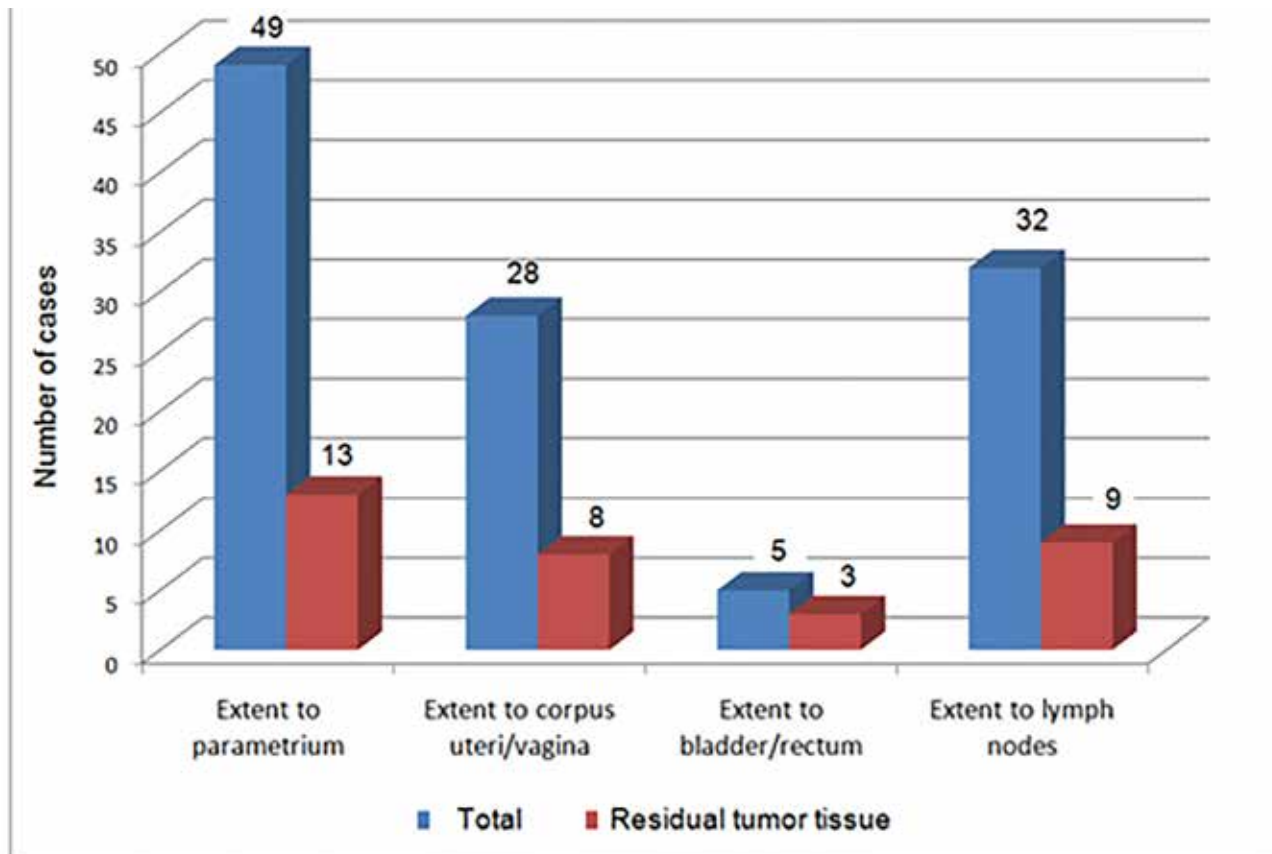
Figure 6. Residual tumor tissue distribution by tumor size



The number of patients with residual tumor tissue was compared with local tumor extension before treatment. Extension to parametrium was diagnosed in 49 patients, 13 (26.5 %) of them were diagnosed with residual tumor tissue. Extension to corpus uteri/vagina was diagnosed in 28 patients, 8 (28.6 %) of them were diagnosed

with residual tumor tissue. Extension to bladder/rectum was diagnosed in 5 patients, 3 (60.0 %) of them were diagnosed with residual tumor tissue. Abnormal pelvic lymph nodes were diagnosed in 32 patients, 9 (28.1 %) of them were diagnosed with residual tumor tissue (Figure 7).

Figure 7. Residual tumor tissue distribution by tumor extent



MRI was performed six months after chemoradiotherapy diagnostic value characteristics were calculated and compared with clinical data obtained after 5 or more years after chemoradiotherapy. MRI showed no tumor relapse in 38 patients. In 30 of them findings were real negative (TN) (MRI shows no residual tumor, and no clinical symptoms of the disease are observed within 5 years after chemoradiotherapy) and in 8 patients findings were false negative (FN) (MRI shows no residual tumor. However, disease relapses within 5 years after chemoradiotherapy). In 14 patients MRI showed residual tumor tissue, of them in 14 patients findings were real positive (TP) (MRI shows residual tumor tis-

sue and disease relapses within five years after chemoradiotherapy). No false negative findings (FN) were obtained (MRI shows residual tumor tissue although no clinical signs of the disease are observed within five years after chemoradiotherapy) (Table 1).

Table 1. Outline of the calculation of MRI diagnostic value characteristics

Tests	Clinically confirmed	Clinically not confirmed
MRI diagnosed	14 (TP)	0 (FP)
MRI not diagnosed	8 (TN)	30 (FN)

According to the results obtained, diagnostic value characteristics of MRI performed six months after chemoradiotherapy were calculated: specificity – 100.0%, sensitivity – 63.6%, PPV – 100.0%, NPV – 78.9% and accuracy – 84.6%. Because no false positive finding was obtained, specificity and PPV were ideal.

Our research showed extremely high Matthews correlation coefficient (MCC=0.71). It shows the high quality of MRI diagnostic value characteristics.

DISCUSSION

In Lithuania and globally, cancer of cervix uteri is one of the most common malignancies in females. According to the data presented by the National Cancer Institute, it is most frequently diagnosed in females in 50-54 years age group [5]. According to the data of our research, it was most frequently diagnosed in females of 46-55 years age group. Therefore our results are close to the literature data.

Assessment of histological findings showed that squamous cell carcinoma is the most common in patients with cancer of cervix uteri. Adenocarcinoma is far rarer, and it accounts for 5-20 % of all cases of cancer of cervix uteri [11, 12]. Our research data are quite similar: squamous cell carcinoma (both keratinizing and non-keratinizing) was diagnosed in 49 out of 52 patients (94.2 %), and adenocarcinoma was diagnosed only in 3 out of 52 patients (5.8 % of all cases).

According to the data of the study conducted by G. Somoye et al., the disease relapses in 30 % of patients, and 5-years survival is approximately 64 % [4]. According to the study of Attia M. A. et al., local relapse after chemoradiotherapy was diagnosed in 31.2 % of patients [13]. According to many authors, the disease relapses in 35-61 % of patients [14]. Our research data show that residual tumor tissue is found slightly more rarely

by MRI performed six months after chemoradiotherapy and made up 25 % of all examined patients.

According to multiple studies, the comparison of relapse number and its previous size shows that the tumor size is a significant prognostic factor. The study of Werner-Wasik et al., showed that in patients with more substantial than 5cm tumor size, relapse was diagnosed in 83 % of patients if compared to the number of relapses in patients with the tumor smaller than 5 cm (53 %). In patients with FIGO stages I and II, the tumor size is even more critical prognostic factor if compared to the stage of the disease [15]. Our study also showed that the majority of patients with residual tumor tissue were diagnosed in the group of patients with large tumor (5-7 cm), and it accounted for 75.0 % of all cases.

Extension to parametrium significantly increases the risk of the residual tumor tissue. According to the study of Werner-Wasik et al., the tumor relapse was diagnosed in 25 % of patients that were not diagnosed with tumor extension to parametrium at initial examination and in 54 % of patients with diagnosed tumor extent to parametrium [15]. Our research showed better results – residual tumor tissue was diagnosed in 26.5 % of patients with tumor extension to parametrium. Literature presents insufficient data concerning the tumor differentiation impact on residual tumor tissue and tumor relapse. Several studies showed that the tumor differentiation grade has no significant effect on the development of tumor relapse [16, 17]. We had only one patient with G1 grade and four patients with G3, so it is impossible to make a relevant conclusion concerning the grade of differentiation and residual tumor tissue.

Several studies were conducted to assess the character of the diagnostic value of MRI in the tumor relapse and residual tumor tissue diagnostic. Many studies evaluated MRI sensitivity

and specificity in the diagnosis of tumor relapse after chemoradiotherapy. E. Vincens et al. conducted one of the most extensive studies. They assessed 43 MRIs after chemoradiotherapy and found that MRI sensitivity was 80 % and specificity was 55 %. There were 50 % of FN findings and 17 % of FP findings [18]. In the study conducted by P. Lavoue et al. 29 MRIs performed after chemoradiotherapy were assessed. MRI sensitivity was 77 %, and specificity was 60 % [14]. According to the data presented by H. Hricak et al., MRI accuracy in assessing the tumor relapse after chemoradiotherapy was 78 %, PPV – 65 % and NPV – 97 %. The accuracy of MRI, conducted earlier than six months after radiotherapy was 69% and specificity was 46 %. These diagnostic value characteristics were much higher when MRIs were conducted in more than six months after initiation of chemoradiotherapy: accuracy was 88 %, and specificity was 81 % [19]. Therefore, our research shows that MRI is considerably more accurate and sensitive when it is conducted not earlier than six months after treatment. MRIs that we have assessed were conducted six months after chemoradiotherapy. Our accuracy was somewhat similar, and it was 86.6 %, and specificity was 100 %.

Due to insufficient sample size during our research, we did not calculate the correlation between residual tumor tissue and histological type, grade of differentiation and tumor local extent.

CONCLUSIONS

1. MRI allowed diagnosing residual tumor tissue in 25.0 % of patients. Moreover, residual tumor tissue was not found in 75.0 % of patients.
2. Patients with non-keratinizing squamous cell carcinoma and well-differentiated carcinoma of cervix uteri were most commonly diagnosed with residual tumor tissue.
3. Residual tumor tissue was most commonly diagnosed in patients with large (7.0-9.0 cm) tumors and patients with tumor invasion to bladder and rectum.
4. In the diagnostic of residual tumor tissue, MRI showed moderate sensitivity, high specificity, accuracy, PPV and NPV.

REFERENCES

- Fields EC, Weiss E. A practical review of magnetic resonance imaging for the evaluation and management of cervical cancer. *Radiation Oncology* 2016; 15: 11–5.
- Demirbaş T, Cimilli T, Bayramoğlu S, Güner NT, Hocaoglu E, Inci E. Contribution of diffusion-weighted imaging to diagnosis and staging of cervical cancer. *Balkan Med J* 2014; 31(2): 154–7.
- Hou B, Xiang SF, Yao GD, Yang SJ, Wang YF, Zhang YQ, Wang J. Diagnostic significance of diffusion-weighted MRI in patients with cervical cancer: a meta-analysis. *Tumour Biol* 2014; 35: 11761–9.
- Somoye G, Harry V, Semple S, Plataniotis G, Scott N, Gilbert FJ, Parkin D. Early diffusion-weighted magnetic resonance imaging can predict survival in women with locally advanced cancer of the cervix treated with combined chemoradiation. *Eur Radiol* 2012; 22(11): 2319–27.
- Smailytė G, Aleknavičienė B. Vėžys Lietuvoje 2012 metais. Vilnius, Lietuva: Petro ofsetas, 2015.
- Xue H, Ren C, Yang J, Sun Z, Li S, Jin Z, Shen K, Zhou W. Histogram analysis of apparent diffusion coefficient for the assessment of local aggressiveness of cervical cancer. *Arch Gynecol Obstet* 2014; 290(2): 341–8.
- Miccò M, Vargas HA, Burger IA, Kollmeier MA, Goldman DA, Park KJ, Abu-Rustum NR, Hricak H, Sala E. Combined pre-treatment MRI and 18F-FDG PET/CT parameters as prognostic biomarkers in patients with cervical cancer. *Eur J Radiol* 2014; 83: 1169–76.
- Jeong YY, Kang HK, Chung TW, Seo JJ, Park JG. Uterine Cervical Carcinoma after Therapy: CT and MR Imaging Findings. *Radio Graphics* 2003; 23(4): 969–81.
- Lucas R, Dias JL, Cunha TM. Added value of diffusion-weighted MRI in detection of cervical cancer recurrence: comparison with morphologic and dynamic contrast-enhanced MRI sequences. *Diagn Interv Radiol* 2015; 21(5): 368–75.
- Elit L, Fyles AW, Oliver TK. Follow-up for women after treatment for cervical cancer. *Curr Oncol* 2010; 17(3): 65–9.
- Drasutienė G, Triponienė D, Triponis VJ, Klimas V, Juodžbalienė E, Pilkauskienė A. Moterų ligos. Kaunas, Lietuva: Arx Baltica, 2010.
- He L, Wu G, Wei W, Han L. The efficacy of neoadjuvant chemotherapy in different histological types of cervical cancer. *Gynecologic Oncology* 2014; 134(2): 419–25.
- Attia AM, Salem MA, Amira G. Treatment Outcomes and Prognostic Factors of Cervical Cancer at South Egypt Cancer Institute. *Cancer Prevention & Current Research* 2015; 2(6): 2373–81.
- Hequet D, Marchand E, Place V, Fourchette V, De La Rochefordiere A, Dridi S, Coutant C, Lecuru F, Bats AS, Koskas M, Bretel JJ, Bricou A, Delpech Y, Barranger E. Evaluation and impact of residual disease in locally advanced cervical cancer after concurrent chemoradiation therapy: results of a multicenter study. *Eur J Surg Oncol* 2013; 39: 1428–34.
- Wernr-Wasik M, Schmid CH, Bornstein L, Ball HG, Smith DM, Madoc-Jones H. Prognostic Factors for Local and Distant Recurrence in Stage I and II Cervical Carcinoma. *International Journal of Radiation Oncology Biology Physics* 1995; 32(5): 130–17.
- Turan T, Yildirim BA, Tulunai G, Boran N. Prognostic effect of different cut-off values (20 mm, 30 mm and 40 mm) for clinical tumor size in FIGO stage IB cervical cancer. *Surgical Oncology* 2010; 19(2): 106–13.
- Kristensen GB, Abeler VM, Risberg B, Trope C. Tumor Size, Depth of Invasion, and Grading of the Invasive Tumor Front Are the Main Prognostic Factors in Early Squamous Cell Cervical Carcinoma. *Gynecologic Oncology* 1999; 74(2): 245–51.
- Vincens E, Balleyguier C, Rey A, Uzan C, Zereski E. Accuracy of magnetic resonance imaging in predicting residual disease in patients treated for stage IB2/II cervical carcinoma with chemoradiation therapy. *Cancer* 2008; 15(8): 2158–65.
- Hricak H, Swift PS, Campos JM, Quivey Z, Gildengorin V, Göranson H. Irradiation of the cervix uteri: value of unenhanced and contrast-enhanced MR imaging. *Radiology* 1993; 189(2): 126–38.

Pulmonary benign leiomyomas mimicking malignant pulmonary metastases: case report and literature review

Rokas Kurtinaitis¹, Kamilė Počepavičiūtė¹, Dovilė Barakauskaitė¹, Ieva Keturkaitė¹, Laima Dobrovolskienė¹, Algidas Basevičius¹

¹Department of Radiology of Lithuanian University of Health Sciences Kaunas, Lithuania.

ABSTRACT

Background and aim: Pulmonary leiomyomatosis (PBML) is the most common type of metastasizing leiomyomas. It is routinely found by a chest X-ray in women with a medical record of myomectomy related to uterine leiomyoma. These findings in young women are frequently misinterpreted as metastasized lung cancer due to the similarity of radiological findings. This article aims to describe a clinical case, define the diagnostic value of radiological imaging findings and to differentiate the distant leiomyoma metastases from malignant ones.

Material and methods: We present a new case of PBML post hysterectomy mimicking malignant pulmonary metastases. Additionally, a literature review was conducted for case reports and previous literature reviews describing PBML, its etiology, pathogenesis, and diagnostic features. Medline (PubMed), ScienceDirect, Hindawi, EPOSTM databases were used.

Results: PBML nodules pose a diagnostic ambiguity by mimicking malignant pulmonary metastases especially on routine chest X-rays and CT scans. Our presented case is similar to previously reported cases, and MRI played a crucial role in the differential diagnosis. In 10 of 13 investigated cases, nodules were multiple and bilateral, oval in shape and well-circumscribed. The average age of patients described in the reviewed case reports was 47,2 years. 77 % of them have had a history of leiomyoma and hysterectomy or myomectomy.

Conclusion: Although PBML is a rare condition it should be considered for patients with a history of leiomyoma or hysterectomy or myomectomy due to leiomyomatosis. It is essential seeing as these findings are often misdiagnosed as malignancy because of ambiguous radiological findings, such as bilateral and multifocal well-circumscribed rounded lesions that vary in size. MRI is a suitable tool for evaluating these nodules and ADC value can be useful to differentiate benign nodules from malignant metastasis.

Keywords: pulmonary leiomyomatosis, benign metastasizing leiomyoma, computed tomography.

INTRODUCTION

Benign metastasizing leiomyoma (BML) is a rare condition that may affect females in all age groups and is frequent in those with a medical history of uterine leiomyoma and myomectomy or rarely without this procedure [1]. However, BML mostly occurs in women during their late reproductive years [2]. The BML generally metastasizes to lungs, although it can be associated with metastases in the abdominal or paraaortic lymph nodes, liver, heart, breasts, muscular tissue or even the central nervous system. Consequently, the diagnosis of pulmonary benign metastasizing leiomyoma (PBML) is complicated. It can be misdiagnosed as bronchitis, pneumonia, pulmonary tuberculosis or metastasizing lung cancer because of non-specific clinical symptoms such as chest pain, cough or shortness of

breath, although usually, BML is asymptomatic. Frequently the diagnosis is based on imaging findings which are even more deceptive [3, 4]. Most cases of PBML may be discovered incidentally by chest X-ray or CT scans during routine examinations and may resemble malignant pulmonary metastases.

AIM

This article aims to describe a clinical case, define the diagnostic value of radiological imaging findings and to differentiate the distant leiomyoma metastases from malignant ones.

CASE REPORT MATERIAL

We present a clinical case of a 50-year-old woman with multiple pulmonary nodules after hysterectomy due to uterine leiomyomatosis and

selective literature review for case reports and literature reviews describing the pulmonary leiomyomatosis, its etiology, pathogenesis and diagnostic features published in the last five years. Medline (PubMed), ScienceDirect, Hindawi, EPOSTM databases were used to search for publications.

A 50-year-old woman was referred to a pulmonologist for consultation at the Hospital of LUHS (Lithuanian University of Health Sciences) Kaunas Clinics after multiple lung nodules varying in size were observed on a routine chest X-ray. Nodules were differentiated between granuloma and metastatic malignancy (Figure 1). The patient denied any symptoms and laboratory results were normal. According to medical history, seven years ago the patient had undergone a hysterectomy due to uterine leiomyomatosis. Lung CT (using Toshiba Aquilion One multislice CT equipment with and without contrast agent) was performed because of the suspected malignancy. CT showed multiple nodules varying in size, with attenuation values changing from 59HU to 100 HU after the injection of contrast agent (Figure 2). The following week a bronchoscopy and transbronchial biopsy were performed, but according to the pathological report, no malignant changes were observed.

A lung MRI was performed to analyze the enhancement, contrast agent wash-out significance and apparent diffusion coefficient (ADC) value of nodules, and exclude any malignant processes. MRI was performed using 1T Siemens Mag-

netom Aera in T1_VIBE, T2_HASTE, TIRM, DW sequences in the axial and coronal plane. MRI showed well defined, heterogeneous nodules with solid and cystic parts, and higher signal intensities (SI) in T2_HASTE and TIRM sequences. (Figure 3)

In the post-processing stage, SI in diffusion-weighted images was evaluated using different b values of 50,400 and 800, after this ADC was calculated to estimate restriction in nodules (Figure 4)

In precontrast T1_VIBE nodules were isointense, in CE T1_VIBE sequence after 5 min. of contrast agent injection SI was 40-77 and after 15 min it was approximately- 56 and wash-out was not significant (Figure 5) Because CE T1_VIBE delayed scans wash-out was not significant it did not allow to exclude malignant pulmonary metastases, but ADC was high, and features of restriction in nodules indicated benign nodules. The multidisciplinary team decided to perform a typical lung resection of one nodule from the right lower lobe for histological verification. Pathology identified a smooth muscle tumor. Immunohistochemical staining showed smooth-muscle desmin and actin, but was negative for CD117. Estrogen and progesterone receptors were strongly positive. These findings suggested pulmonary leiomyomatosis.

The patient was started on tamoxifen, an aromatase inhibitor, and GnRH analog. Further follow up was suggested using CT/MRI.

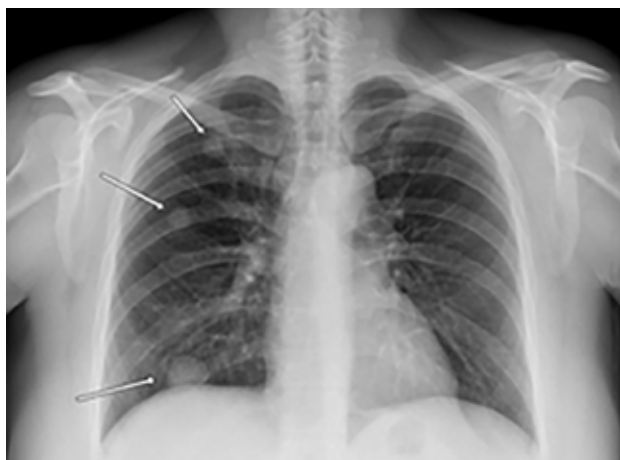


Figure 1. LUHS Radiology clinic archive

A, B Plain films of 50-year-old women demonstrate 1,0 - 3,5 cm well-defined oval nodules in the right lung upper and lower lobes (white arrows).

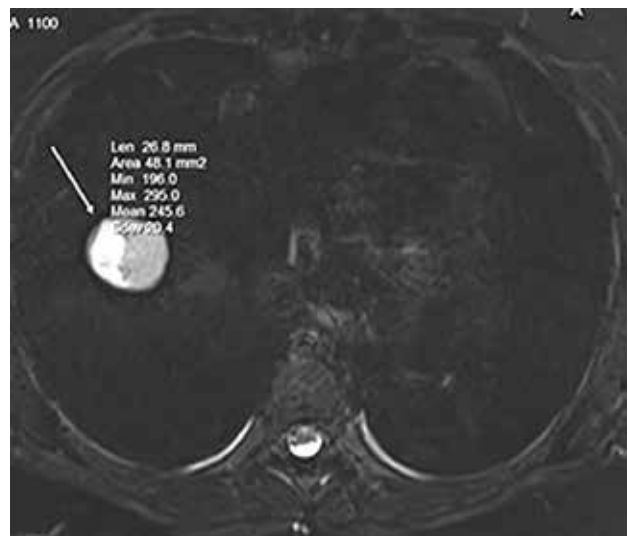


Figure 2. LUHS Radiology clinic archive
CT scans of the same 50-year old female with a history of uterine myomectomy. (A, B) native and C after i/v contrast agent administration. Scans demonstrate multiple well defined pulmonary nodules in variable size 2-32 mm in the right lung field, i/v contrast-enhanced from 59 HU in the native scan (C) to 100 HU in CE scan (B).

Figure 3. LUHS Radiology clinic archive
MRI scans of the same patient: A, B T2_HASTE axial images- white arrows show SI in the solid part of nodule – 373; C- TIRM axial slice – arrow show cystic part of nodule, SI -245.

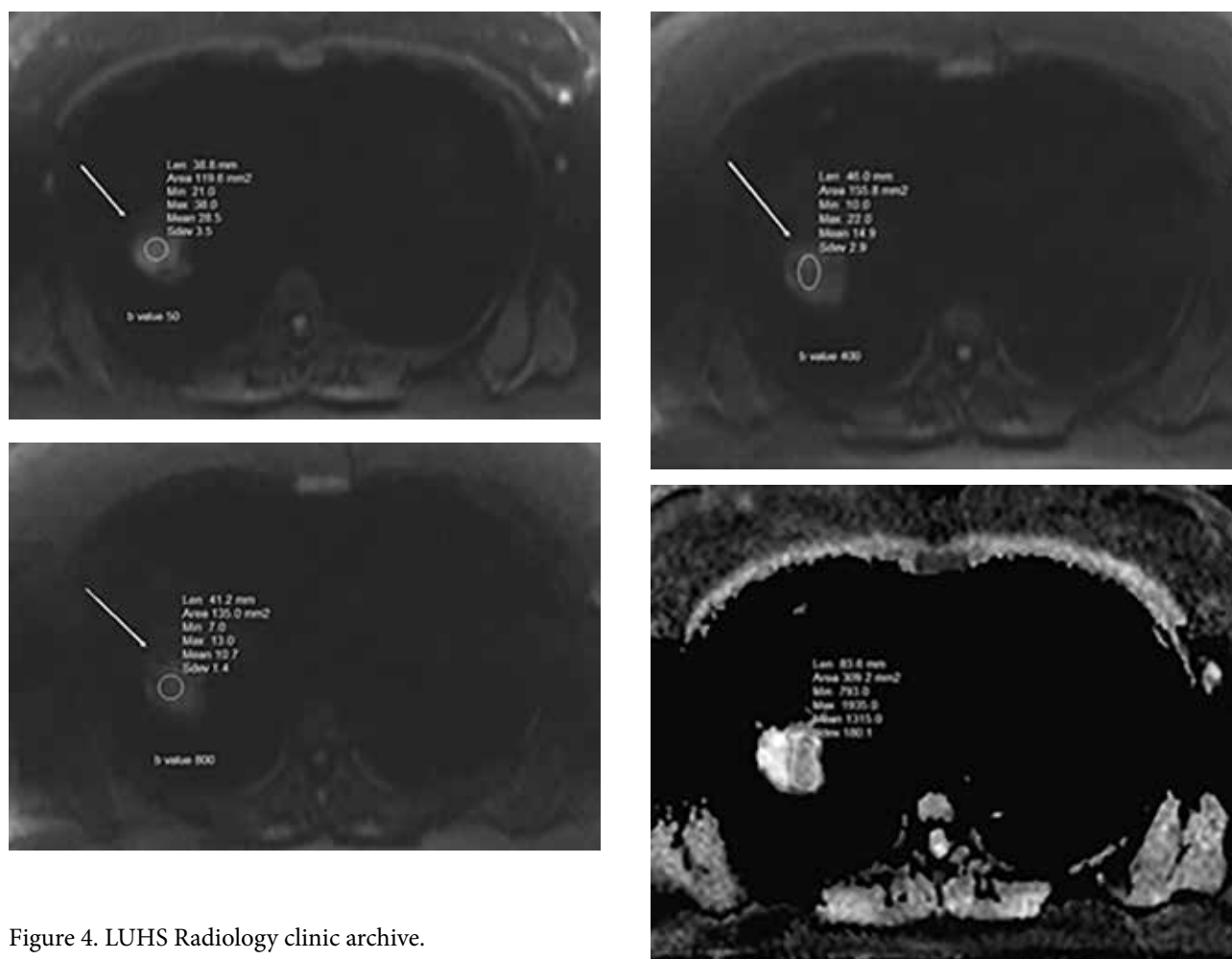


Figure 4. LUHS Radiology clinic archive.

A, B and C demonstrate the patient's MRI scans of DW sequences with different b values they show no restriction in nodule and D - ADC map with ADC value of solid part of nodule calculated $1,3 \times 10^{-3}$.

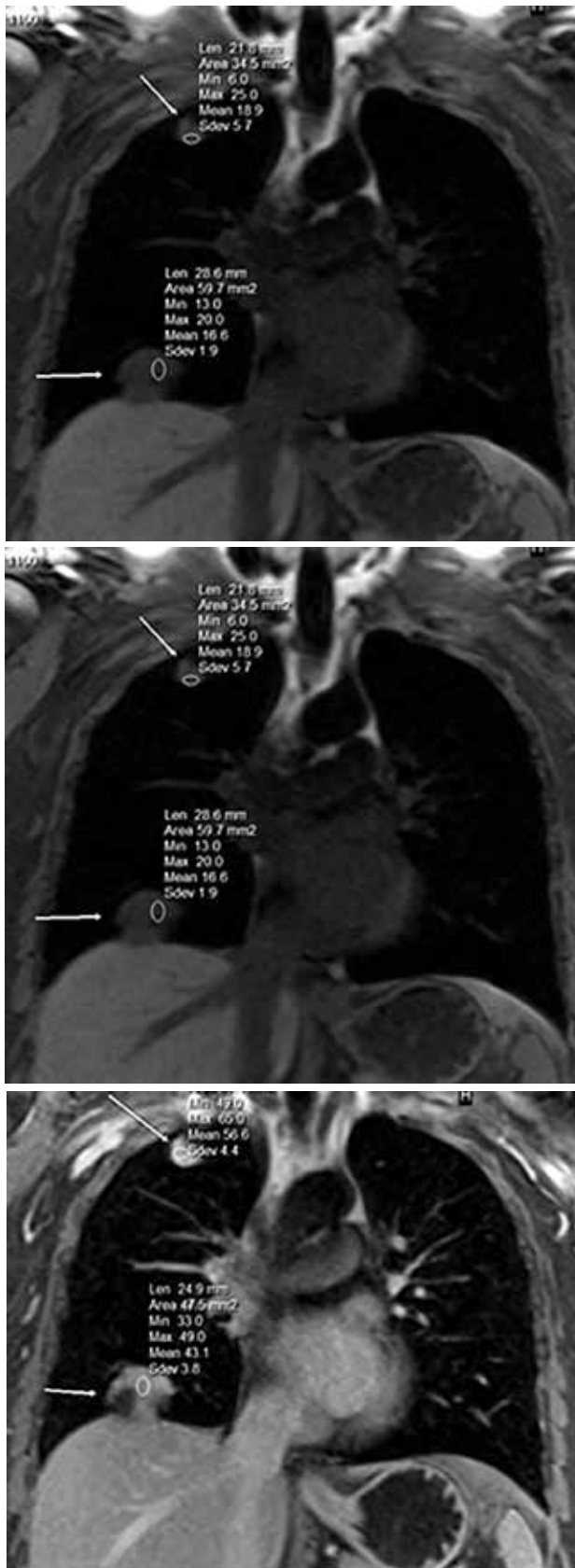


Figure 5. LUHS Radiology clinic view archive
A- Fat suppressed T1_VIBE coronal image before contrast injection: white arrows show nodules with measured SI- 19- 25, B- after 5 min of contrast enhancement (CE) SI was 77 and C after 15 min SI – 56. Heterogeneous nodules with solid and cystic parts.

DISCUSSION

The mechanism of the leiomyomas dissemination is under consideration. It is believed that the smooth muscle cells spread to distant sites after uterine extension into pelvic venous channels. However, in some cases, the uterine leiomyoma is diagnosed after metastases [4,5]. For the most part, patients diagnosed with PBML are in their fifties. The average age of a patient from analyzed case reports was 47,2 years.

The majority of the PBML patients are asymptomatic, although an investigation of 13 case reports showed that 8 of them complained of pulmonary symptoms, such as shortness of breath, cough or chest pain.

The diagnosis of PBML is usually based on findings of multiple nodules in the lungs (rarely a single node) on routine radiological examination such as chest X-ray and CT scan. These nodules can be discovered before hysterectomy or even three months – 20 years afterward. In a report of 13 analyzed case reports of PBML, this interval ranged from 1 month to 20 years with a mean of 9.3 years. 3 out of 13 patients had no history of hysterectomy or myomectomy. Most importantly, PBML nodules pose diagnostic ambiguity mimicking malignant pulmonary metastases especially on routine X-ray (Figure 1) [4].

Both CT and MRI imaging may be useful in finding pulmonary nodules in the setting of PBML (Figure 2; Figure 3). The nodules are usually 0,2 – 8 cm but can vary in size from a few millimeters to several centimeters, and the distribution of these nodules is random. It is worth mentioning that nodules can regress in size during pregnancy or after menopause [6]. The radiologic appearance is well-circumscribed round lesions; the majority of them are bilateral which can be misinterpreted incorrectly as malignant pulmonary metastases. Usually, the nodules have a homogenous appearance on a CT scan. Typically these nodules are non-calcified and do not enhance using i/v contrast agent [1]. In 10 out of 13 investigated cases, the nodules were multiple and bilateral. One of these cases was multiple and unilateral. The other two were solitary in one lung. All of the nodules in X-ray and CT scans were without calcifications and were described as round or oval and well-circumscribed.

In patients with a history of hysterectomy or myomectomy due to leiomyoma, even the ambiguous radiological findings should strongly suggest PBML.

In the setting of inconclusive imaging findings, an imaging-guided biopsy can help to confirm the diagnosis [4]. Pathologically PBML nodules consist of benign smooth cells similar to uterine leiomyoma. Usually, estrogen and progesterone receptors are positive. Pathologists investigated nodules from all 13 cases. Microscopic examinations revealed a proliferation of the differentiated spindle cells without nuclear atypia, anaplasia, necrosis, and neovascularization. The mitotic index was low. Inflammation was not observed. Estrogen and progesterone receptors from all samples were positive. All of these criteria can help to show the benign process and origin from the uterus and can be useful in differentiation from malignant processes.

Our presented case is similar to previously reported cases. Most of the PBML cases were related to previous myomectomy or hysterectomy (77 %). Indeed, a previous diagnosis of uterine leiomyoma may help to point the diagnosis.

The method of choice for the differentiation and diagnosis of these nodules remains a chest CT scan. However, taking into account the fact that this disease affects young women in their reproductive years, the onset of a new era in lung MRI and sensitivity of proton sequences for nodules provides with the opportunity to use MRI as an alternative imaging method.

Macroscopically all of the nodules were ovoid-shape and well-circumscribed. Because of that, differentiation with malignant pulmonary metastases was necessary. Diagnoses were confirmed by histological examination. Pulmonary leiomyomas are slow growing nodules. Their histological pattern is identical to the tissue of uterine leiomyoma. During microscopic examination spindle cells appear proliferated, benign, well-differentiated with a moderate degree of vascularization, insignificant nuclear atypia, mitotic activity, anaplasia, necrosis, vascular invasion. Because the progression of this disease is closely related to sex hormone levels, it is important to find positive estrogen and progesterone receptors during an immunological examination of nodules tissue. It reveals the uterine origin [3].

Actin, desmin, vimentin are immunohistochemical markers that confirm mesenchymal derivation with smooth muscle differentiation of these tumors [7].

One of the analyzed cases was misdiagnosed as pulmonary tuberculosis because of no history of smoking, no family history of cancer and tuberculoma resembling radiological findings. Accordingly, careful collection of patient history is the primary method to suspect the right diagnosis and avoid unnecessary antibiotics.

Differential diagnosis is complicated because other types of spindle cell neoplasm such as malignant melanoma, sarcoma, nerve sheath tumor should be excluded. Immunostains to demonstrate smooth muscle is helpful [2].

Additionally, entrapped alveolar or bronchiolar epithelium can be found in the metastatic foci which can sometimes complicate diagnosis for pathologists. Cavitation and miliary pattern have been reported as well [8, 9].

Furthermore, positive estrogen and progesterone receptors aid in understanding other essential aspects of patient medical history. The doctor should pay attention and consider PBML diagnosis if a patient is in the premenopausal age group, obese or uses estrogens [10].

Although PBML is hormone-sensitive and has a good prognosis is uncommon for this disease to be related to serious complications, such as cor pulmonale, respiratory failure, or even fatal outcomes [7]. The progression of PBML differs and appears to rely on the status of estrogen in the patient. The course of the disease is slow, and patient mortality is not related to the disease in postmenopausal women, while the progress in premenopausal women may lead to death [4].

CONCLUSION

Although PBML is a rare condition, it should be considered for the patients with a history of leiomyoma or hysterectomy or myomectomy due to leiomyomatosis. It is essential seeing as these findings are often misdiagnosed as malignancy because of ambiguous radiological findings, such as bilateral and multifocal well-circumscribed rounded lesions that vary in size. MRI is a suitable tool for evaluating these nodules and ADC value can be useful to differentiate benign nodules from malignant metastasis.

REFERENCES

1. Barnaś E, Książek M, Raś R, Skręt A, Skręt-Magierło J, Dmoch-Gajzlerska E. Benign metastasizing leiomyoma: A review of current literature in respect to the time and type of previous gynecological surgery. *PLoS One*. 2017;12(4):e0175875.
2. Taftaf R, Starnes S, Wang J, et al. Benign metastasizing leiomyoma: a rare type of lung metastases-two case reports and review of the literature. *Case Rep Oncol Med*. 2014;2014:842801.
3. Chen S, Liu RM, Li T. Pulmonary benign metastasizing leiomyoma: a case report and literature review. *J Thorac Dis*. 2014;6(6):E92-8.
4. Teixeira BC, Mahfouz K, Escuissato DL, Costa AF, Noronha Ld. Solitary benign metastasizing leiomyoma: imaging features and pathological findings. *J Bras Pneumol*. 2014;40(2):193-5.
5. Aka N, Iscan R, Köse G, Kaban I. Benign Pulmonary Metastasizing Leiomyoma of the Uterus. *J Clin Diagn Res*. 2016;10(9):QD01-QD03.
6. Latif MF, Sirelkhatim MS, Osman B and Azam F. Benign Pulmonary Metastasizing Leiomyoma of Uterus Presenting as Malignancy of Unknown Origin, A Diagnostic Dilemma. *Austin J Med Oncol*. 2015; 2(2): 1019.
7. Ki EY, Hwang SJ, Lee KH, Park JS, Hur SY. Benign metastasizing leiomyoma of the lung. *World J Surg Oncol*. 2013;11:279. Published 2013 Oct 17. doi:10.1186/1477-7819-11-279
8. Rajesh S, Adam M. Benign metastasizing leiomyoma: "A sheep in wolf's clothing". *Community Oncol* 2013;10:122-5
9. Sousa IR, Campos P, Tavora I. Imaging features of pulmonary leiomyomatosis. *European Congress of Radiology 2013*. <https://doi.org/10.1594/ecr2013/c-1455>.
10. Wiencek-Weiss AJ, Bruliński K. Benign metastasizing leiomyomas in the lungs: a case study. *Kardiochir Torakochirurgia Pol*. 2016;13(1):61-3.

Use of shear wave elastography in the evaluation of liver fibrosis

Dalia Mitraitė¹, Dovilė Duličiūtė¹, Edita Treiklerytė-Varškienė² and Rūta Tatarėlytė³

¹ Department of Radiology, Medical Academy, Lithuanian University of Health Sciences, Kaunas, Lithuania

² Department of Family Medicine, Medical Academy, Lithuanian University of Health Sciences, Kaunas, Lithuania;

³ Clinical Department of Internal Diseases, Medical Academy, Lithuanian University of Health Sciences, Kaunas, Lithuania;

ABSTRACT

Background and objective: Chronic liver disease promotes hepatic inflammation and fibrosis. When diagnosing and treating hepatic diseases such as chronic hepatitis C, it is important to evaluate the degree of liver fibrosis. We aimed to determine the diagnostic capabilities of shear wave elastography (SWE) in patients with liver disease. **Materials and methods:** Hepatic stiffness, size of liver and spleen, portal vein flow velocity, portal vein diameter and flow pattern of hepatic veins were evaluated in 24 patients with diagnosed liver disease and 15 healthy subjects. All measurements were performed using the Philips ElastPQ SWE. The hepatic stiffness was expressed in kilopascals (kPa). **Results:** The mean liver stiffness value was 4.18 ± 1.15 kPa in the control group and 16.19 ± 12.31 kPa inpatient group ($p < 0.001$). An optimal SWE cut-off value of 5.51 kPa had predicted 88% sensitivity and 93% specificity for detecting liver fibrosis. The liver stiffness was positively correlated with the portal vein diameter and the flow pattern of hepatic veins ($r = 0.4$, $P < 0.008$), no significant correlation between liver stiffness and the size of the liver, spleen and portal vein flow velocity was found. **Conclusions:** The liver is stiffer in subjects with diagnosed liver disease than in those who are healthy. The sensitivity of the SWE is 88%, specificity 93% with a cut-off value of 5.51 kPa. Greater hepatic stiffness is associated with increased portal vein diameter, monophasic and biphasic flow patterns of hepatic veins.

Keywords: ultrasound; shear wave elastography; liver stiffness; liver fibrosis; cirrhosis

INTRODUCTION

Based on the latest scientific research, shear wave elastography (SWE) is a sensitive and specific diagnostic tool [1] that may become a standard method in evaluating patients with chronic liver disease. Currently, liver biopsy is the most commonly used method in clinical practice to determine the degree of liver fibrosis. However, it is a painful and risky intervention. A first non-invasive method used for liver stiffness evaluation was transient elastography (TE), implemented in a FibroScan device. It is a painless and safe method, but has several technical limitations: the scan is “blind,” it is not accurate on patients with ascites and on individuals who are morbidly obese or have a thick subcutaneous fat in the abdomen [2].

Newer techniques such as ultrasound-based SWE show results that correlate with the histological fibrosis scores [3], so using such non-invasive methods may reduce the number of patients un-

dergoing potentially dangerous liver biopsy [4] and therefore reduce the risk of complications and medical costs. Measuring liver and spleen shear wave velocity may help to predict prognosis in patients with liver cirrhosis and portal hypertension [5]. SWE may be used to evaluate liver stiffness in patients with chronic hepatitis C virus infection who received antiviral therapy and may help to avoid repeating biopsy and add valuable information about disease progression [6]. The recent imaging phantom experiment showed that observers' experience levels had little impact upon the accuracy of SWE results [7]. Little impact of observers' experience suggests that specific training is not needed prior to performing SWE making this method easily implemented into the clinical practice.

This study proves SWE being useful, valuable and accurate method in measuring liver stiffness which may help to avoid the liver biopsy and threatening complications associated with it.

MATERIALS AND METHODS

The study protocol was approved by the local institutional ethics committee. Before the start of the study, written informed consent was obtained from all participants. Between March and December of 2016, we examined 39 subjects. The patient group consisted of subjects with diagnosed cirrhosis and another liver disease (cholecystitis, steatohepatitis, etc.). The control group consisted of apparently healthy volunteers.

All measurements were performed using Elast-PQ SWE on Philips EPIQ 7 ultrasound system. Scans were conducted by one observer with 30 years of abdominal US experience. The ultrasonographer was blinded to the subject's clinical data.

Participants were in the supine position. First, the size of the liver and spleen, portal vein flow velocity, portal vein diameter and flow pattern of hepatic veins were evaluated. Next, the liver stiffness of the right hepatic lobe was measured. The detection site was fixed at least 1.5 cm beneath the liver capsule, away from the intrahepatic vessels and gallbladder (Figure 1). When the elasticity imaging mode was selected, subjects were asked to hold the breath at mid-respiration for 3–5 s. When the region of interest (ROI) was located, the ultrasonographic initiated the SWE measurement (the median elastic modulus in kilopascals (kPa) was calculated automatically). The mean value of 10 consecutive measurements was used for statistical analysis.

We used the following values proposed by Philips for staging liver fibrosis: no fibrosis (F0) – 2.0–4.5 kPa, normal or mild fibrosis (F0–F1) – 4.5–5.7 kPa, mild-moderate fibrosis (F2–F3) – 5.7–12.0 kPa and moderate-severe fibrosis (F3–F4) – 12.0–21.0+ [8].

To determine the diagnostic accuracy of SWE for the prediction of liver stiffness development in patients with liver disease, receiver operating characteristic (ROC) curve analysis was performed. Statistical analysis was performed using IBM SPSS statistics 24.0 software. Statistical significance was defined as $p < 0.05$.



Figure 1. The image shows how measurements were obtained. The quadrangular white box is ROI. The median stiffness, in this case, is 3.26 kPa.

RESULTS

Ultrasound examination of the abdomen was used to evaluate liver stiffness, size of the liver and spleen, portal vein flow velocity, portal vein diameter and flow pattern of hepatic veins in 39 participants. The baseline characteristics of all participants are listed in Table 1.

The mean liver stiffness value was 4.18 ± 1.15 kPa and 16.19 ± 12.31 kPa in control and patient group, respectively ($p < 0.001$). In this study, the mean liver stiffness values were found to be increased inpatient group compared with the control group ($p < 0.001$). ROC curve analysis showed that, with an optimal SWE cut-off value of 5.51 kPa, the predicted sensitivity and specificity for detecting liver fibrosis is 88% and 93%, respectively (Figure 2).

Table 1. The main participants' characteristics and SWE results.

Characteristic	Control group (n=15)	Patient group (n=24)	P Value
Sex (n) ¹			0.542
Female	6 (40.0)	12 (50.0)	
Male	9 (60.0)	12 (50.0)	
Age (y) ²	52.73 ± 11.73	57.21 ± 14.42	0.338

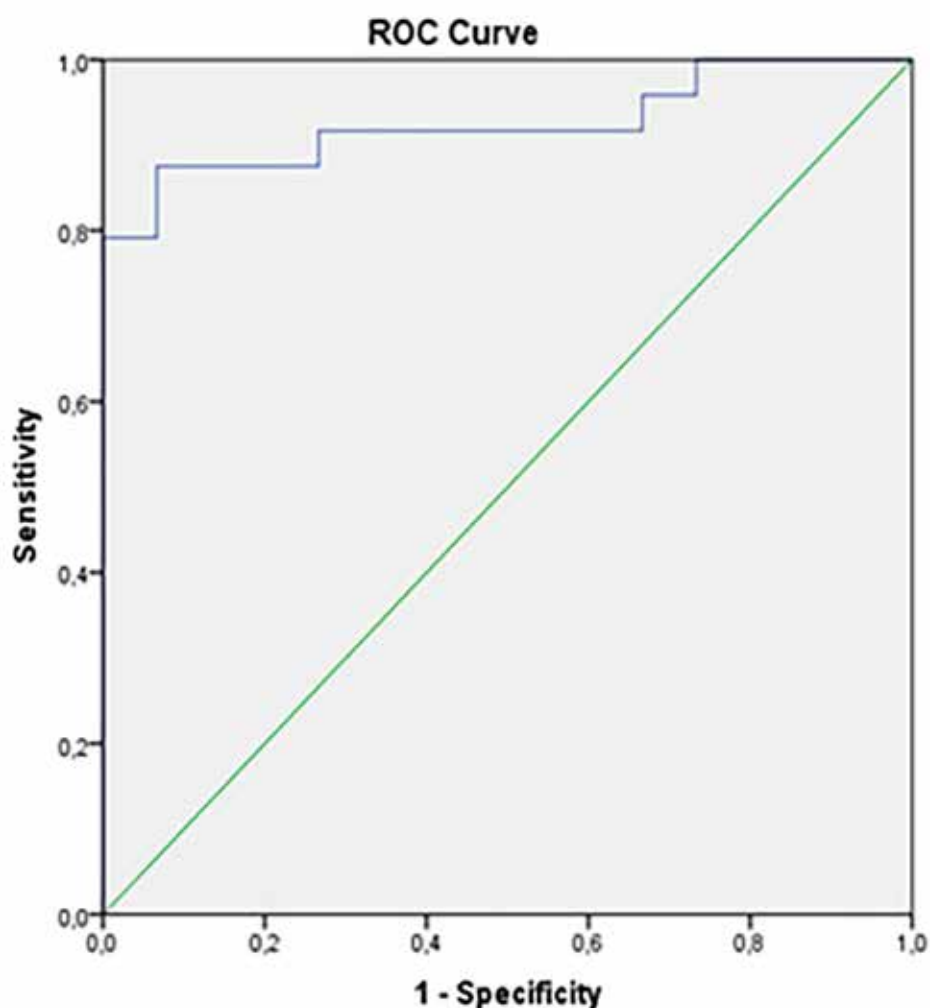
¹ Data are numbers of patients or volunteers with percentages.

² Data are means ± standard deviations.

Fibroscan was performed on 3 (12.5 %) participants in the patient group. Comparing the diagnostic performance of Fibroscan and SWE, the same stage of hepatic fibrosis was found in 2 out of 3 participants, in one patient SWE showed a lower degree of fibrosis (F2-F3) than Fibroscan (F4).

Liver stiffness was found to be positively corre-

lated with the portal vein diameter and the flow pattern of hepatic veins ($r=0.4$, $P<0.008$). The analysis showed that SWE is 9.87 kPa higher than the average value when hepatic vein flow pattern is biphasic and 12.28 kPa higher when monophasic. No significant correlation between liver stiffness and the size of the liver and spleen or portal vein flow velocity was found.

Figure 2. The performance of ElastPQ for predicting liver fibrosis.

DISCUSSION

To our knowledge, we were first to use SWE in the evaluation of liver fibrosis in Lithuania. When we started our study, we had to obtain ten measurements to evaluate the stiffness of the liver. At mid-respiration participants were asked to hold breaths, the measurements were obtained by placing a small white box (ROI) in the right lobe of the liver. The method is simplified now because it's enough to put an ROI box on site once and obtain all ten measurements within. This makes the scan much faster and easier to perform.

One of the limitations of our study was that only a few patients that we examined underwent Fibroscan testing before. There is no database where the results of TE are registered in our clinic so we couldn't confidently compare TE and SWE results. However, TE demonstrated more severe liver fibrosis than SWE in 1 patient. Based on a single case, we cannot make any conclusions, but it may be explained by studies performed on elasticity phantoms that found TE to be better at soft and hard tissues comparing with SWE, both were found equally good at intermediate levels of elasticity [9]. Another study that compared ElastPQ (the same SWE method that we used) and TE results found similar accuracy for staging liver fibrosis [10].

Comparing SWE and TE, an observer who uses SWE has more influence on final results as he or she can exclude several measurements. In contrast, the exclusion is not available in Fibroscan [11]. That may be one of the reasons why the mean stiffness values in control groups vary in different studies. The mean liver stiffness value in our control group was 4.18 ± 1.15 kPa. However, research with a larger sample found it to be higher (5.49 ± 1.59 kPa). They have also found it to be higher in men than in women [12]. However, several studies found it to be less than four kPa in the control group [13, 14].

The fact that liver stiffness was found to be positively correlated with the flow pattern of hepatic veins and the portal vein diameter is not surprising as liver fibrosis is associated with increased portal vein diameter and changing of the flow pattern of hepatic veins into the biphasic and

monophasic as fibrosis progresses. In contrast, typical hepatic venous waveform shows a triphasic pattern. No association with liver and splenic size may be explained due to the small sample and the fact that more than half of the subjects inpatient group (58.3%) had mild-moderate fibrosis or no fibrosis (<12 kPa).

CONCLUSIONS

SWE is a promising method to diagnose liver fibrosis that has the potential to replace liver biopsy, although more extensive prospective studies are needed to define the role of SWE in liver fibrosis staging.

Funding: This research received no external funding.

Conflicts of Interest: The authors declare no conflict of interest.

REFERENCES

1. Guibal, A.; Renosi, G.; Rode, A.; Scoazec, JY.; Guillaud, O.; Chardon, L.; Munteanu, M.; Dumortier, J.; Collin, F.; Lefort, T. Shear wave elastography: An accurate technique to stage liver fibrosis in chronic liver diseases. *Diagn Interv Imaging* 2016; 97: 91-9.
2. Wong, G. Update of liver fibrosis and steatosis with transient elastography (Fibroscan). *Gastroenterol Rep (Oxf)* 2013; 1(1): 19-26.
3. Sande, J.; Verjee, S.; Vinayak, S.; Amersi, F.; Ghesani, M. Ultra-sound shear wave elastography and liver fibrosis: A Prospective Multicenter Study. *World J Hepatol* 2017; 9(1): 38-47.
4. Ferraioli, G.; Tinelli, C.; Lissandrin, R.; Zicchetti, M.; Dal Bello, B.; Filice, G.; Filice, C. Reproducibility and performance of a new point shear wave elastography technique for assessing fibrosis in chronic Hepatitis C. *World J Gastroenterol* 2014; 20(16): 4787-4796.
5. Zhang, Y.; Mao, DF.; Zhang, MW.; Fan, XX. Clinical value of liver and spleen shear wave velocity in predicting the prognosis of patients with portal hypertension. *World J Gastroenterol* 2017; 23(45): 8044-8052.
6. Tada, T.; Kumada, T.; Toyoda, H.; Mizuno, K.; Sone, Y.; Kataoka, S.; etc. Improvement of liver stiffness in patients with hepatitis C virus infection who received direct-acting antiviral therapy and achieved sustained virological response. *J Gastroenterol Hepatol* 2017; 32 (12): 1982-1988.
7. Seliger, G.; Chaoui, K.; Kunze, C.; Dridi, Y.; Jenderka, K.; Wienke, A.; etc. Intra- and inter-observer variation and accuracy using different shear wave elastography methods to assess circumscribed objects – a phantom study. *Med Ultrason* 2017; 19 (4): 357.
8. Richard, G. B. Noninvasive liver fibrosis assessment: Elast-PQ ultrasound shear wave elastography. 2014. Available online: http://www.usa.philips.com/b-dam/b2bhc/us/topics/shearwave/LiverAssessment_DrBarr_WhitePaper_V4_LR.pdf (accessed on 18 October 2016).
9. Carlsen, J.; Pedersen, M.; Ewertsen, C.; Săftoiu, A.; Lönn, L.; Rafaelsen, S.; etc. A Comparative Study of Strain and Shear-Wave Elastography in an Elasticity Phantom. *Am J Roentgenol* 2015; 204 (3): 236-242.
10. Ferraioli, G.; Tinelli, C.; Lissandrin, R.; Zicchetti, M.; Dal Bello, B.; Filice, G.; Filice, C. Point shear wave elastography method for assessing liver stiffness. *World J Gastroenterol* 2014; 20: 4787-4796.
11. Piscaglia, F.; Salvatore, V.; Mulazzani, L.; Cantisani, V.; Schiavone, C. Ultrasound Shear Wave Elastography for Liver Disease. A Critical Appraisal of the Many Actors on the Stage. *Ultraschall Med - Eur J Ultrasound* 2016; 37 (1): 1-5.
12. Roulot, D.; Czernichow, S.; Le Clesiau, H.; Costes, J.L.; Vergnaud, A.C.; Beaugrand, M. Liver stiffness values in apparently healthy subjects: Influence of gender and metabolic syndrome. *J Hepatol* 2008, 48, 606–613.
13. Ling W, Lu Q, Quan J, Ma L, Luo Y. Assessment of impact factors on shear wave based liver stiffness measurement. *Eur J Radiol* 2013; 82: 335–341.
14. Ferraioli, G.; Tinelli, C.; Lissandrin, R.; Zicchetti, M.; Dal Bello, B.; Filice, C. Performance of ElastPQ® shear wave elastography technique for assessing fibrosis in chronic viral hepatitis [abstract]. *J Hepatol* 2013; 58 (1): S7.

Intracranial osteochondroma: A case report with review of literature

Milda Sarkinaite¹, Denas Andrijauskis¹, Egidijus Marcinkevicius², Rymante Gleizniene³

¹ Lithuanian University of Health Sciences

² Lithuanian University of Health Sciences, Department of Neurosurgery

³ Lithuanian University of Health Sciences, Department of Radiology

ABSTRACT

Osteochondromas account for approximately 15% of all bone neoplasms and up to 30-50% of benign bone tumors. Intracranial osteochondromas are very uncommon and represent only 0.1–0.3% of all intracranial neoplasms. We reported a 25-year old previously healthy male presented with malaise, paresthesia, and weakness of the right extremities. The patient was referred to as magnetic resonance imaging (MRI) to confirm the demyelinating disease. Instead of multiple sclerosis, an extra-axial lesion with hemorrhage was suspected, and the patient was hospitalized. Computer tomography (CT) showed a well-circumscribed extra-axial lesion with calcification. The patient had an episode of seizures accompanied by severe morning headaches, dizziness, vomiting, and speech disorders. The patient underwent craniotomy with the excision of the tumor under the control of intraoperative magnetic resonance imaging. Few episodes of Jacksonian Seizures were observed during the surgery and after the procedure. After the surgery patient remained with only slight neurological deficits. Follow-up of the patient with clinical examination and imaging studies showed no evidence of any recurrence.

Keywords: intracranial, osteochondroma, bone tumor, supratentorial

INTRODUCTION

Osteochondroma is a benign neoplasm that arises from mature hyaline cartilage together with the local ossification center. The tumor itself grows slowly, although it can reach well-defined, great sizes [1]. Osteochondromas account for approximately 15% of all bone neoplasms and up to 30-50% of benign bone tumors. They usually occur around the knee or the proximal humerus [2]. Osteochondromas often occur spontaneously, although there are few reports about osteochondromas following radiotherapy [3-5]. However, intracranial osteochondromas are very uncommon and represent only 0.1–0.3% of all intracranial neoplasms [6]. So far only sporadic case reports can be found in the literature. Most of the intracranial osteochondromas arise extradurally from the base of mid-skull, although they may rarely occur from the dura mater of the falx cerebri [7, 8].

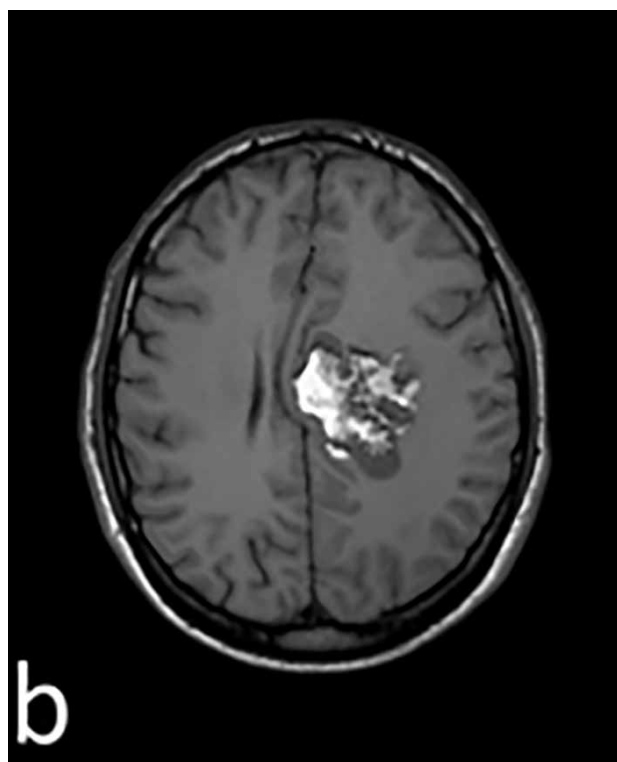
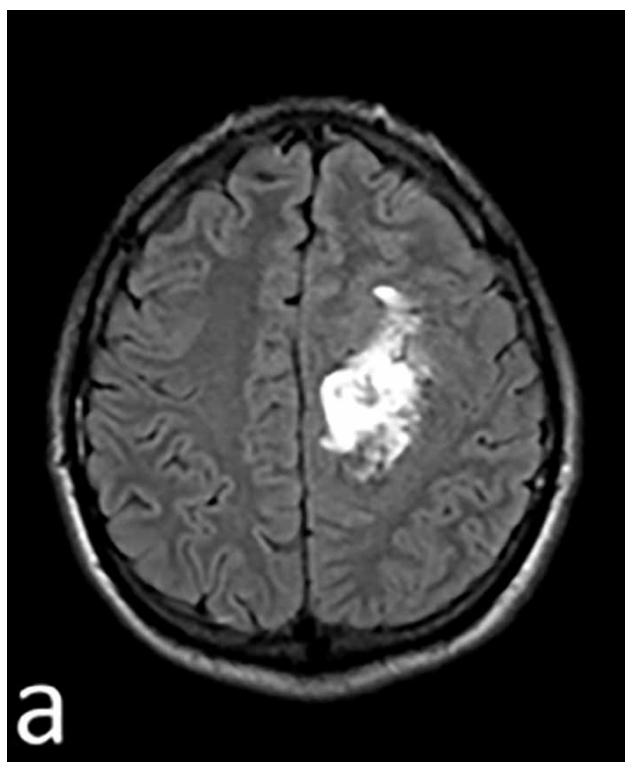
CASE REPORT

A 25-year old previously healthy male presented with malaise, paresthesia, and weakness of

the right extremities. The symptoms first started half a year ago when he experienced paresthesia of the right lower extremity. The condition became extremely severe during the last week because of newly originated paresthesia of the right arm. The patient was consulted by the general practitioner and neurologist, and the demyelinating disease was suspected. He was referred to as magnetic resonance imaging (MRI) at the “Affidea Lietuva” diagnostic center to confirm multiple sclerosis. The MRI of the brain showed brain lesions with a slight midline shift and local compression features in the left frontoparietal region (Figure 1). The differentiation involved arteriovenous malformation and tumor with the subacute hemorrhage. The patient was hospitalized in the Hospital of Lithuanian University of Health Sciences Kaunas Clinics, department of neurosurgery. Physical examination revealed no pathology except for the focal neurological symptoms. Right-sided hemiparesis with muscle weakness, impaired ability to walk and instability in Romberg’s pose were detected. Later on computerized tomography (CT) was performed and showed well-circumscribed extra-axial mass

lesions with intense calcification. The lesion was located in the corona radiata of the left frontal region (Figure 2). The midline structures were shifted to the right. Differential diagnosis included extra-axial tumor (calcified meningioma, metastasis, sarcoma), intralesional calcified cavernous hemangioma, maybe fibrous dysplasia. Angiography and electroencephalogram revealed no pathology (Figure 3). The neurosurgical treatment was delayed at that time because of subcutaneous infection found in the thigh. After three months, the patient had his first episode of seizures following the immediate hospitalization. On admission to hospital, the patient also complained of having severe morning holocranial headaches accompanied by dizziness, vomiting, and speech disorders. On physical examination, he was conscious, alert with stable

vitals, although neurological deficits appeared to be more severe than three months ago. The patient underwent craniotomy with the excision of the tumor under the control of intraoperative magnetic resonance imaging (Figure 4). Although the patient was previously started on antiepileptic drugs, few episodes of Jacksonian seizures were observed during the surgery and after the procedure. The pathohistological diagnosis of osteochondroma was given. The patient felt well at follow-up after the operation. The improvement of symptoms was seen. However mild right-sided weakness remained. Antiepileptic treatment with phenobarbital, as well as follow-up EEG was recommended. The control MRI taken in the postoperative period of the patient revealed the total removal of the lesion (Figure 5).



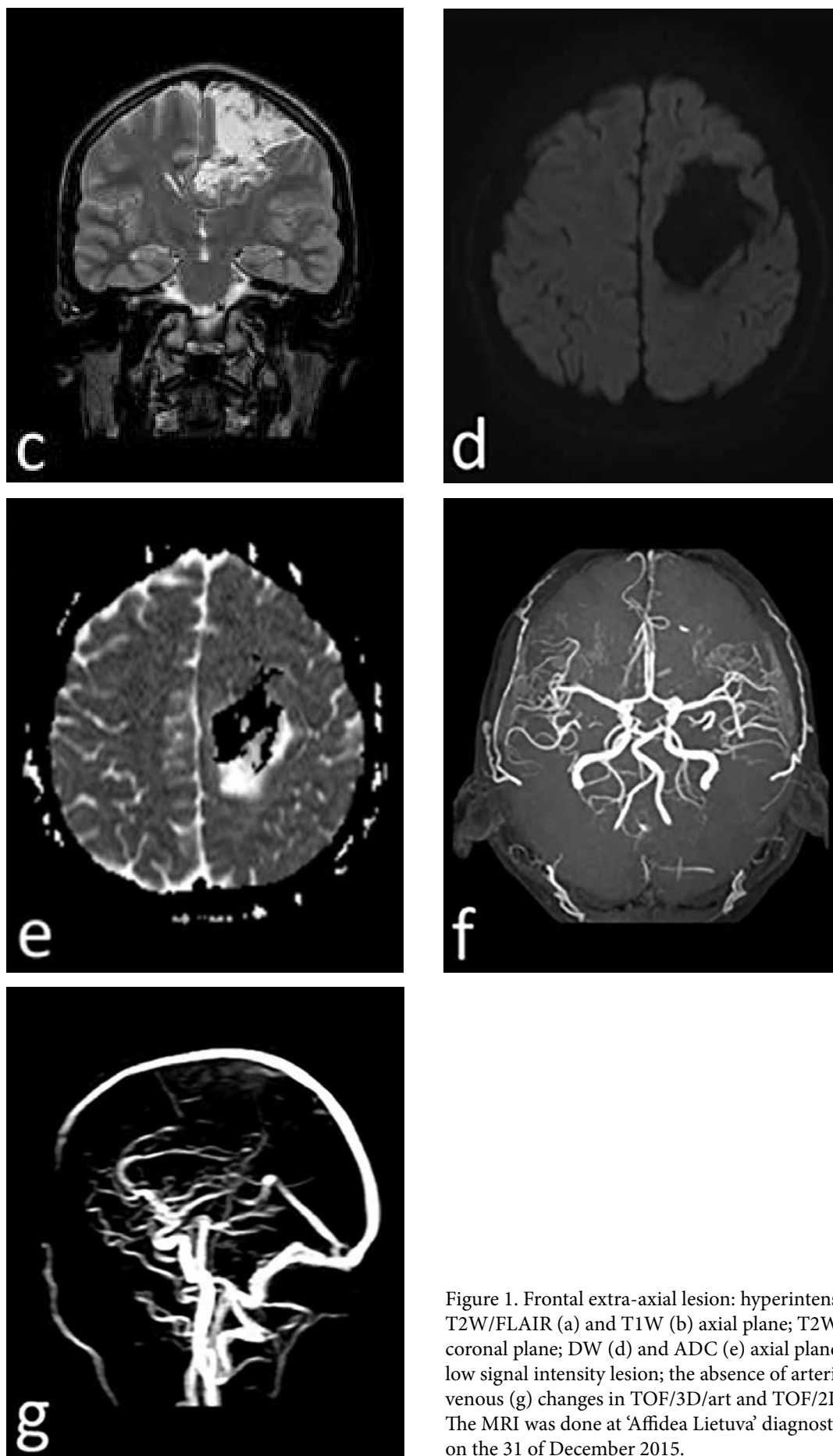


Figure 1. Frontal extra-axial lesion: hyperintense lesion T2W/FLAIR (a) and T1W (b) axial plane; T2W (c) coronal plane; DW (d) and ADC (e) axial plane revealed low signal intensity lesion; the absence of arterial (f) and venous (g) changes in TOF/3D/art and TOF/2D/vein. The MRI was done at 'Affidea Lietuva' diagnostic center on the 31 of December 2015.

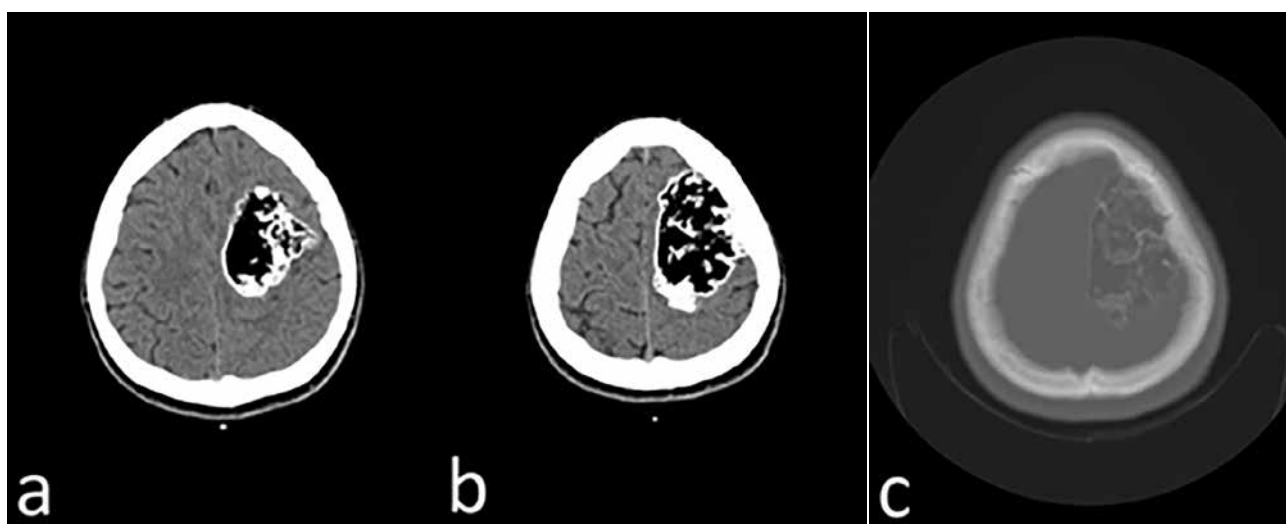


Figure 2. CT 2015 12 31 LSMUL KK: CT axial brain window (a, b), bone window (c): calcified lesion with fat inclusion are seen on the periphery.

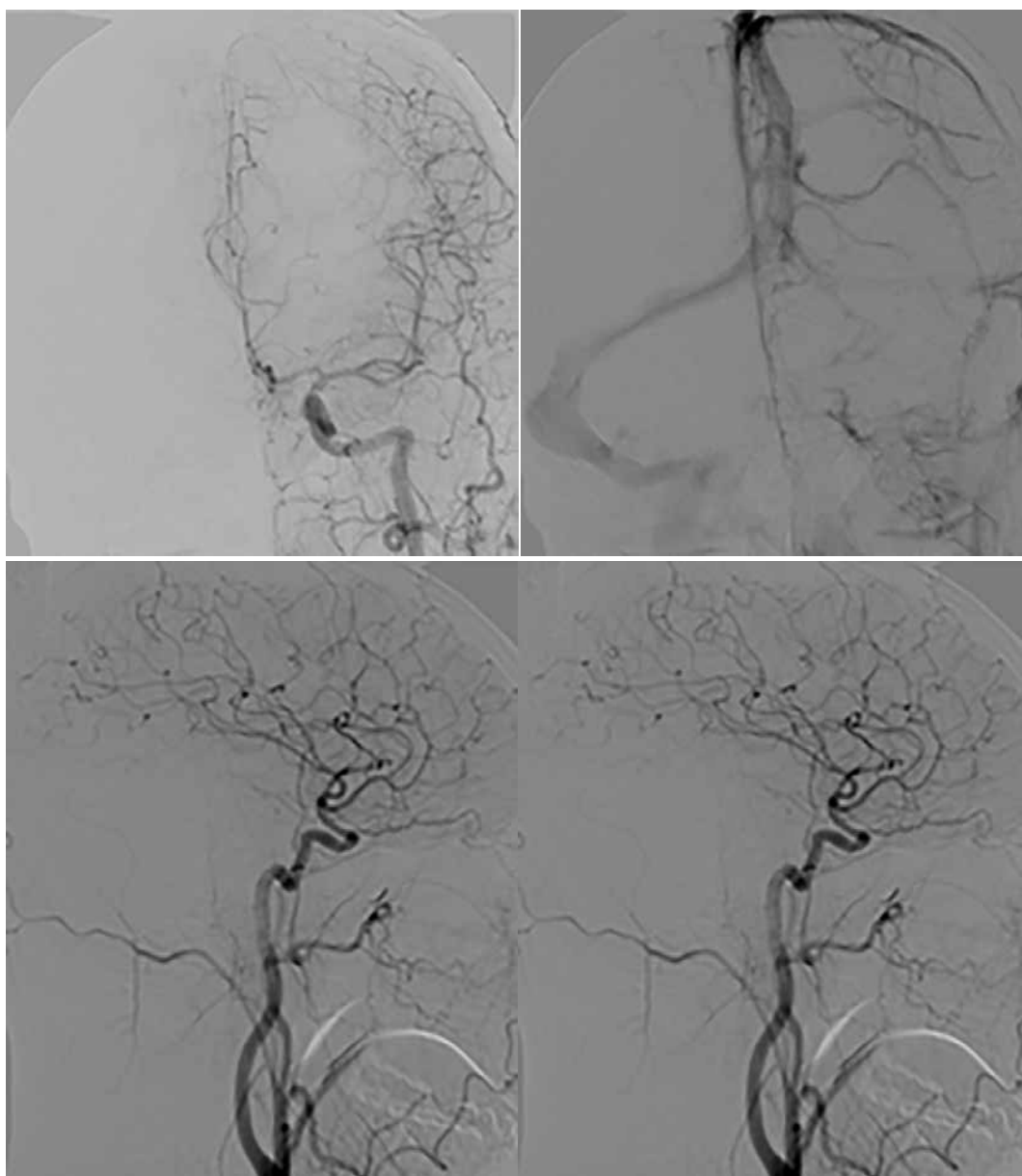


Figure 3. Anterior and lateral view of angiography revealed no pathology in both arterial and venous phases.

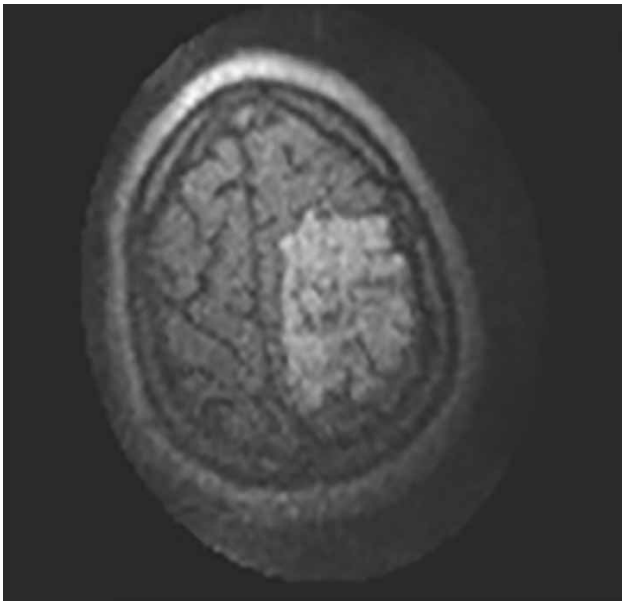


Figure 4. Hyperintense lesion was seen on the intraoperative MRI T1W axial plane.

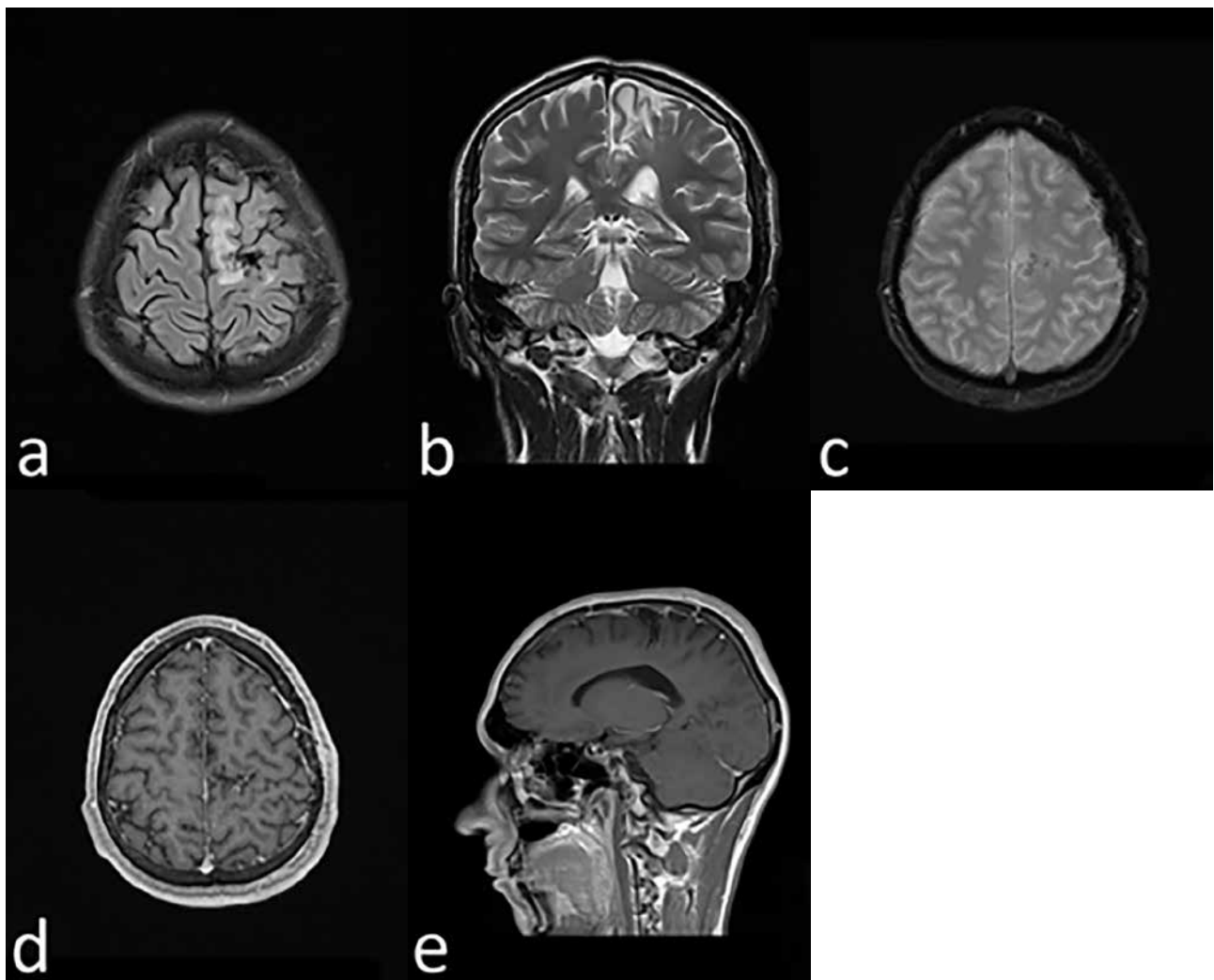


Figure 5. The postoperative control MRI (2016/2018). The postoperative cystic gliotic area at the left frontal lobe: T2W/FLAIR axial (a), T2W coronal (b), T2W/FLAIR/hemo axial (c), T1W post c/m, axial, sagittal (d, e).

DISCUSSION

Osteochondromas typically occur in the metaphyseal end of skeletal bones, such as the distal femur, proximal tibia, and proximal humerus. Intracranial osteochondromas are seen uncommonly. The majority occur from the base of the skull. Only on rare occasions, they arise from the dura attached to the falx cerebri in the frontoparietal area. Therefore, the localization of the tumor makes our case unique. Intracranial osteochondromas may arise at any age with the peak incidence in the third decade, as seen in our patient [9]. Clinical manifestation of the disease mostly depends on the tumor mass effect and location [10]. The supratentorial tumor may cause a mass effect with contralateral midline shift. This may lead to rapid deterioration of the clinical condition. Meanwhile, tumors arising from the base of the skull manifest earlier than supratentorial. Because of the rare incidence of intracranial osteochondromas, the differential diagnosis with other more commonly found tumors, such as meningioma becomes essential. CT is the first choice diagnostic method to investigate neurologic signs or symptoms. This is the reason why the majority of meningiomas are detected using CT. Native CT scans usually show from slightly hyperdense to normal brain tissue, and up to 30% of cases have some calcification. Post-contrast CT reveals the homogenous enhancement of contrast material. Osteochondromas that arise from the convexity dura usually imitate meningiomas on MRI [11]. Osteochondromas appear with the central hypointensity on T1W and T2W sequences, which can be similar to calcification, with a slight chance of intratumoral hemorrhage. Calcifying or ossifying centers can be observed in meningiomas with metaplastic change. On rare occasions, meningiomas might also present with necrotic and hemorrhagic areas. The features of meningiomas include more homogenous contrast enhancement and the dural tail, unlike in osteochondromas, which show heterogeneous enhancement on contrast. More specific findings of osteochondromas are the hyperostosis and absence of surrounding edema [9]. Due to the heterogeneous appearance of the lesion, the diagnosis of the dermoid tumor should also

be excluded. Most commonly dermoid tumors present with signal intensity features similar to fat. Unlike intracranial lipomas that follow fat density on all sequences, intracranial dermoid cysts have various signal characteristics on MRI. They appear as hyperintense on T1W-weighted scans and hypointense on T2W scans. Dermoid tumors and osteochondromas are similar to the fact that they both may be inhomogeneous. The heterogeneity of dermoid tumors depends on the presence of hair follicles, calcifications, and cellular debris. Rupture of the dermoid tumor can lead to fat drops in the subarachnoid spaces or ventricles, with T1W high signal intensity. Fat-fluid levels can appear in the lateral ventricles. Similarly to our case, CT scans of FD show calcified lesion. After contrast administration, enhancement is not common, and if present should be limited to the peripheral edge. Another tumor that should be ruled out before the diagnosis of osteochondroma can be confirmed is fibrous dysplasia (FD). Radiographically, FD usually has a non-symmetrical ground-glass appearance on CT scan. 20% of FD cases present with cystic lesions. FD merges with skull bone and leads to the thinning of the cortical bone [12]. Developing FD might demonstrate a cauliflower-like appearance, which is more commonly found in osteochondromas. Moreover, if the tumor invades the meninges, vasogenic edema can be found in the surrounding brain tissue. Although MRI is not the first choice in diagnosing FD, it can be sometimes used in unclear cases. T1W and T2W reveal heterogeneous signal, usually from low to moderate intensity. Contrasting gives the heterogeneous appearance to the lesion. It is also important to exclude intracranial metastasis when considering the origin of the tumor. Although, brain metastases are often multiple, up to 50% of cases demonstrate only a single lesion as seen in our case. The majority of metastatic tumors appear at the grey-white matter junction or in the arterial watershed areas. On native CT scans the mass may be isodense, hypodense or hyperdense comparing to normal brain tissue. There is a different amount of vasogenic edema found in the surrounding brain tissue. After contrast material is administrated, punctate, nodular and intensive enhancement can be observed. If

the tumor overgrows surrounding vasculature, a typical sign of ring-enhancing is seen. Meanwhile on MRI scans, metastatic tumors appear as well-circumscribed, clearly enhancing, extra-axial, dura based, heterogeneous lesions. T1W typically reveals iso- to hypointense signal intensity while T2W and/or FLAIR commonly show hyperintense lesions. Similarly to CT after contrast, an MRI enhancement pattern can be uniform, punctate, or ring-enhancing, but it is usually intense. On DWI edema is inconsistent with the size of the tumor and appears dark. While discussing treatment options, the main treatment of intracranial osteochondromas is complete surgical removal of the tumor. Although osteochondromas tend to be benign, there is a slight possibility of 1% for malignant transformation [13]. The thickness of the cartilage cap seen in MRI helps to assess the possibility of malignant transformation. Cartilage cap thickness of more than 2 cm indicates the possible malignant change [14]. Our case represents the sporadic incidence of osteochondroma. Rarely this tumor occurs as part of generalized hereditary multiple exostoses syndrome, which is an autosomal dominant condition. In our case, the tumor was completely removed, and the patient remained with only slight neurological deficits. Follow-up of the patient with clinical examination and imaging studies showed no evidence of any recurrence.

CONCLUSION

The surgical removal of osteochondromas is the gold standard of treatment. Although intracranial osteochondromas are rare, they should be involved in the differential diagnosis of intracranial extraxial neoplasms with a rare form of calcification. Despite the benign growth pattern of the tumor, the risk of recurrence should be closely monitored after the excision.

REFERENCES

1. Somerset HL, Kleinschmidt-DeMasters BK, Rubinstein D, et al. (2010) Osteochondroma of the convexity: pathologic-Neuroimaging correlates of a lesion that mimics high-grade meningioma. *J Neurooncol* 98: 421-426.
2. Murphey MD, Choi JJ, Kransdorf MJ, et al. (2000) Imaging of osteochondroma: variants and complications with radiologicpathologic correlation. *Radiographics* 20: 1407-1434.
3. Kushner BH, Roberts SS, Friedman DN, et al. Osteochondroma in long-term survivors of high-risk neuroblastoma. *Cancer* 2015; 121:2090.
4. Marcovici PA, Berdon WE, Liebling MS. Osteochondromas and growth retardation secondary to externally or internally administered radiation in childhood. *Pediatr Radiol* 2007; 37:301.
5. Faraci M, Bagnasco F, Corti P, et al. Osteochondroma after hematopoietic stem cell transplantation in childhood. An Italian study on behalf of the AIEOP-HSCT group. *Biol Blood Marrow Transplant* 2009; 15:1271.
6. Venkata RI, Kakarala SV, Garikaparathi S, Duttaluru SS, Parvatala A, Chinnam A. Giant intracranial osteochondroma: A case report and review of the literature. *Surg Neurol Int* 2011;2:118.
7. Venkata RI, Kakarala SV, Garikaparathi S, et al. (2011) Giant intracranial osteochondroma: a case report and review of the literature. *Surg Neurol Int* 2: 118.
8. Colpan E, Attar A, Ereku S, et al. (2003) Convexity dural chondroma: a case report and review of the literature. *J Clin Neurosci* 10: 106-108
9. Erdogan S, Zorludemir S, Erman T, et al. (2006) Chondromas of the falx cerebri and dural convexity: report of two cases and review of the literature. *J Neurooncol* 80: 21-25.
10. Omalu BI, Wiley CA, Hamilton RL (2003) A 53-year-old male with new onset seizures. *Brain Pathol* 13: 419-423.
11. Somerset HL, Kleinschmidt-DeMasters BK, Rubinstein D, Breeze RE (2010) Osteochondroma of the convexity: pathologicneuroimaging correlates of a lesion that mimics high-grade meningioma. *J Neurooncol* 98:421-426
12. Unal Erzurumlu Z, Celenk P, Bulut E, Baris YS. CT Imaging of Craniofacial Fibrous Dysplasia. *Case Rep Dent* 2015. 2015:134123.
13. Matz S, Israeli Y, Shalit MN, et al. (1981) Computed tomography in intracranial supratentorial osteochondroma. *J Comput Assist Tomogr* 1: 109-115.
14. Padhya TA, Athavale SM, Kathju S, Sarkar S, Mehta AR. Osteochondroma of the skull base. *Otolaryngol Head Neck Surg* 2007;137:166-8.

